

# Deep-blue supercontinuum light sources based on tapered photonic crystal bres

**Sørensen, Simon Toft**

*Publication date:*
2013

*Document Version*
Publisher's PDF, also known as Version of record

# Deep-blue supercontinuum light sources based on tapered photonic crystal fibres

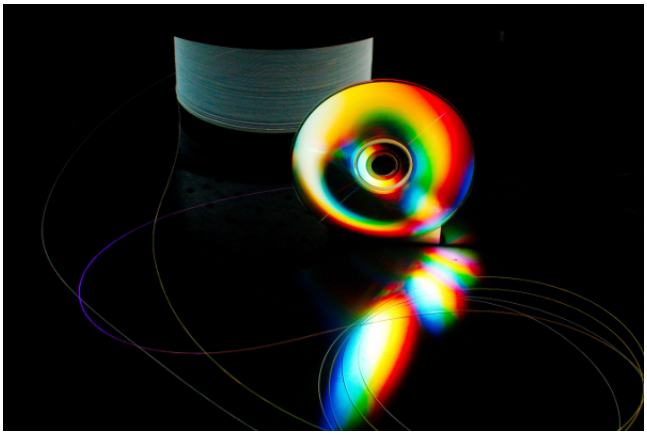

**Simon Toft Sørensen**

PhD Thesis

June 2013

DTU Fotonik
Department of Photonics Engineering

Technical University
of Denmark

NKT Photonics
the power of light

# Abstract

The nonlinear pulse broadening phenomenon of supercontinuum generation in optical fibres is appreciated as one of the most striking in nonlinear physics. Thanks to the unique combination of high brightness and octave-spanning spectra, modern "white-light" supercontinuum lasers have found numerous applications in areas such as spectroscopy and microscopy.

In this work, we exploit the tremendous design freedom in air hole structured photonic crystal fibres to shape the supercontinuum spectrum. Specifically, the supercontinuum dynamics can be controlled by clever engineering of fibres with longitudinally varying air hole structures. Here we demonstrate supercontinuum generation into the commercially attractive deep-blue spectral region below 400 nm from an Yb laser in such fibres. In particular, we introduce the concept of a group acceleration mismatch that allows us to enhance the amount of light in the deep-blue by optimising the fibre structure. To this end, we fabricate the first single-mode high air-fill fraction photonic crystal fibre for blue-extended supercontinuum sources.

The mechanisms of supercontinuum broadening are highly sensitive to noise, and the inherent shot-to-shot variations in long-pulsed supercontinuum sources are a limiting factor for several applications. We investigate different approaches to quantify and lower the spectral noise. Specifically, we characterise the spectral noise in the framework of statistical higher-order moments, which provides insight into the nature of the noise across the spectrum. We further investigate the possibilities of reducing the spectral noise by modulating the pump with a weak seed, which makes the broadening dynamics increasingly deterministic rather than driven by noisy modulation instability. Particular attention is paid to the commercially relevant high power regime. Finally, we examine passive noise reduction in photonic crystal fibres with longitudinally varying air hole structures.

# Resumé

## Blå-forstærkede superkontinuum lyskilder baseret på taperede fotoniske krystal fibre

Den ekstreme pulsforbredning i optiske fibre, superkontinuum generering, er anerkendt som et af de mest spektakulære fænomener i den ulineære fysik. Takket være den unikke kombination af en høj lysstyrke og spektre der spænder over mere end en optisk oktav, har moderne superkontinuum "hvidlys" lasere fundet talrige anvendelser inden for bl.a. spektroskopi og mikroskopi.

I dette arbejde udnytter vi den enorme designfrihed i fotoniske krystal fibre, bestående af en mikrostruktur af lufthuller, til at forme superkontinuum spektret. Konkret kan dynamikken bag superkontinuum generering styres ved at variere mikrostrukturen af lufthuller på langs af fiberen. Ved at gøre dette, demonstrerer vi superkontinuum generation i det kommercielt attraktive mørkeblå bølgelængdeområde under 400 nm fra en Yb laser. Vi indfører desuden begrebet gruppe-accelerations tilpasning, der gør det muligt, at øge lyseffekten i den blå spektrale kant ved at optimere fiberstrukturen. Til dette formål fabrikerede vi den første single-mode fotoniske krystal fiber med høj luftfyldningsfaktor til blå-forstærkede superkontinuum kilder.

Forbredningsmekanismerne bag superkontinuum generering er meget følsomme over for støj, hvilket medfører store variationer fra puls til puls i superkontinuum kilder baseret på lange pulser. Dette er en klar begrænsning for adskillige potentielle anvendelser. Vi undersøger forskellige tilgange til at kvantificere den spektrale støj, samt til at sænke støjen ved at kontrollere forbredelsesmekanismerne. Konkret karakteriserer vi den spektrale støj med

statistiske højereordens momenter, der giver indsigt i karakteren af støjen over hele den spektrale båndbredde. Vi gransker desuden mulighederne for at reducere den spektrale støj, ved at modulere pumpen med en svag puls. Dette gør i højere grad forbredelsen deterministisk fremfor drevet af modulations instabiliteter. Vi fokuserer specielt på det kommercielt relevante høj-effekts regime. Derudover undersøger vi, om den turbulente superkontinuum forbredning kan tæmmes i fotoniske krystal fibre med longitudinalt varierende mikrostruktur.

# Preface

This thesis is submitted for the degree of Doctor of Philosophy of the Technical University of Denmark. The research contained herein has been carried out over the three year period May 2010 to April 2013 as a part of the research project "Intelligent tapers and seeding for taming the optical rogue wave and develop stable deep-blue supercontinuum light sources (ITRUS)" supported by the Danish Agency for Science, Technology and Innovation (Det Frie Forskningsråd for teknologi og produktion, projektnr. 09-070566). The majority of the work was performed at the main project partners DTU Fotonik, Department of Photonics Engineering at the Technical University of Denmark and NKT Photonics A/S in Birkerød, but also during a research stay in the Optoelectronics and Photonics research group at University of Franche-Comté, Besançon, in the summer 2011. The project was supervised by Prof. Dr. Ole Bang, DTU Fotonik, and Carsten L. Thomsen, Manager - Product Development at NKT Photonics A/S, but also partly by Prof. Dr. John M. Dudley during the research stay in Besançon.

I would, of course, like to take the full credit for all the good parts of this work and blame the faults, flaws and weaknesses on others. However, not only is this sort of behaviour generally frowned upon, it also greatly discredits the large team effort on which this work is based. Without all the dedicated help and support I have received, the outcome of this project would simply not have been possible. I am therefore indebted to several people. First and foremost, I wish to thank my supervisor Ole Bang for giving me the opportunity to work on this exciting project *and* for making it a truly enjoyable journey. This thesis would not have come to existence without his dedication and enthusiastic guidance, motivation and support. I must also thank my co-supervisor Carsten L. Thomsen for his support and guidance, but also for opening the doors for an exciting academic-industrial

collaboration.

My (project) partners in crime, Casper Larsen and Uffe Møller, deserve special mentioning for superb teamwork and heaps of fun. In fact, the same goes for the many others who contributed to this work. Especially, Christian Jakobsen for always finding a way to fabricate our increasingly odd and demanding fibre designs, and Jeppe Johansen and Peter M. Moselund for discussions and indispensable help in the lab. But also my other co-authors and collaborators: Christian Agger, Thomas V. Andersen, Thomas Feuchter, Alex Judge (University of Sydney) and Michael Frosz (now at Max Planck Institute for the Science of Light, Erlangen). And Chris Brooks for last-minute proofreading this thesis. It is also my pleasure to thank John M. Dudley for hosting me in Besançon and making it a fun and enlightening experience (yes, I am infinitely beer indebted), and to Benjamin Wetzel for great collaboration during my stay. I am also very thankful to all the guys who showed me how to have a good time in France (without speaking French).

I further want to express a special thanks to everybody who participated in the OSA Student Chapter and PhD Club activities, and to all my friends and family for a seemingly infinite support.

Finally, I wish to acknowledge the Technical University of Denmark and the Danish Agency for Science, Technology and Innovation for financial support of this PhD project, and Otto Mønsteds Fond, Oticon Fonden, the French Embassy in Denmark (Programme de coopération scientifique et universitaire) and the Optical Society of America for indispensable financial support for conference participation and my research stay in Besançon.

The thesis was presented for public examination and debate on 27 May 2013 at the Technical University of Denmark. The evaluation committee consisted of Dr. Goëry Genty, Tampere University of Technology, Finland, Dr. John C. Travers, Max Planck Institute for the Science of Light, Erlangen, Germany, and Dr. Jesper Lægsgaard, Technical University of Denmark. A few minor corrections have been made to the original thesis.

*Kongens Lyngby, June 2013*

Simon Toft Sørensen

# Contents

# List of publications

## Journal publications

This thesis is based on the following peer-review journal publications. It should be noted that Paper IV is not yet published.

**Paper I**

S. T. Sørensen, A. Judge, C. L. Thomsen, and O. Bang, "Optimum fiber tapers for increasing the power in the blue edge of a supercontinuum—group-acceleration matching," Opt. Lett. **36**, 816–818 (2011).
http://dx.doi.org/10.1364/OL.36.000816

**Paper II**

S. T. Sørensen, U. Møller, C. Larsen, P. M. Moselund, C. Jakobsen, J. Johansen, T. V. Andersen, C. L. Thomsen, and O. Bang, "Deep-blue supercontinnum sources with optimum taper profiles – verification of GAM," Opt. Express **20**, 10635-10645 (2012).
http://dx.doi.org/10.1364/OE.20.01063

**Paper III**

U. Møller, S. T. Sørensen, C. Larsen, P. M. Moselund, C. Jakobsen, J. Johansen, C. L. Thomsen, O. Bang, "Optimum PCF tapers for blue-enhanced supercontinuum sources [Invited]," Opt. Fiber Technol. **18**, 304-314 (2012).
http://dx.doi.org/10.1016/j.yofte.2012.07.010

**Paper IV**

S. T. Sørensen, C. Larsen, C. Jakobsen, C. L. Thomsen, O. Bang, "Single-mode high air-fill fraction photonic crystal fiber for high-power deep-blue supercontinuum sources," submitted to Opt. Lett. 29 April 2013.

**Paper V**

S. T. Sørensen, O. Bang, B. Wetzel, J. M. Dudley, "Describing supercontinuum noise and rogue wave statistics using higher-order moments," Opt. Comm. **285**, 2451-2455 (2012).
http://dx.doi.org/10.1016/j.optcom.2012.01.030

**Paper VI**

S. T. Sørensen, C. Larsen, U. Møller, P. M. Moselund, C. L. Thomsen, and O. Bang, "Influence of pump power and modulation instability gain spectrum on seeded supercontinuum and rogue wave generation," J. Opt. Soc. Am. B **29**, 2875-2885 (2012).
http://dx.doi.org/10.1364/JOSAB.29.002875

**Paper VII**

S. T. Sørensen, C. Larsen, U. Møller, P. M. Moselund, C. L. Thomsen, and O. Bang, "The role of phase coherence in seeded supercontinuum generation," Opt. Express **20**, 22886-22894 (2012).
http://dx.doi.org/10.1364/OE.20.022886

**Paper VIII**

U. Møller, S. T. Sørensen, C. Jakobsen, J. Johansen, P. M. Moselund, C. L. Thomsen, and O. Bang, "Power dependence of supercontinuum noise in uniform and tapered PCFs," Opt. Express **20**, 2851-2857 (2012). http://dx.doi.org/10.1364/OE.20.002851;
Erratum, Opt. Express **20**, 23318-23319 (2012).
http://dx.doi.org/10.1364/OE.20.023318

## Conference contributions

The conference contributions with relation to this thesis are listed below in chronological order.

**Conference I**

S. T. Sørensen, A. Judge, C. L. Thomsen, and O. Bang, "Group-Acceleration Matching in Tapered Optical Fibers for Maximising the Power in the Blue-Edge of a Supercontinuum," in CLEO/Europe and EQEC 2011 Conference Digest, OSA Technical Digest (CD) (Optical Society of America, 2011), paper CD.P12.

**Conference I**

U. Møller, S. T. Sørensen, P. M. Moselund, J. Johansen, C. L. Thomsen, and O. Bang, "Reduced Amplitude Noise in Supercontinuum Generated in Tapered PCFs," in CLEO/Europe and EQEC 2011 Conference Digest, OSA Technical Digest (CD) (Optical Society of America, 2011), paper CD8.3.

**Conference III**

S. T. Sørensen, O. Bang, J. M. Dudley, "Higher order moment description of supercontinuum noise and rogue wave statistics," Rogue Waves: International Workshop, Dresden, Germany (2011).

**Conference IV**

U. Møller, S. T. Sørensen, C. Jakobsen, J. Johansen, P. M. Moselund, C. L. Thomsen, and O. Bang, "Supercontinuum noise in tapered photonic crystal fibers," Rogue Waves: International Workshop, Dresden, Germany (2011).

**Conference V**

S. T. Sørensen, U. Møller, C. Larsen, P. M. Moselund, C. Jakobsen, J. Johansen, T. V. Andersen, C. L. Thomsen, and O. Bang, "Asymmetric Draw-Tower Tapers for Supercontinuum Generation and Verification of the Novel Concept of Group-Acceleration Matching," in CLEO: QELS-Fundamental Science, OSA Technical Digest (Optical Society of America, 2012), paper QM4E.4.

**Conference VI**

S. T. Sørensen, O. Bang, B. Wetzel, J. M. Dudley, "Higher-Order Moment Characterisation of Rogue Wave Statistics in Supercontinuum Generation," in Nonlinear Photonics, OSA Technical Digest (Optical Society of America, 2012), paper JTu5A.22.

**Conference VII**

U. Møller, S. T. Sørensen, C. Larsen, C. Jakobsen, J. Johansen, P. M. Moselund, C. L. Thomsen, and O. Bang, "Optimization of Tapered Photonic Crystal Fibers for Blue-Enhanced Supercontinuum Generation," in Nonlinear Photonics, OSA Technical Digest (Optical Society of America, 2012), paper JW4D.1. **Postdeadline**.

**Conference VIII**

U. Møller, S. T. Sørensen, P. M. Moselund, C. Jakobsen, C. L. Thomsen, and O. Bang, "High power supercontinuum generation in tapered photonic crystal fibers", part of: 3rd International Workshop on Laser-Matter Interaction (WLMI 2012), Porquerolles.

**Conference IX**

U. Møller, S. T. Sørensen, C. Larsen, P. M. Moselund, C. Jakobsen, J. Johansen, C. L. Thomsen, and O. Bang, "Tapered photonic crystal fibers for blue-enhanced supercontinuum generation," part of: EOS Annual Meeting (EOSAM 2012), ISBN: 978-3-9815022-4-4, European Optical Society.

**Conference X**

S. T. Sørensen, C. Larsen, U. Møller, P. M. Moselund, C. Jakobsen, J. Johansen, T. V. Andersen, C. L. Thomsen, and O. Bang, "Su-

percontinuum Generation in Uniform and Tapered Photonic Crystal Fibers," Presented at: The International OSA Network of Students (IONS) conference and SPIE Federation of Optics College and University Students (FOCUS), New York (2012).

**Best Oral Presentation award by the American Physical Society (APS) Division of Laser Science (DLS)**.

**Conference XI**

S. T. Sørensen, C. Larsen, U. Møller, P. M. Moselund, C. L. Thomsen, and O. Bang, "Seeded Supercontinuum Generation - Modulation Instability Gain, Coherent and Incoherent Rogue Waves," in Frontiers in Optics Conference, OSA Technical Digest (online) (Optical Society of America, 2012), paper FTh1D.4.

**Conference XII**

C. L. Thomsen, F. D. Nielsen, J. Johansen, C. Pedersen, P. M. Moselund, U. Møller, S. T. Sørensen, C. Larsen, and O. Bang, "New horizons for supercontinuum light sources: from UV to mid-IR," in Proc. SPIE 8637, Complex Light and Optical Forces VII, 86370T (2013). **Invited**.

**Conference XIII**

S.T. Sørensen, C. Larsen, U. Møller, P. M. Moselund, C. L. Thomsen, and O. Bang, "Influence of Phase Coherence on Seeded Supercontinuum Generation," to be presented at CLEO/Europe and EQEC 2013, paper IF-P.10.

**Conference XIV**

S.T. Sørensen, C. Larsen, U. Møller, P. M. Moselund, C. L. Thomsen, and O. Bang, "Coherent and Incoherent Rogue Waves in Seeded Supercontinuum Generation," to be presented at CLEO/Europe and EQEC 2013, paper JSIII-P.6.

**Conference XV**

S.T. Sørensen, C. Larsen, C. Jakobsen, C. L. Thomsen, and O. Bang "Hole-Size Increasing PCFs for Blue-Extended Supercontinuum Generation," to be presented at CLEO/Europe and EQEC 2013, paper CD-P.45.

## Scientific reports outside the scope of the thesis

The following journal and conference papers were published during the course of the project, but lie outside the scope of this thesis.

**Paper IX**

C. Agger, S. T. Sørensen, C. L. Thomsen, S. R. Keiding, and O. Bang, "Nonlinear soliton matching between optical fibers," Opt. Lett. **36**,

2596-2598 (2011).
http://dx.doi.org/10.1364/OL.36.002596

**Paper X**

C. Larsen, S. T. Sørensen, D. Noordegraaf, K. P. Hansen, K. E. Mattsson, O. Bang, "Zero-dispersion wavelength independent quasi-CW pumped supercontinuum generation," Opt. Comm. **290**, 170-174 (2013).
http://dx.doi.org/10.1016/j.optcom.2012.10.030

**Conference XVI**

C. Agger, S. T. Sørensen, C. L. Thomsen, S. R. Keiding, and O. Bang, "Nonlinear matching of Solitons - Continued redshift between silica and soft-glass fibers," in CLEO: QELS-Fundamental Science, OSA Technical Digest (Optical Society of America, 2012), paper QF1G.8.

# Acronyms

| | |
|---|---|
| CW | Continuous wave |
| DW | Dispersive wave |
| FWHM | Full-width at half-maximum |
| FWM | Four-wave mixing |
| GAM | Group acceleration mismatch |
| GNLSE | Generalised nonlinear Schrödinger equation |
| GV | Group velocity |
| GVD | Group velocity dispersion |
| HOM | Higher-order moment |
| IR | Infrared |
| MI | Modulation instability |
| NLSE | Nonlinear Schrödinger equation |
| PCF | Photonic crystal fibre |
| RIN | Relative intensity noise |
| SC | Supercontinuum |
| SPM | Self-phase modulation |
| UV | Ultraviolet |
| XPM | Cross-phase modulation |
| ZDW | Zero-dispersion wavelength |

Chapter 1

# Introduction

Supercontinuum (SC) generation is a spectacular phenomenon of extreme spectral broadening involving a plenitude of nonlinear physics [1,2]. Following the first observation of SC generation in bulk glass in the 1970s [3,4], the field was taken to optical telecom fibres [5,6]. However, the full potential of SC generation that pushed the technology from a mere laboratory curiosity to the development of today's commercial sources was first realised with the invention of the photonic crystal fiber (PCF) in the late 1990s [7–12], in which light can be manipulated by tailoring the PCF's air hole structure. Because of the unprecedented design freedom of the guiding properties that were impossible in bulk materials and standard optical fibres, the advent of the PCF spawned a renaissance of nonlinear optics in general and SC generation in particular [13]. Specifically, by design optimisation the zero-dispersion wavelength (ZDW) can be tuned into the visible [14]; the fibre can be made endlessly single-mode [15] or even guide light in air [16].

SC generation in PCFs is synonymous with soliton physics: when long pico or nanosecond pulses, or even continuous waves (CWs), are launched into the fibre, the process of modulational instability (MI) induces a temporal break-up that splits the pulse envelope into a distributed spectrum of solitons [17–23]. As it turns out, the subsequent soliton propagation and interactions are in fact the main driving mechanism behind the spectral SC broadening. Modulational instability is a universal physical phenomenon, in which a weak modulation of a wave experience an exponential growth [13, 24–26]. In the specific context of fibre optics, the modulation builds from quantum noise and results in large spectral shot-to-shot variations. A closer inspection of these variations led to the surprising observation of optical rogue waves [27]; statistically rare solitons with peak powers significantly above the mean. Because of their statistical nature, these op-

tical rogue waves constitute an analogue to rogue phenomena found in such diverse systems as ocean waves, where they appear out of nowhere and cause serious damage on ships and oil rigs [28–30], finance [31] and biology [32].

It is thus clear that SC generation in PCFs provides an excellent platform for investigating important fundamental effects and their links with other physical systems. Amongst the numerous effects discovered in this context are soliton fission [33], Raman redshift cancellation by the presence of a second ZDW [34], and soliton trapping of dispersive waves (DWs) in gravitational wells [35–37]. The latter is principal for SC generation, where the long wavelength spectral "red" edge is comprised of solitons and the short wavelength spectral "blue" edge by trapped DWs. The trapping mechanism thus manifests itself as a lock between the two edges separated by upto multiple optical octaves: when the distributed spectrum of MI-generated solitons are redshifted by the Raman effect, they trap DWs across the ZDW and force them to blueshift so as to satisfy group velocity (GV) matching with the solitons [35, 38]. With a clever engineering of the GV landscape, the SC dynamics can therefore be harnessed to generate certain spectral qualities, such as an enhancement of the blue edge [38–40].

Commercial SC sources saw the light of day in 2003 (NKT Photonics A/S) and have since been established as a mature and reliable technology. As an example of their versatile applicability, Leica's new generation TCS SP8 X confocal microscope for fluorescence microscopy allows up to eight continuously tunable excitation lines to be picked simultaneously from a single SC sources. High-power commercial SC sources are typically based on long-pulsed fibre lasers, resulting in bright spectra with more than one optical octave of bandwidth. These sources are characterised by a low temporal coherence and high spatial coherence, making them suitable for a range of sophisticated spectroscopy and imaging techniques, such as optical coherence tomography [41–43] and fluorescence lifetime imaging [44, 45]. Broadly speaking, the SC technology has great potential in fields where a single SC source can replace an array of lasers operating at different wavelengths, although the technology has also found applications in areas requiring ultrahigh precision, such as the development of ultra-stable optical clocks [46–50]. The potential of the SC field is highlighted by the immense growth over the last ten years, and it was recently estimated that the market for SC sources has an annual sales potential in excess of $150M [51]. The future of the fibre-based SC field seems to point to the development of cheap high-power SC sources based on (quasi) CW lasers [52–54], fully coherent SC sources in all-normal PCFs [55–61], and extending the SC spectrum into the infrared (IR) in nonsilica glasses with higher nonlinearities and/or low transmission loss in the mid-IR [62–65] or into the deep-blue and ultraviolet

(UV) with dispersion engineering [40, 66–69].

In this work we pursue two such goals: (1) to extend the SC into the deep-blue by manipulating the spectral development with dispersion engineering in tapered PCFs; and (2) to lower the spectral shot-to-shot noise by controlling either the initial MI dynamics by modulating the input pulse with a weak seed or the subsequent soliton-driven dynamics with tapered fibres. These goals are motivated by a direct commercial relevance: the entire visible part of the electromagnetic spectrum is very important for biological applications in, e.g. high resolution imaging with confocal microscopy and studies of ultrafast temporal responses with fluorescence lifetime imaging, as well as optical coherence tomography [41, 44, 45, 70]. However, most commercial sources are limited to 450-500 nm and hence cannot be used to access the biologically relevant deep-blue spectral region. Similarly, low shot-to-shot fluctuations are required in many applications where, e.g. the dynamics of a biological system is studied on a time scale comparable to the repetition rate of the light source, and in optical coherence tomography where low-noise femtosecond lasers remain the preferred choice over SC sources, despite their more attractive spectral properties. Indeed, the limited spectral shot-to-shot stability is currently one of the main drawbacks facing commercial long-pulsed SC sources.

## 1.1 Outline

This thesis compiles the main research results obtained during the author's PhD study. The thesis is divided into five chapters including this introduction and a summary, followed by an appendix with complementary information and the scientific journal publications Papers I-VIII published during the study (note: due to copyright ownership the full articles are not included in the online version of the thesis). The thesis should be considered a compliment to these eight scientific journal publications, and contains the necessary background information to make the thesis and publications self-contained. In addition to this background information, the thesis highlights the main results of Papers I-VIII in a coherent manner. This inevitably introduces a degree of repetition between the thesis and publications.

An introduction to nonlinear pulse propagation in microstructured optical fibres is presented in Chapter 2. The chapter is intended to establish a frame of reference to understand long-pulsed SC generation and the results presented in the following chapters. Specifically, Chapter 2 summarises the basic theory of linear and nonlinear fibre optics with a clear focus on SC generation.

In Chapter 3 we explain how dispersion engineering can be utilised to extend and enhance SC generation into the deep-blue in tapered PCFs. The chapter reviews the results of Papers I-IV plus additional unpublished results. In particular, we introduce the concept of group acceleration matching that allows us to optimise the blue edge of an SC. This is demonstrated with an array of experimental results, including the first PCF with longitudinally varying pitch and hole-size for deep-blue SC generation.

Chapter 4 discusses the noise properties of long-pulsed SC generation. Specifically, we characterise the noise properties with statistical high-order moments as described in Paper V, which provides direct insight into the nature of the noise across the spectrum. Following this, we numerically examine noise reduction by modulating the pump with a seed and experimentally by taming the SC dynamics with tapered fibres, similar to those used in Chapter 3. These results relate to Papers VI-VII and Papers III and VIII, respectively. Particular emphasis is given on the noise properties in the commercially relevant high-power regime, which has remained relatively unexplored.

Chapters 3–4 are concluded individually, and a final summary of the thesis is given in Chapter 5. Additionally, a description of the numerical modelling and the eight scientific journal publications are included as appendices.

Chapter 2

# Pulse propagation in nonlinear optical fibres

The interaction of light and matter has been extensively studied for decades. Today it is well established that light can cause matter to oscillate on an atomic or molecular level, which in turn re-emits light that interferes with the original light, and that this interaction is described by the Maxwell equations. Thanks to this understanding it is today possible to control light by engineering the medium in which it propagates. In optical fibres light is subject to *dispersion* and, if the intensity is sufficiently high, a *nonlinear* electronic response called the *Kerr effect*. That is, the refractive index depends on both the frequency and intensity of the light, which disperses the different frequencies of the light as it propagates and leads to the generation of light at new frequencies, respectively. Light can further interact with the molecular vibrations of the medium through the *Raman effect*.

The scope of this chapter is to give a condensed introduction to the physics of pulse propagation in nonlinear optical fibres, so as to make this thesis self-contained. Emphasis is given on the basic mathematical and physical background needed to understand the driving mechanisms in SC generation. An in-depth treatment is easily found elsewhere, see e.g. the book by Agrawal [71] and the 2006 review on SC generation by Dudley *et al.* [1].

## 2.1 Linear propagation

An electromagnetic field can be constrained by the physical boundaries of a waveguide, such a singlemode optical fibre, where guiding is achieved

by surrounding the core region with a lower refractive index cladding. An electric field $\mathbf{E}(\mathbf{r}, t)$ propagating in the fundamental mode of an optical fibre can be mathematically described as

$$\mathbf{E}(\mathbf{r}, t) = \hat{x} \left\{ F(x, y) A(z, t) \exp\left[ i(\beta_0 z - \omega_0 t) \right] \right\}, \tag{2.1}$$

where the field is assumed linearly polarised along the $\hat{x}$-direction. $F(x, y)$ is the transverse field distribution, $A(z, t)$ is pulse envelope and $\beta_0 = \beta(\omega_0)$ the propagation constant at pulse centre frequency $\omega_0$, which specifies the phase change per unit length.

### 2.1.1 Dispersion

One of the key parameters of optical fibres is the dispersion, or the frequency dependence of the refractive index $n(\omega)$. Dispersion originates partly from the frequency dependence of the response of silica to electromagnetic waves, and partly from frequency dependencies associated with the geometry and confinement of the waveguide. These two components are referred to as *material* and *waveguide dispersion*, respectively. Dispersion is mathematically accounted for by Taylor expanding the propagation constant about the pulse centre frequency [71]

$$\beta(\omega) = n(\omega)\frac{\omega}{c} = \beta_0 + \beta_1(\omega - \omega_0) + \frac{1}{2}\beta_2(\omega - \omega_0)^2 + \cdots, \tag{2.2}$$

where $c$ is the speed of light and the $\beta_m$ coefficients are given by

$$\beta_m = \left. \frac{\partial^m \beta(\omega)}{\partial \omega^m} \right|_{\omega = \omega_0}. \tag{2.3}$$

The parameters $\beta_1$ and $\beta_2$ are particularly important in fibre optics. The *group velocity* $v_g$, i.e. the velocity with which the pulse envelope propagates, is directly related to $\beta_1$

$$v_g = \left( \frac{\partial \beta(\omega)}{\partial \omega} \right)^{-1} = \beta_1^{-1}. \tag{2.4}$$

The frequency dependence of $v_g$ leads to pulse broadening of short pulses, and this *group velocity dispersion* (GVD) (or simply dispersion) is related to the GVD parameter $\beta_2$

$$D = \frac{\partial \beta_1}{\partial \lambda} = -\frac{2\pi c}{\lambda^2}\beta_2, \tag{2.5}$$

where $\lambda$ is the wavelength. Dispersion parameters $\beta_m$ of third and higher order are called higher-order dispersion.

The sign and magnitude of $\beta_2$ are crucial for most nonlinear processes in optical fibres. A region with $\beta_2 > 0$ ($D < 0$) is said to have *normal dispersion* and a region with $\beta_2 < 0$ ($D > 0$) *anomalous dispersion*. Normal dispersion means that the GV increases with wavelength, and that short wavelength "blue" components of a pulse travels slower than its longer wavelength "red" components. The opposite is true for regions with anomalous dispersion. The crossing point is called the *zero-dispersion wavelength* (ZDW). Efficient nonlinear conversion requires extended interaction with propagation of pulses at different wavelengths. The nonlinear interaction can thus be limited by temporal walk-off if the pulses (or frequency components) propagate with different GV, and accurate control of the dispersion is a clear prerequisite for manipulating nonlinear processes.

### 2.1.2 Photonic crystal fibres

Single-mode optical fibres consist of a small core surrounded by a cladding with a lower refractive index (Fig. 2.1(a)). They are typically made from fused silica glass and the index difference is controlled by dopants. Light is guided in the core due to *total internal reflection* at the boundary between the core and cladding. In contrast, *photonic crystal fibres* (PCFs) have a fundamentally different design with a complex cladding made of an array of air holes running along the length of the fibre, resembling the structure of a photonic crystal. In solid-core PCFs (Fig. 2.1(b)), the periodicity is broken by introducing a solid core, which enables light guidance in the core by a modified total internal reflection due to a lower (effective) refractive index of the air hole-surrounding relative to the core [9–11]. The first solid-core PCF was demonstrated in 1995 [7, 8], but the idea of guidance in single-material fibres was attempted as early as the 1970s [72]. In another class of PCFs light is guided in a hollow core by a photonic bandgab effect [73–75] (Fig. 2.1(c)).

PCFs can be drawn on conventional fibre draw-towers. The preform is typically made by stacking silica tubes in a close-packed array, where the core is shaped simply by placing a solid tube in the centre of the preform.

The cladding index of PCFs has a much greater wavelength dependence than that of conventional fibres, as the light distribution in the air and glass varies with wavelength. This enables endlessly single-mode operation [15], but also makes calculations of the fibre properties more difficult, and must be numerically determined with e.g. a finte-element solver. The design of the air holes allows a unique engineering of the dispersive and nonlinear properties [76], which offers unprecedented control of nonlinear processes. In particular, the success of PCFs lies in the easy tunability of the ZDW to

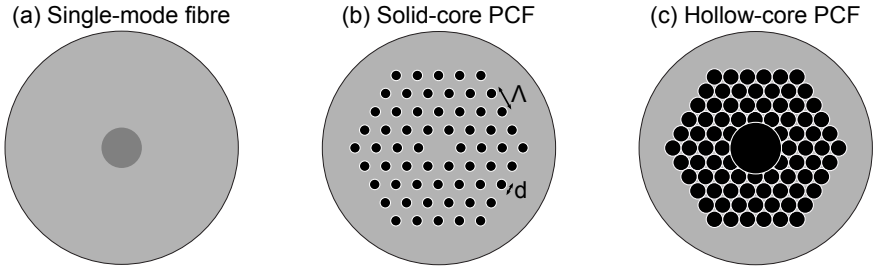


**Figure 2.1:** Schematic illustration of fibre cross-section of the fibre types discussed in the text. Grey areas are glass and black areas are hollow. The pitch $\Lambda$ and hole size $d$ are marked in (b).

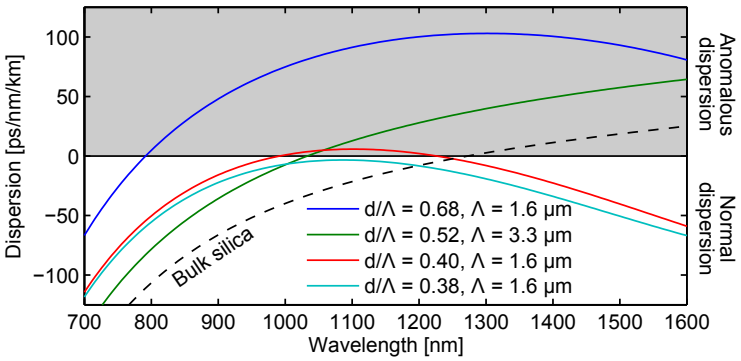


**Figure 2.2:** Dispersion profiles of solid-core PCFs with different hole size ($d$) and pitch ($\Lambda$). The dispersion of bulk silica is from [71].

match the wavelength of commercially available lasers. This is illustrated in Fig. 2.2, where the dispersion landscape is controlled to match the ZDW to a pump wavelength of either 800 or 1064 nm, and further to bring the second ZDW close to the pump or even have normal dispersion at all wavelengths. By controlling the waveguide dispersion it is thus possible to create fibres with properties very different from bulk silica.

### Modal properties

Optical fibres can support a number of guided modes depending on the fibre design and wavelength; the modes differ in transverse amplitude profiles and propagation constant. Throughout this thesis we will only consider propagation in the *fundamental mode* of a solid-core PCF, which is charac-

terised by the largest effective index and a symmetric intensity profile. In fibres with circular symmetry, the fundamental mode is two-fold degenerate with orthogonally polarized modes. The fibre properties considered here were calculated with the commercial finite-element solver COMSOL from a specified fibre geometry and appropriate choice of boundary conditions.

**Attenuation**

The attenuation in PCFs comes partly from the intrinsic material loss of the silica host material and partly from various sources of imperfections [10, 11, 71]. The PCF production causes imperfection in the form of structural defects and contaminations leading to additional extrinsic losses. PCFs are particularly exposed to water-related losses, where an overtone of OH-silica bond absorption causes attenuation at 1.38 $\mu$m [77]. The material loss of pure silica is low in the range 500-2000 nm, but increases towards the ultraviolet and mid-infrared due to electronic and vibrational resonances, respectively [78]. Scattering from surface roughness at the air-silica boundaries can be significant due to the large index contrast [79–81]. This becomes an increasing problem when the intensity of the guided mode is high at the boundaries, like for the small cores in the tapered PCFs considered in this thesis. Similarly, OH losses are known to increase with decreasing core size [82]. Confinement losses occur when a guided mode has a substantial evanescent field in the cladding, which can be mitigated by increasing the number of air hole rings. Appendix A includes a discussion on how to treat the dominating sources of attenuation when modelling SC generation, and attenuation in tapered PCFs is further discussed in Chapter 3.

## 2.2 Nonlinear propagation

From Maxwell's equations it can be shown that an electromagnetic field propagating in an isotropic medium with no free charges obeys the wave equation [71]

$$\nabla \times \nabla \times \mathbf{E}(\mathbf{r},t) = -\frac{1}{c^2}\frac{\partial^2 \mathbf{E}(\mathbf{r},t)}{\partial t^2} - \mu_0 \frac{\partial^2 \mathbf{P}(\mathbf{r},t)}{\partial t^2}, \tag{2.6}$$

where $\mu_0$ is the free space permeability and $\mathbf{P}(\mathbf{r},t)$ is the electric polarisation. A high-intensity electromagnetic field can give rise to a nonlinear response of a dielectric medium, which in turn can generate light at new frequencies. This happens when the motion of the bound electrons becomes anharmonic. The nonlinear response of the induced polarisation to an electromagnetic field can be described by a Taylor expansion in the electric field

when operating far from any resonances of the medium [71]

$$\mathbf{P}(\mathbf{r},t) = \epsilon_0 \left(\chi^{(1)} + \chi^{(2)}\mathbf{E}(\mathbf{r},t) + \chi^{(3)}\mathbf{E}(\mathbf{r},t)\mathbf{E}(\mathbf{r},t) + \cdots\right)\mathbf{E}(\mathbf{r},t), \quad (2.7)$$

where $\chi^{(n)}$ is the $n$th order *susceptibility*. The linear susceptibility $\chi^{(1)}$ is the dominating effect; its real and imaginary parts are related to the refractive index and attenuation, respectively. Due to the centrosymmetry of silica all even-order terms vanish. As a consequence, effects like second-harmonic and sum-frequency generation associated with the second order susceptibility $\chi^{(2)}$ do (normally) not occur in silica fibres.

The lowest-order nonlinear effects in silica fibres can hence be associated with $\chi^{(3)}$, which gives rise to the Kerr effect and Raman scattering. The former manifests itself as an intensity dependent modification of the refractive index, which leads to phenomena such as *self-phase modulation* (SPM), *cross-phase modulation* (XPM) and *four-wave mixing* (FWM) that are discussed in the following. In its simplest form, the intensity dependent contribution to the refractive index can be written as

$$\Delta n = n_2|E|^2; \qquad n_2 = \frac{3}{8n}\mathrm{Re}(\chi^{(3)}_{xxxx}), \quad (2.8)$$

where $|E|^2$ is the optical intensity and Re denotes the real part. Many of the components of $\chi^{(3)}$ can be zero for symmetry reasons, and for a linearly polarized field only the $\chi^{(3)}_{xxxx}$ component is non-zero. The nonlinearity can then be quantified through the nonlinear refractive index of silica $n_2 \approx 2.6 \cdot 10^{-20}$ m$^2$/W [71].

A propagation equation for the pulse envelope that includes dispersive and nonlinear $\chi^{(3)}$ effects can be derived from the wave equation Eq. (2.6). It assumes that the nonlinearity is small (i.e. that the nonlinear polarisation can be treated as perturbation) and that the bandwidth is less than $\sim$1/3 of the carrier frequency [83]. The result is the scalar *generalised nonlinear Schrödinger equation* (GNLSE) in the retarded time frame $\tau = t - z/v_g$ [83]

$$\frac{\partial A}{\partial z} = i\sum_{m\geq 2}\frac{i^m\beta_m}{m!}\frac{\partial^m A}{\partial \tau^m} - \frac{\alpha}{2}A + i\gamma\left(1 + i\tau_{\mathrm{shock}}\frac{\partial}{\partial\tau}\right)\left(A(z,\tau)\int_{-\infty}^{+\infty} R(\tau')|A(z,\tau-\tau')|^2 d\tau'\right). \quad (2.9)$$

The complex pulse envelope is normalised such that $|A(z,t)|^2$ gives the instantaneous power. The sum on the right hand side of Eq. (2.9) describes dispersion and $\alpha$ is the loss. The nonlinearties are quantified by the *nonlinear coefficient*

$$\gamma = \frac{n_2(\omega_0)\omega_0}{cA_{\mathrm{eff}}}, \quad (2.10)$$

where the *effective area* of the mode $A_{\text{eff}} = (\int |\mathbf{E}|^2 dA)^2 / \int |\mathbf{E}|^4 dA$ depends on the modal distribution integrated over the $xy$ plane [71, 84]. The time derivative in Eq. (2.9) describes the dispersion of the nonlinearity and is characterised by a time scale $\tau_{\text{shock}} = 1/\omega_0$ [1, 71], which leads to effects like *self-steepening*. $R(t)$ is the nonlinear response function of silica

$$R(t) = (1 - f_R)\delta(t) + f_R h_R(t), \tag{2.11}$$

which comprises two effects: (1) the electronic response, which is assumed instantaneous and hence described by the delta function $\delta(t)$, and (2) the delayed Raman response $h_R(t)$ originating from phonon interactions [83]. $f_R = 0.18$ is the relative strength of the Kerr and Raman interactions.

When neglecting all terms except the GVD and instantaneous Kerr nonlinearity, the GNLSE reduces to the standard *nonlinear Schrödinger equation* (NLSE) [71]

$$\frac{\partial A}{\partial z} = -i\frac{\beta_2}{2}\frac{\partial^2 A}{\partial \tau^2} + i\gamma A|A|^2. \tag{2.12}$$

The NLSE is the simplest nonlinear equation for studying $\chi^{(3)}$ effects.

### 2.2.1 Numerical solutions

Analytical solutions to the GNLSE only exist in few highly simplified cases rendering numerical integration the obvious approach to the full problem. Numerical solutions to the GNLSE have been demonstrated to produce spectra and noise properties in good - occasionally excellent - agreement with experiments over a large range of input conditions, see e.g. [1]. The numerical modelling in this thesis is based on the particular implementation by Lægsgaard [85] that directly includes the frequency dependence of the effective area. The GNLSE is solved in the interaction picture [86] by an adaptive step-size fourth order Runge-Kutta solver. The implementation is detailed in Appendix A together with some useful tricks. The mode profile and effective area were calculated with the finite element mode solver COMSOL and will not be discussed here. It should be noted that Eq. (2.9) preserves the number of photons if loss is neglected, but energy is not preserved due to the photon-phonon energy transfer through the Raman effect [71].

It is often important to include a noise background in the simulations. This is commonly done with the *one photon per mode* model by injecting a fictitious field consisting of one photon with a random phase in each spectral discretisational bin. Additional noise sources are discussed in Chapter 4 and Appendix A.

The numerical results can be visualised in various ways. In the time domain, the pulse envelope is directly related to the instantaneous power

$P(t) = |A(t)|^2$, as mentioned above. The frequency domain envelope $\tilde{A}(\omega)$ is then simply given by the Fourier transform of $A(t)$. However, when comparing to experiments, it is often more convenient to show the power spectral density $\mathrm{PSD}(\omega) = c/\lambda^2 f_{\mathrm{rep}} |\tilde{A}(\omega)|^2$, where $f_{\mathrm{rep}}$ is the repetition rate. The spectrogram or time-frequency representation gives an excellent characterisation of the complex pulse dynamics, which is particularly useful for correlating temporal and spectral features. It is found by gating the field with a gate function $g(t-\tau)$ with variable delay $\tau$, $S(\tau,\omega) = |\int A(t) g(t-\tau) \exp(-i\omega t) dt|^2$. Experimentally, the spectrogram can e.g. be measured using the frequency-resolved optical gating (FROG) technique [87, 88].

### 2.2.2 Self-phase and cross-phase modulation

The Kerr effect entails that the phase-velocity $v_p = c/n$ becomes intensity dependent, which leads to a self-phase modulation of a propagating pulse [89, 90] and a cross-phase modulation of co-propagating pulses [91–93].

The effects of SPM are easily observed from the NLSE (Eq. (2.12)) by neglecting GVD ($\beta_2 = 0$), which has the general solution [71]

$$A(z,\tau) = A(0,\tau) \exp(i\phi_{\mathrm{NL}}(z,\tau)); \quad \phi_{\mathrm{NL}}(z,\tau) = \gamma |A(0,\tau)|^2 z. \tag{2.13}$$

It is clearly seen that the temporal pulse shape $|A(z,\tau)|^2$ remains unchanged with propagation, while the pulse acquires a phase shift $\phi_{\mathrm{NL}}(z,\tau)$ that depends on the initial pulse shape and chirp. The time dependence of the phase shift leads to spectral changes: in general, for an unchirped Gaussian-like pulse, the leading edge will be downshifted in frequency and the trailing edge upshifted, respectively, which spectrally broadens the pulse [90].

The intensity dependence of the GV leads to self-steepening because the pulse peak moves at a lower speed than the edges. In combination with SPM this causes an asymmetric spectral broadening; for ultrashort pulses it shifts the pulse peak to the trailing edge with propagation, which ultimately creates an optical shock [71].

In addition to SPM, the Kerr effect implies that the refractive index can be modulated by the intensity of a co-propagating wave through XPM. The nonlinear phase shift experienced by a field $A_1$ in the presence of a co-propagating field $A_2$ at a different frequency can be approximated by [71]

$$\phi_{\mathrm{NL},1}(z,\tau) \approx \gamma(|A_1(0,\tau)|^2 + 2|A_2(0,\tau)|^2) z, \tag{2.14}$$

and similarly for the phase shift of $A_2$. The first term is due to SPM and the second term is from XPM, which is seen to be twice as effective. It is important to notice that two waves can interact through XPM without

any transfer of energy. XPM depends strongly on the GVs of the involved waves to prevent temporal walk-off. This point is very important for SC generation, as we shall see.

### 2.2.3 Four-wave mixing and modulation instability

Four-wave mixing is a parametric $\chi^{(3)}$ process. As the name suggests, the process involves light at four (not necessarily distinct) frequencies that mix together in a way that satisfies energy and momentum conservation [71, 94–96]. When light with frequencies $\omega_1$ and $\omega_2$ propagate in a $\chi^{(3)}$ medium, it can induce harmonics in the polarisation, which generates light at $\omega_3 = \omega_1 - (\omega_2 - \omega_1) = 2\omega_1 - \omega_2$ and $\omega_4 = \omega_2 + (\omega_2 - \omega_1) = 2\omega_2 - \omega_1$. The process can thus be used to parametrically amplify a pre-existing frequency at $\omega_3$ or $\omega_4$. And the FWM amplified frequencies can further interact with each other to generate a full comb of equidistantly spaced frequency components. This technique is utilised in Chapter 4.

Phase-matching is a prerequisite for FWM, and the process can be made very efficient in fibres by controlling the dispersion to ensure a vanishing phase-mismatch $\Delta k = \beta(\omega_3)+\beta(\omega_4)-\beta(\omega_1)-\beta(\omega_2)+2\gamma P_0 \approx 0$, where $2\gamma P_0$ is the nonlinear phase [71, 95, 96]. In a special case of FWM, two *degenerate* pump photons drive the generation of a Stokes/anti-Stokes photon pair at frequencies symmetrically positioned about the driving frequency. This automatically ensures phase-matching of the driving field.

*Modulation instability* is a nonlinear phenomenon in which amplitude and phase modulations of a wave experience growth. A weak perturbation of a continuous or quasi-continuous wave background can, if it falls within a certain frequency range, undergo an exponential amplification that breaks the wave into a pulse train. Although first observed in hydrodynamics [97], the MI process is recognised a universal process in nonlinear physics [13, 24–26]. In the specific context of fibre optics, MI is a consequence of the interplay between dispersive and nonlinear Kerr effects, resulting in an exponential amplification of a weak perturbation that is known to induce a break-up of quasi-continuous waves into trains of temporally short pulses [17, 22, 23, 26, 98]. The perturbation can be either quantum noise (spontaneous MI) or a signal with a frequency shift relative to the pump (induced MI). In the frequency domain, MI is a degenerate FWM process where two pump photons are converted to a Stokes/anti-Stokes photon pair and can be associated with a modulation frequency $\Delta\omega_{\mathrm{MI}} = (2\gamma P/|\beta_2|)^{1/2}$ [99].

### 2.2.4 Raman scattering

The electronic responses that give rise to Kerr nonlinearities are effectively instantaneous. In contrast, Raman scattering of light by molecular vibrations (phonons) is a non-instantaneous $\chi^{(3)}$ process. In *spontaneous* Raman scattering, a photon is downshifted in frequency by transferring some of its energy to a phonon [100] or upshifted by combining with a phonon. The downshifted and upshifted radiation are referred to as a Stokes and anti-Stokes wave, respectively. The latter process occurs less frequently as it requires a phonon of the right energy and momentum. It is similarly possible to utilise Raman scattering for *stimulated* amplification of a Stokes signal by a suitable pump. Spontaneous Raman scattering can act as a seed for further stimulated amplification [71].

The molecular vibrations of silica induced by an optical field can to a fair approximation be described by a simple damped oscillator model [71,83]

$$h_R(t) = \frac{\tau_1^2 + \tau_2^2}{\tau_1 \tau_2^2} \exp(-t/\tau_2) \sin(t/\tau_2) \Theta(t), \tag{2.15}$$

with $\tau_1 = 12.2$ fs and $\tau_2 = 32$ fs. $\Theta(t)$ is the unit step function. The Raman gain (i.e. the gain seen by a weak Stokes signal with a frequency offset relative to the pump) is given by the imaginary part of $h_R(t)$ in the frequency domain. The simple Raman gain is shown together with the full Raman response in Fig. 2.3. The simple model reproduces the overall shape of the full Raman gain and both show a clear maximum at ∼13.2 THz. Equation (2.15) has been used extensively for modelling pulse propagation with good results [1] and was used in this work. However, the model tends to underestimate the Raman-induced frequency shifts that will be discussed in the following [71].

## 2.3 Solitons and solitonic effects

In optical fibers with anomalous dispersion, the chirp from SPM can be exactly compensated by dispersion. This leads to one of the most intriguing phenomena in nonlinear physics: *the soliton*, a translational solitary wave that retains its shape with propagation. Solitons are known from a wide range of nonlinear systems and were first discovered in the early 1800s in the form of water waves [102]. The propagation of solitons in optical fibres was first considered in 1973 by Hasegawa and Tappert [103] and experimentally observed in 1980 by Mollenauer *et al.* [104], although optical solitons were in fact unknowingly generated in 1978 by Lin *et al.* [6].

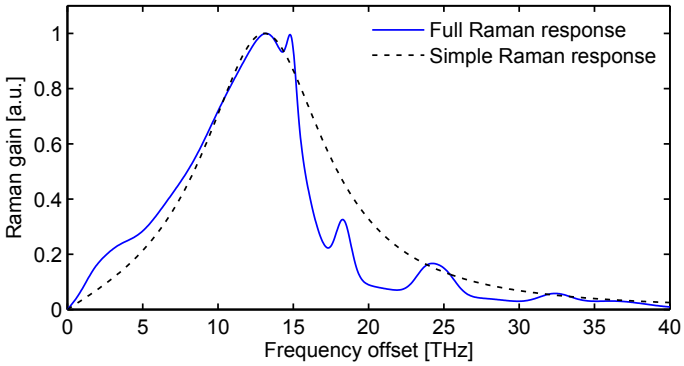


**Figure 2.3:** Normalised Raman gain spectrum of silica. The frequency offset is of the (weak) Stokes signal wave with respect to the pump. The full Raman response is based on [101].

Mathematically, solitons are exact solutions to the NLSE of the form [71]

$$A(z,\tau) = \sqrt{P_0}\mathrm{sech}\left(\frac{\tau}{\tau_0}\right)\exp\left(-i\frac{|\beta_2|}{2\tau_0^2}z\right), \tag{2.16}$$

where the width $\tau_0$ and peak power $P_0$ are related through the *soliton number*

$$N^2 = \frac{\gamma P_0 \tau_0^2}{|\beta_2|}, \tag{2.17}$$

and the exponential function represents the nonlinear phase shift attained with propagation. *Fundamental solitons* have $N = 1$ and propagate without any change in temporal or spectral shape. Higher-order solitons have integer soliton numbers $N > 1$ and periodically return to their initial shape. However, the term soliton typically refers to a fundamental soliton, as we shall do here.

One of the most remarkable features of solitons is the stability: near-solitonic pulses automatically adjust their shape to that of a fundamental soliton, possibly by dispersing excess energy. Solitons are similarly known to be stable under small perturbations, such as losses and amplification [103,105–107] as well as changes in dispersion and nonlinearity [22,108]. The changes just need to be sufficiently slow for the soliton to *adiabatically* adjust its shape. Because of the stability solitons were quickly suggested as candidates for optical communication [105, 106, 109, 110]. In contrast, higher-order solitons are not stable under perturbations, rather they un-

dergo *soliton fission* that breaks the higher-order soliton into its fundamental soliton constituents [35, 71, 111].

### 2.3.1 Soliton self-frequency shift

The spectrum of a temporally narrow soliton can be sufficiently broad for the short wavelength components of the soliton to act as a Raman amplifier for the long wavelength components [112]. This intra-pulse Raman scattering transfers energy from the blue to the red edge, which effectively shifts the soliton to gradually longer wavelengths, a phenomenon called the *soliton self-frequency shift* [113, 114]. The Raman gain is weak for small frequency offsets, as seen in Fig. 2.3. This causes a strong dependence of the redshift rate on the soliton duration that can be approximated by $\partial\omega_s/\partial z \propto -|\beta_2|/\tau_0^4$ for long pulses [114]. The self-shift rate (generally) slows down with propagation because energy is lost in the Raman process and the pulse broadens temporally.

The Raman self-frequency shift can be used to access spectral regions that are hard to reach with existing lasers. In Paper IX we investigated the possibility of coupling an ensemble of redshifting solitons between two different fibres, while ensuring that the solitons remain solitons without shedding energy. This can e.g. be utilised to extend the redshift of multiple co-propagating solitons into the mid-infrared by coupling them from a silica to a softglass fibre. However, this will not be discussed further in this thesis.

### 2.3.2 Dispersive wave generation

A soliton can, in the presence of higher-order dispersion, resonantly transfer energy into the normal dispersion regime to a so-called *dispersive wave* or *Cherenkov* radiation [115]. The amplification of DW radiation conditions resonant coupling, i.e. phase-matching from the soliton to the DW. This can occur for solitons in the vicinity of a ZDW with spectral components extending into the normal dispersion regime, so that the centre of the soliton can resonantly amplify its own spectral tail with propagation [116, 117]. A cancellation of the self-frequency shift has been demonstrated by a mechanism where a redshifting soliton slows down as it approaches a long-wavelength ZDW [34], which causes a recoil of the soliton due to phase-matched energy transfer across the ZDW.

Recently, Erkintalo *et al.* [118] identified phase-matched cascaded FWM as the driving mechanism in DW generation from soliton-like pulses perturbed by higher-order dispersion, where a bichromatic pump pair within the soliton spectrum generates frequencies in the opposite dispersion regime.

This directly explains the soliton recoil observed near a second ZDW and DW generation in the anomalous dispersion regime from pulses in the normal dispersion regime [119]. Also recently, it was demonstrated by Rubino *et al.* [120] that the soliton has an additional phase matched component in the negative frequency branch of the dispersion that can generate DWs at even shorter wavelengths. This can be understood by noting that an electromagnetic field is a real function, and can hence be described as a positive frequency envelope and its complex (negative frequency) conjugate, where the latter gives rise to additional phase-matching conditions [120, 121].

### 2.3.3 Trapping of dispersive waves

The dispersive radiation generated from a soliton typically propagates at a lower GV than the soliton, preventing any immediate interaction. However, as the soliton redshifts it decelerates, which eventually allows the soliton and DW to interact through a cascade of XPM collisional events. This leads to the fascinating phenomenon of *pulse trapping*, where the redshifting soliton traps the DW and forces it with to move with the GV of the soliton [35–37, 122–126]. This effect is principal for SC generation and its implications will be discussed in greater detail in Chapter 3. The manifestation of the trapping effect is demonstrated in Fig. 2.4, which shows the propagation of a 25 fs fundamental soliton and a GV matched DW package in a typical PCF with a ZDW at 1054 nm (the modelling in Chapter 4 is based on the same fibre). The spectral evolution in Fig. 2.4(a) shows how the soliton forces a continuous blueshift of the DW with propagation, so as to satisfy GV matching. This is detailed in the spectrograms in Fig. 2.4(b) for the soliton and DW, the soliton alone and the DW alone, respectively. When both pulses are present, the DW is trapped by the soliton, which forces it to propagate at the GV of the soliton and keeps the DW from dispersing. The soliton undergoes nearly the same redshift in the absence of the DW, although a small change in the final delay is observed. In contrast, when the DW propagates alone it is subject to significant dispersion, which clearly highlights the trapping effect.

The trapping effect has been explained as a consequence of XPM and the soliton deceleration: The soliton induces a modulation of the refractive index across the DW via XPM, which effectively creates a potential barrier that forces the DW to trail behind the soliton. In addition, the soliton deceleration imposes a gravity-like force on the DW, preventing it from dispersing behind the soliton. These two effects combined thus creates a gravity-like potential that effectively traps the DW and forces it to follow the GV of the soliton. This was first explained by Gorbach and Skryabin [37]

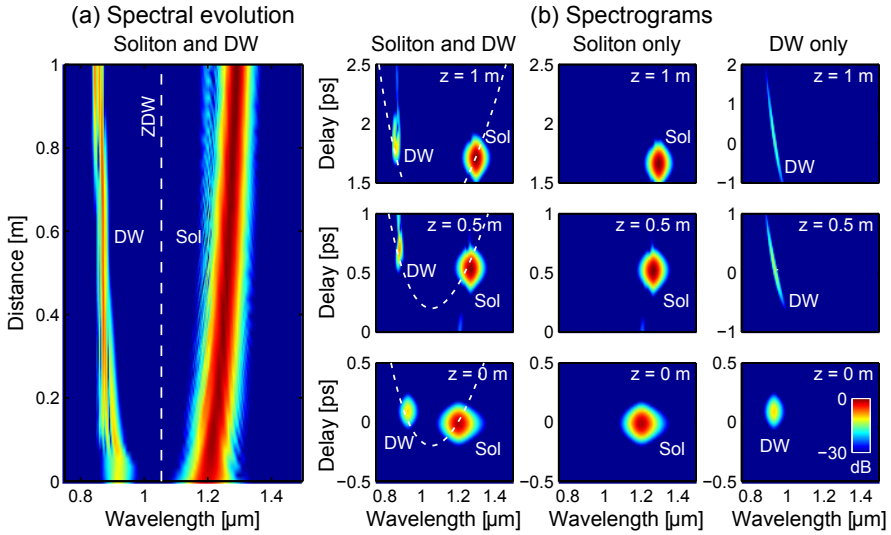


**Figure 2.4:** (a) Propagation of a fundamental soliton ($\lambda_s = 1200$ nm, $\tau_0 = 25$ fs, $P_0 = 10.2$ kW) and GV matched DW (sech$^2$-shape, $\lambda_{DW} = 925$ nm, $\tau_0 = 25$ fs, $P_0 = 1.02$ kW): as the soliton redshifts it traps and blueshifts the DW. (b) Spectrograms at 0, 0.5 and 1 m for the soliton and DW, the soliton alone and the DW alone, respectively. The dotted lines show the GV. The used PCF has hole-to-pitch ratio $d/\Lambda = 0.52$ and pitch $\Lambda = 3.6$ $\mu m$, which gives a ZDW of 1054 nm.

by investigating the process in the inertial frame of the soliton. The soliton deceleration is normally provided by the Raman redshift, but can likewise be achieved by tapering the fiber [127].

## 2.4 Supercontinuum generation

*Supercontinuum generation* occurs when short and intense pulses experience extremely large spectral broadening due to a range of interconnected linear and nonlinear effects. It is perhaps the most striking and dramatic effect in nonlinear fibre optics, and is particularly efficient in PCFs due to the excellent control of both nonlinear and dispersive properties. It was first observed in the 1970s in bulk by Alfano and Shapiro [3, 4] and later in optical fibres by Lin *et al.* [5, 6]. In these first experiments the pump fell in the normal dispersion regime and the spectral broadening was mainly caused by the Raman effect and SPM. However, in the 1980s SC generation was realised from a pump in the anomalous dispersion regime, where MI

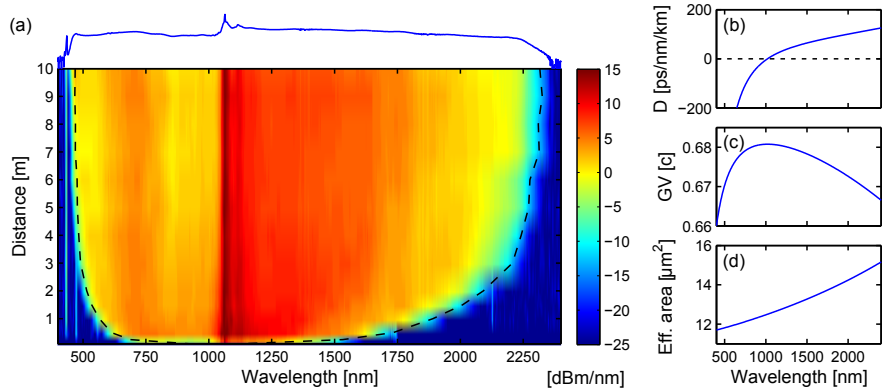


**Figure 2.5:** (a) Experimental cutback measurement of SC generation in a uniform PCF with hole-to-pitch ratio $d/\Lambda = 0.85$ and pitch $\Lambda = 4.4$ $\mu$m. (b)–(d) Calculated dispersion, GV and effective area, respectively. The fibre was pumped at 1064 nm with 10 ps pulses at 15 W average power and 80 MHz repetition rate. The dotted lines in (a) show the measured long-wavelength edge and the theoretically calculated GV matched blue edge.

caused a break-up of the pump into a distributed spectrum of redshifting solitons [19, 35, 128]. The resulting broad spectra were attributed to the an ensemble average of the solitons that had redshifted by different amounts. The SC field really took off with the invention of the PCF, which greatly simplified the requirements needed for SC generation, as demonstrated in the 2000 experiment by Ranka *et al.* [12]. The first commercial SC source saw the light of day shortly after in 2003. Today the technology has matured and SC sources are available from several companies [129].

The commercially available SC sources are typically based on a picosecond high-power fibre laser and a length of PCF to broaden the spectrum. Here we shall focus on such sources. The spectral broadening as a function of length is shown in Fig. 2.5(a) for a laser and PCF typical of most high-power sources. The measurement was made by repeatedly shortening the fibre and measuring the spectrum. The spectrum broadens very rapidly over the first ∼2 m, but the broadening slows down in the remaining fibre length and effectively ceases after ∼8 m. The final SC spectrum is very smooth and extends over 2.5 optical octaves from 450–2300 nm. The calculated dispersion, GV and effective area are shown in Fig. 2.5(b)–(d). The SC broadening in this regime with a picosecond pump in the anomalous dispersion regime close the to ZDW can be described as follows:

(i) The broadening is initiated when MI breaks the picosecond pump into

large a number of temporally short pulses that reshape into fundamental solitons [17–23].

(ii) The solitons generate DWs in the normal dispersion regime and start redshifting. As the solitons redshift they trap and blueshift DWs across the ZDW [35–37, 124, 125].

(iii) The broadening stops when the largest solitons reach the infrared material loss edge, which effectively prevents soliton propagation beyond $\sim$2.4 $\mu$m. This in turn defines the short-wavelength blue edge through GV matching, since this edge is comprised of the most blueshifted DWs that are linked to the most redshifted solitons at the long-wavelength red edge [35, 38].

The fundamental importance of the soliton-induced trapping can be seen in Fig. 2.5(a), where the dotted lines mark the experimentally determined red edge and theoretically calculated GV matched blue edge, respectively. The agreement is excellent and can be used to theoretically determine the blue edge [35, 38, 40], as we shall see. The broadening described above becomes much clearer when investigating the dynamics in spectrograms. To this end, simulated spectrograms of parameters similar to those of Fig. 2.5 are shown in Fig. 2.6 at select propagation distances. The initial stage of MI and the subsequent generation of ultrashort soliton-like pulses are clearly evident in Figs. 2.6(a)–(b), which is further supported by the close-up of the temporal dynamics near the pulse centre shown in Fig. 2.6(d). The final stage of soliton redshift and DW-trapping is apparent in Fig. 2.6(c), where a clear temporal overlap between the most redshifted solitons and the most blueshifted DWs is observed.

The break-up of a long pulse has later been linked to Akhmediev breather theory [13, 25]. Akhmediev breathers are exact analytical solutions to the NLSE that describe the evolution of a wave with a small time-periodic perturbation imposed on a constant background, resulting in the growth and return of a train of ultrashort pulses. It was suggested in [13] that the onset of long-pulse SC generation from spontaneous MI can be interpreted as the generation of large number of Akhmediev breathers that then reshape into solitons.

The distributed spectrum of MI-generated solitons will redshift at different velocities, which inevitable leads to temporal collisions. In fact, it turns out that inelastic soliton collisions are a key driver in the formation of the long-wavelength SC edge [128, 130, 131]. Left isolated, even the most powerful MI-generated soliton broadens and slows down before reaching the loss edge. During such collisions, inter-pulse Raman scattering transfers energy between the solitons; the energy transfer depends strongly on the relative

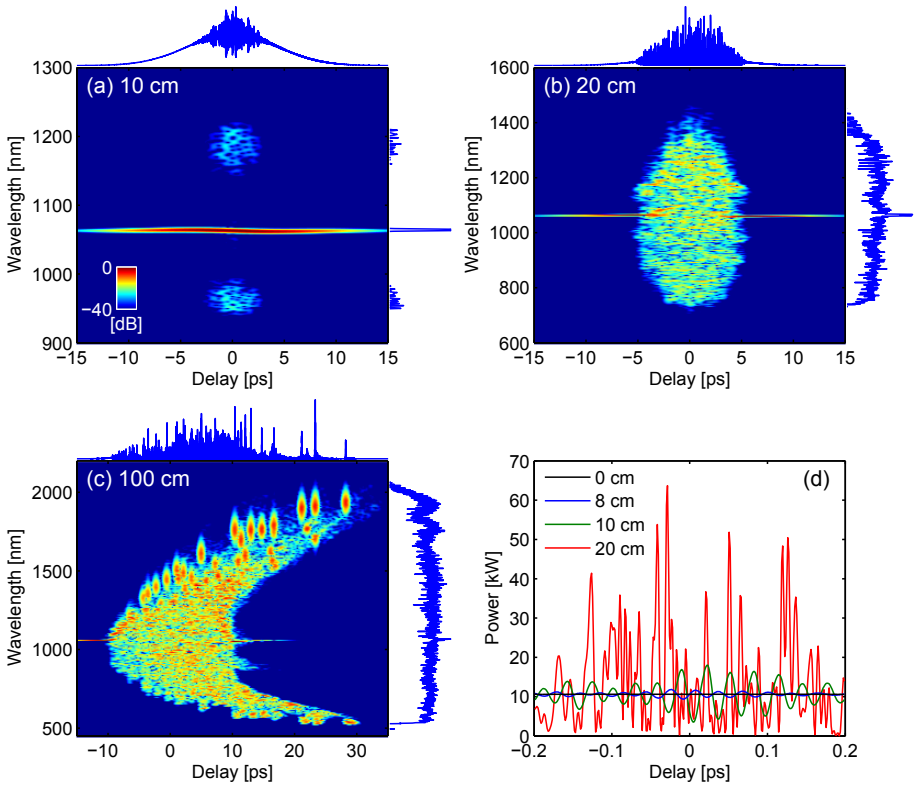


**Figure 2.6:** (a)–(c) Spectrograms at propagation distances of 10, 20 and 100 cm, respectively, calculated for parameters corresponding to those in Fig. 2.5. The spectra are downsampled to 1 nm resolution. (d) Close-up of the temporal evolution near the pulse centre at propagation distances of 0, 8, 10 and 20 cm, respectively.

phase and amplitude, but on average there is a preferential transfer of energy from the smaller to the larger soliton [128, 130, 131]. This energy transfer can lead to the formation of rare large amplitude solitons, also known as *rogue waves* [27], which we discuss in Chapter 4.

It is interesting to compare the *single-shot* spectra in Fig. 2.6 with the measured *averaged* spectra in Fig. 2.5: the MI process generates solitons with a spread in shape and power, which leads to a corresponding difference in the final spectra from shot to shot. This is characteristic of noise-seeded MI and explains why the experimental spectra measured over 1000s of shots are so remarkably smooth and flat. However, there is an intrinsic trade-off between the spectral flatness and noise.

Finally, it should be noted that the spectral broadening can be achieved

through other mechanisms. The dominating broadening mechanisms depend on the dispersion, nonlinearity and pump duration and power. In particular, soliton fission generally takes precedence over MI for short (femtosecond) pulses and soliton-driven broadening is prohibited when pumping in the normal dispersion regime [1].

Chapter 3

# Blue-enhanced supercontinuum generation in tapered PCFs

Amongst the greatest advantages of SC generation in PCFs is the possibility to shape the SC spectrum through dispersion engineering. Indeed, by controlling the dispersion, and thereby the phase and GV landscape, the nonlinear processes that govern SC generation can be manipulated. In this chapter, tapered PCFs are utilised to extend the SC spectrum into the deep-blue. This is motivated by a great commercial interest in extending the bandwidth below 400 nm, in particular for biological applications in e.g. fluorescence microscopy due to the absorption bands of many fluorophores in this wavelength region [70]. The chapter summarises the results of Papers I-IV. Specifically, the importance of the taper shape on available power in the blue edge and the first single-mode high air-fill fraction PCF for deep-blue SC generation.

## 3.1 Tapered PCFs for blue-extended supercontinuum

In soliton-driven SC generation, dispersion engineering can be directly applied to yield a certain SC bandwidth, since the spectral edges are linked by GV matching [35, 38, 39]. The maximal attainable SC bandwidth in a given fibre is thus limited by the GV profile and where the soliton redshift ceases: the maximum extent of the soliton redshift defines the red edge, which in turn defines the blue edge by GV matching. Specifically, in Paper II we define the red edge $\lambda_{\mathrm{red}}$ for a high-power SC source as the wavelength where the spectral broadening is stopped by the increasing material loss

$\lambda_{\text{loss}}$ (the loss "edge"), here set to 2300 nm, or a wavelength $\lambda_2$ close to the second ZDW, whichever is the lowest. Solitons always halt their redshift about 50-100 nm away from the second ZDW [34, 132] so $\lambda_2$ is chosen to $\lambda_{\text{ZDW},2} - 50$ nm, which means that $\lambda_{\text{red}} = \min\{\lambda_{\text{loss}}, \lambda_{\text{ZDW},2} - 50\text{nm}\}$. The blue edge is then simply determined through GV matching. This is demonstrated in Fig. 3.1 by showing the calculated dispersion, effective area and GV for PCFs with a hole-to-pitch ratio of 0.52 and values of the pitch in the range 4.0 to 2.0 $\mu$m. Reducing the pitch shifts the first ZDW to gradually shorter wavelengths and eventually also brings the second ZDW below the loss edge. The effective area reduces with the pitch due to the decreasing core size. But more importantly, the GV decreases with the pitch, which means that there is GV matching to gradually shorter wavelengths up to a certain point. This allows us to define an *optimum pitch* that yields the shortest possible blue edge (for a fixed hole-to-pitch ratio). Reducing the pitch below the optimum increases the GV near the loss edge due to the second ZDW, which increases the GV matched blue edge wavelength. However, simply starting out with a PCF with the optimum pitch is generally undesirable: a pulse break-up with an efficient transfer of energy into the normal dispersion regime requires a pump in the vicinity of the ZDW, and the optimum pitch generally shifts the ZDW far below the ytterbium pump wavelength of 1064 nm used in most commercial SC sources. It further gives a small core that complicates coupling. The trade-off between a short wavelength blue edge and an efficient conversion across the ZDW can be resolved by using tapered PCFs, in which an initial length of uniform fibre with a suitable ZDW ensures an efficient pulse break-up, and a subsequent tapered section with decreasing pitch (and fixed hole-to-pitch ratio) permits GV matching to gradually shorter wavelengths [39, 40, 66–68, 70, 133–137]. For the particular PCF in Fig. 3.1 (that we shall be using later) the blue edge is shifted from 496 nm at a pitch of 3.3 $\mu$m (ZDW at 1035 nm) to 476 nm at the optimum pitch of 2.5 $\mu$m (ZDW at 963 nm). We emphasise that the trends described here are applicable over a wide range of hole-to-pitch ratios.

Tapering has previously been demonstrated as an effective way of extending the SC bandwidth into the blue by changing the dispersion and increasing the nonlinearity [40, 66–68, 70, 133, 136, 138–143]. In particular, spectra extending down to wavelengths as short as 320 nm from a 1065 nm pump were reported in [67,68], which is at the limit of what can be achieved, as we shall see. An impressive 280 nm was reached in [69] by pumping an ultrashort taper with a femtosecond pump at 800 nm. However, in the latter case the light was generated directly in the UV region by a different mechanisms of soliton fission directly from the pump. Table 3.1 summarises

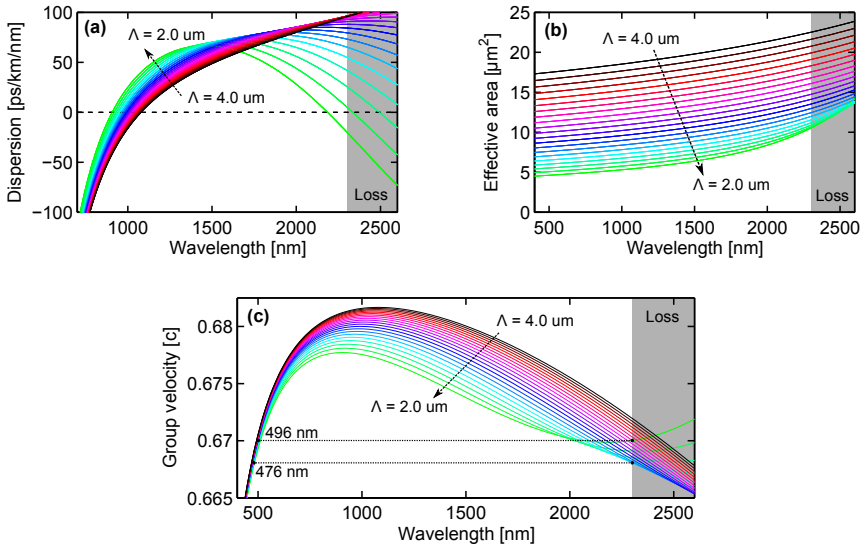


**Figure 3.1:** Calculated (a) dispersion, (b) effective area and (c) GV for PCFs with hole-to-pitch ratio 0.52 and values of the pitch from 4.0 to 2.0 $\mu$m. The shaded areas mark the loss region above 2300 nm, and the horizontal dotted lines in (c) show the GV matching from 2300 nm for a pitch of 3.3 and 2.5 $\mu$m, respectively.

a selective review of the literature on SC generation in tapered fibres, and a more general overview of blue-extended SC generation can be found in the 2010 review by Travers [40].

The use of tapered fibres was first suggested as a means of compensating temporal pulse broadening in lossy fibres [108, 153–156], where the propagation of a soliton can be made invariant by decreasing the dispersion along the fibre. Later the same method was used for pulse compression [157–162] and the generation of high repetition rate soliton trains [22, 23, 156]. Similarly, tapered PCFs have been used for more general soliton manipulation [163–166], including the observation of a soliton blue-shift [167]. And more straightforwardly, tapering has been used to increase the fibre nonlinearity [145, 168, 169]. Indeed, tapered single-mode fibres can be made to have dispersion and nonlinear properties similar to those of a PCF to facilitate SC generation [138, 144, 170]. This has further been utilised for mid-IR SC generation in soft glasses like chalcogenide and tellurite, where the taper increases the nonlinerity and hence expands the SC to longer wavelengths beyond the transmission window of silica [171–174].

PCFs can be tapered exactly like single-mode fibres either by post-

| Reference | Pump[1] | Fibre | SC width and power |
|---|---|---|---|
| Birks, OL 2000 [138] | Ti:Saph, 850 nm, 70-100 fs, 76 MHz | SMF taper 1 m | 370–1545 nm, 300 mW |
| Wadsworth, JOSA B 2002 [144] | Ti:Saph, mode-locked, 850 nm, <200 fs, 76 MHz | SMF-28 taper | 400–1600 nm, 350 mW |
| Leon-Saval, OpEx 2004 [139] | Microchip, 532 nm, 0.6 ns, 6.33 kHz, 1 kW | Tapered PCF, 9 cm, 500 nm core | <400–850 nm, 1.7 mW |
| Foster, OpEx 2004 [145] | Ti:Saph, 25 fs, 80 MHz | PCF taper, sub-um core | 400–1000 nm |
| Teipel, OpEx 2005 [146] | (a) Nd:YVO4, 1064 nm, 8 ps, 85 MHz, 350 nJ , 30 W<br>(b) Nd:YVO4, 1064 nm, 9 ps, 120 MHz, 50 nJ, 6 W | SMF-28, multiple tapers | (a) 450–1600 nm, 4.2 W<br>(b) 900–1600 nm, 1.4 W |
| Lu, OL 2005[2] [140] | Ti:Saph, 880-900 nm, 100 fs, 150 mW | PCF taper, short | ∼380–1200+ nm |
| Travers, OL 2005 [147] | Yb, mode-locked, 1064nm, 3-4 ps, 51 MHz, 8 W (2.2 W) | Cascaded PCFs | 350–1750+ nm, 0.95 W |
| Kudlinski, OpEx 2006[3] [66] | (a) Nd:YAG microchip, Q-switched, 1064 nm, 600 ps, 7.25 kHz, 15kW (60% coupling)<br>(b) Yb, mode-locked, 1064 nm, 3-4 ps, 51 MHz, 60 kW peak, 8 W avg. (4-5 W) | PCF tapers, draw tower | (a) 370–1750+ nm<br>(b) 375–1750+ nm, 3.5 W |
| Xiong, OpEx 2006 [148] | Nd:YAG, microchip, Q-switched, 1064 nm, 0.6 ns, 7.2 kHz, 15 kW | Inflated PCF: all normal ESM → taper (12 cm waist) → ESM | ∼400–1700+ nm, 30 mW |
| Travers, CLEO 2007[4] [67] | Same as [66] | PCF tapers, draw tower | (a) 320–? nm<br>(b) 330–2400 nm, 3.5 W |
| Kudlinski, OL 2008[5] [133] | Yb, CW, 1064 nm, 0.5 nm FWHM, 20 W (13.5 W) | PCF taper, 100 m. Germanium and flurine doped core | 670–1350 nm, 9.55 W |
| Cascante-Vindas, OC 2008 [149] | Nd:YAG, 532 nm, 7 ns, 10 kHz, 282 W (70% coupling) | PCF cobweb taper, 10 cm | 350–800 nm |
| Moselund, Thesis 2009[6] [136] | Yb, mode-locked, 1064 nm, 14.6 ps, 80 MHz, 14 W (70% coupling) | PCF tapers, cm length | ∼380–1750+ nm |
| Kudlinski, JLT 2009 [39]; Mussot, EL 2009 [135] | Yb, CW, 1070 nm, 1 nm FWH , 50 W (35 W) | Tapered PCF, draw tower, 100 m | 650–1380 nm, 19.5 W |
| Kudlinski, OL 2009 [52] | Same as [39], 45 W coupled | Tapered $GeO_2$-doped-core PCF, 130 m (135 to 85 $\mu$m OD) | 470–1750+ nm, 9.3 W |
| Stark, JOSA B 2010 [150] | NOPA 490-700 nm, sub-50 fs, 250 kHz, 250 nJ | Short PCF taper, ZDWs at 509 and 640 nm | ∼350–900 nm |
| Cascante-Vindas, OpEx 2010 [143] | Nd:YAG, 1064 nm, 0.6 ns, 20 kHz, 160 mW/13 kW | PCF taper, 35 cm, Ge doped | 420–1850 nm |
| Kudlinski, OpEx 2010[7] [70, 137] | Nd:YAG, q-switched, 1064 nm, 0.6 ns, 7 kHz, 8 kW (5.8 kW, ∼43 mW avg.) | Tapered PCF, draw tower, 7 m | 350–1750+ nm, 17 mW |
| Peiguang, OpEng 2011[8] [151] | Nd:$YVO_4$, 1064 nm, 7.76 ps, 76 MHz, 10 W | Tapered PCF, 145 m | 430–2050 nm, 1.1 W |
| Stark[9], OL 2012 [69] | 800 nm, 130 fs, 2 nJ | PCF tapers, 5-30 mm | 280–1600 nm |
| Wadsworth, OPN 2012[10] [81] | Yb, pulsed, 1064 nm | PCF taper, draw tower | 310–2500 nm |
| Stone, OFT 2012 [68] | 1060 nm, 5 ps, 1 MHz | PCF taper, 5 m | 330–2600 nm, 130 mW |
| Chen, COL 2012[11] [152] | Microchip, 1064 nm, 0.7 ns, 7 kHz, 8 kW/40 mW coupled | Multiple short PCF tapers | 470–1670 nm |

**Comments:** [1]Coupled power levels are specified in brackets. [2]Blue edge generated as a-Stokes radiation. [3](b) 3 dB flatness: 395-850 nm with 2 mW/nm. [4]Results similar to [66]. [5]A strong peak at 550 nm from a higher-order mode was observed. [6]Taper shape and noise properties investigated. [7] [70] High conversion to 350–600 nm region; [137] similar results, focus on noise reduction in blue edge. [8]Very large OH loss: 188 dB/km at 1380 nm. [9]UV light generated directly from the temporally compressed pump in ultra-steep taper. [10]Values estimated from spectrum in OPN News article. [11]Focus on spectral flatness.

**Table 3.1:** Selective literature overview on blue-extended supercontinuum generation in tapered fibres.

fabrication processes or during the fibre draw, and it has been demonstrated that even very short PCF tapers do not introduce coupling between modes [175]. In addition to decreasing the overall fibre diameter, PCFs allow for a longitudinal variation of the hole-size, which we utilise in Sec. 3.3. Post-processed tapers are fabricated by heating and stretching the fibre, thereby reducing the diameter. This can be done with high accuracy and hole-collapse can be avoided either by pressurising the air holes or tapering cold and fast [136, 149, 176–181]. Post-fabricated tapers are typically limited to 10s of cm, and although longer lengths have been fabricated, such fibres will be very fragile. This is circumvented by tapering directly at the draw-tower by varying the draw-speed during fabrication [40,66,70,133,151,160]. It has generally been the belief [179] that draw-tower tapers shorter than 10 m are difficult to fabricate. On the contrary, we find that tapering directly on the draw-tower offers high accuracy of the fibre parameters by pressure control of the air hole structure, and allows fabrication of accurate fibre tapers with lengths from less than a metre and up with high reproducibility, as shown in Paper III. This further makes it possible to use the draw-tower's coating system as an integrated part of the taper fabrication. A very short draw-tower taper of only 10 cm was recently reported in [182], showing the flexibility of draw-tower tapers.

Blue-extended SC generation has also been achieved by other kinds of dispersion engineering, such as immersing a post-processed tapered PCF in a liquid with a suitable refractive index [183] and by doping the silica glass with e.g. germanium [52, 184, 185]. Changing the material can have the additional advantage of enhancing the Kerr and Raman responses. Impressive results have been demonstrated by (mainly) SPM broadening in short lengths of fluoride fibres with an SC spanning 3 octaves from 350 nm to 3.85 $\mu$m [64]. And recently uniform PCFs with microstructured cores [186] were used to achieve GV matching to wavelengths below 400 nm, but at the expense of a very small effective area.

## 3.2 Optimum taper profiles for blue-enhanced supercontinuum

The idea of extending the SC into the deep-blue by changing the GV landscape has been described and demonstrated by several authors [39, 40, 66–68, 70, 133–137], but the importance of the taper shape remained largely unknown [40]. This section describes the importance of the taper profile on the available light in the blue edge. It should be emphasized that the approach pursued here is for long-pulsed MI-initiated SC generation, which is

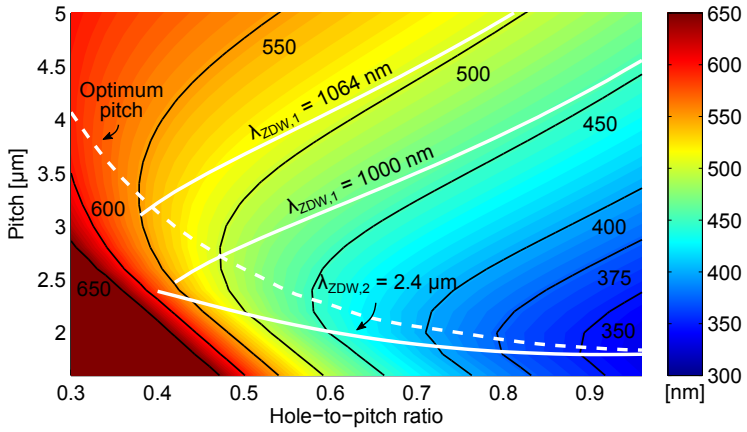


**Figure 3.2:** Calculated blue edge wavelength as a function of hole-to-pitch ratio $d/\Lambda$ and pitch $\Lambda$, assuming GV match to a red edge at 2300 nm or 50 nm below the 2nd ZDW. The dashed line indicates the optimum pitch (shortest blue edge) for a given hole-to-pitch ratio. The full white lines mark where the first ZDW is at 1064 and 1000 nm, respectively, and where the second ZDW is at 2400 nm.

fundamentally different from e.g. [69, 150], where the blue edge is generated directly from a fs pump pulse in an ultrashort taper. The taper profile was optimised for this short-pulse SC regime in [142, 187], where the SC bandwidth and flatness were controlled by manipulating direct soliton fission of the pump in a short tapered fibre.

Analytical descriptions of soliton propagation in non-uniform fibres have been reported by several authors [163, 188, 189]. In particular, Judge *et al.* [163] theoretically calculated the condition for an increased soliton redshift by clever uptapering, where the long-wavelength ZDW is increased as the soliton redshifts so as to avoid DW generation and soliton recoil. However, the focus here is on the downtapering section where the solitons are decelerated and can trap DWs.

As a starting point, in Fig. 3.2 we extend the analysis of Fig. 3.1 by mapping out the calculated blue edge as a function of pitch and hole-to-pitch ratio, which suggests that ∼330 nm can be achieved for $d/\Lambda > 0.95$, and that the optimum pitch is found near 2 $\mu$m for large hole-to-pitch ratios, in agreement with the similar analysis in [40]. This suggests that the results in [67, 68] are at the limit of what can be achieved in terms of achieving the shortest possible wavelength. The figure clearly shows the merits of tapered PCFs for blue extended SC generation: the full white lines mark

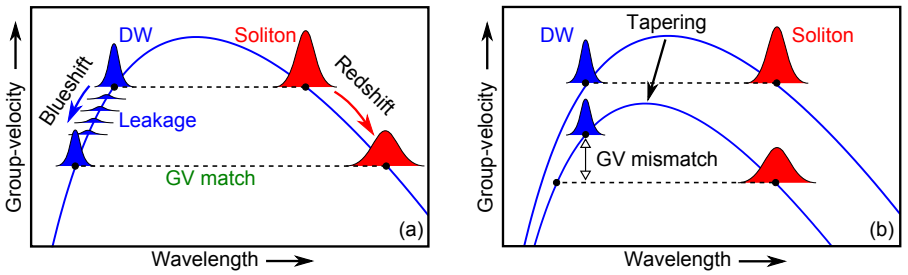


**Figure 3.3:** Radiation trapping and leakage in (a) uniform and (b) tapered fibres. In tapered fibres the asymmetric change in the GV of the soliton and DW gives rise to a group acceleration mismatch.

where the first ZDW is at 1064 nm and 1000 nm, respectively. PCFs with a ZDW of 1000 nm are seen to have GV matching to wavelengths above 450 nm, which demonstrates that achieving GV matching to wavelengths much below 450 nm in a uniform fibre is difficult without compromising the conversion efficiency to the visible due to the offset from the ZDW [38].

### 3.2.1 Group acceleration mismatch

In order to determine the optimum taper profile it is useful to first review the soliton-induced trapping of a DW package in a uniform fibre. It has generally been neglected that the soliton trapping process is in fact not complete, which means that a trapped DW may continuously loose energy. This is illustrated in Fig. 3.3(a): the soliton undergoes a continuous Raman redshift, which leads to a continuous change in GV with propagation length, i.e. a deceleration. The DW does, however, not move spectrally in its own right and is thus not subject to the same deceleration. This means that there is a small difference in GV, and thus potentially a small leakage of DW energy. The Raman effect therefore leads to a *group acceleration mismatch* (GAM); an asymmetric change in the GV of the solitons and DWs. The effect is not significant in uniform fibres, because the relatively weak Raman redshift leads only to small GV changes with propagation and hence a minor GAM. However, in a fibre taper the GV change can be orders of magnitude larger than the inherent Raman induced change. Moreover, the change in GV is generally highly asymmetric, i.e. the taper-induced GV change is much smaller for the DW than for the soliton, as illustrated in Fig. 3.3(b). Travers and Taylor [127] demonstrated that this taper-induced GV decrease enhances the trapping potential of the soliton and can in fact supply the needed soliton deceleration to trap a DW in the absence of the Raman effect.

In physical terms, the GAM lowers the XPM interaction length (the depth of the gravitational well), causing light to escape. To this end, Schreiber *et al.* demonstrated [190] that light can escape or pass unaffected through the XPM interaction region when the interaction length is sufficiently short, i.e. a large GV difference.

The GAM concept was introduced in Paper I, where we further demonstrated, for the first time, the impact of the taper gradient on the trapping of a DW by means of single soliton simulations. This directly translates to a dependence of the available light in the blue edge of an SC on the taper gradient. To investigate the full scale importance of GAM on SC generation comprised by hundreds of solitons and DWs, we fabricated an asymmetric draw-tower taper. The point of the asymmetry is to enforce a difference in the GAM depending on whether the fibre is pumped from the long or short downtapering side, while ensuring that the light passes through the same length of fibre. We based the taper on the commercial fibre SC-5.0-1040 from NKT Photonics A/S with a hole-to-pitch ratio of $d/\Lambda = 0.52$ and pitch 3.3 $\mu$m, which we analysed in Fig. 3.1. We chose this particular fibre, because it it is single-mode at the pump [191].

In all of the SC experiments in this work, we used a modelocked 1064 nm Yb fibre-laser typical for commercial SC sources. The laser emits 10 ps pulses with an average output power of 14 W at a repetition rate of 80 MHz. The PCFs were spliced directly to the laser using a filament splicer, resulting in typical coupling losses below 1 dB. The output was collimated and recorded with an optical spectrum analyser through an integrating sphere. The output power was measured with a power meter and the spectra normalised accordingly (see [192] for details). The IR part of the spectrum was measured with an additional spectrum analyser and the two spectra were stitched together.

The results of the asymmetric draw-tower taper are summarised in Fig. 3.4. We characterise the taper profile in Fig. 3.4(c), where the pitch as a function of length is determined from cross-sectional images. It is seen that the pitch is reduced from 3.3 to 2.5 $\mu$m in an asymmetric way that roughly can be described as a 1.5 m downtaper and a 0.5 m uptaper. The hole-to-pitch ratio of 0.52 was preserved throughout the taper. We used an additional 5 m of uniform fibre before and after the tapered section to generate an initial spectral broadening. The spectra recorded when pumping from the long (blue) and short (red) downtapering sides are shown in Fig. 3.4(a) together with a reference spectrum from a 10 m uniform fibre (black) with a constant pitch of 3.3 $\mu$m. A close up of the blue edge is shown in Fig. 3.4(b), where the theoretically calculated blue edges from Fig. 3.2 are marked; the discrepancy can be ascribed to deviations in the

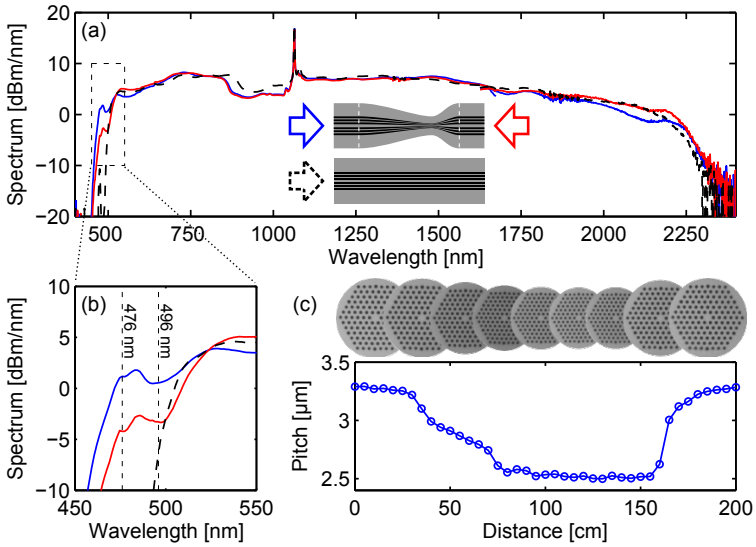


**Figure 3.4:** (a) Experimental output spectra of the asymmetric draw-tower taper. The spectra show the taper pumped from the long (blue) and short (red) downtapering sides. The spectrum of a 10 m uniform fibre (black dash) is shown for comparison. (b) Close-up of the blue edge marked in (a). The vertical lines denote the calculated spectral edges. (c) Measured profile of the taper. The pitch is calculated from the shown cross-sectional images recorded with an optical microscope at 100x magnification. The hole-to-pitch ratio $d/\Lambda = 0.52$ was constant through the taper.

hole-to-pitch ratio in the taper. Evidently, both spectra generated in the tapered fibre extend below the bandwidth achievable in the uniform fibre, as expected. But more importantly, pumping from the long downtapering side clearly yields a significantly higher power in the blue edge than pumping from the short, which confirms the importance of GAM: when the taper is too steep, the solitons at the red edge undergo a much larger deceleration than the DWs at the blue edge, and a fraction of the energy in the DWs therefore escapes the trapping potential and is consequently not blueshifted. In the present case, we see a threefold increase in the energy below 500 nm when the taper is pumped from the long downtapering side. These results form the basis of Paper II. The importance of GAM was complimented with additional experiments and simulations in Paper III.

### 3.2.2 Deep-blue supercontinuum generation

The GV matching landscape in Fig. 3.2 tells us, for a fixed hole-to-pitch ratio, what values of the pitch we should choose to (1) ensure an effective pulse break-up near the ZDW and (2) give the optimum short wavelength blue edge. The notion of GAM additionally says that the length of the downtapering section should be as long as possible to yield an efficient conversion of light to short wavelengths. However, in reality attenuation and soliton broadening will enforce an upper limit on the downtapering length. Specifically, the rapidly increasing loss at short wavelengths will eventually precede the amount of light that is continuously transferred to the edge, and for long tapers the solitons will temporally broaden and/or be stopped by the IR loss edge, and hence terminate the DW trapping and blueshift, before the optimum pitch is reached. For the tapers considered above and in Papers II-III, where the SC never extended below 450 nm, we saw a continual increase in power at the blue edge with increasing taper length. We later conducted additional experiments with downtaper lengths above 10 m, which further supported this conclusion. An SC extending down to 450 nm can, however, be realised in a uniform fibre, as suggested by Fig. 3.2. We therefore - among other things - turned to designing an SC extending below 400 nm. Although far from the 320 nm reported in the literature [67, 68] this is still a significant improvement over most commercially available high-power systems and an important intermediate step on the way to realising a system extending far into the deep-blue. To this end, we fabricated a number of tapers with a hole-to-pitch ratio of 0.7, all with a total length of 10 m. They consisted of ∼35 cm of uniform fibre with a pitch of 4.0 $\mu$m (ZDW at 1035 nm), followed by a downtapering section where the pitch is linearly reduced to either 2.2 or 1.85 $\mu$m over a varying length, and finally a length of uniform waist to fixate the total fibre length at 10 m. A pitch of 2.2 $\mu$m corresponds to the optimum tapering degree defined in Fig. 3.2. The lower pitch of 1.85 $\mu$m was chosen to investigate the influence and sensitivity of the spectrum on the final pitch and the accompanying increased attenuation due to the smaller core. The total length was fixed at 10 m to examine if a long downtapering section is preferable over a relatively shorter downtapering section and a correspondingly longer waist with a fixed pitch.

The results are shown in Fig. 3.5: all spectra show a peak with a high spectral power density around 395 nm and generally have spectral densities above 1 mW/nm across the entire visible spectrum. The exact position of the blue peak varies slightly, which again can be ascribed to slight variations in the actual fibre parameters. The position of the blue edge is particularly sensitive to variations in the hole-to-pitch ratio, and the spectrum of the

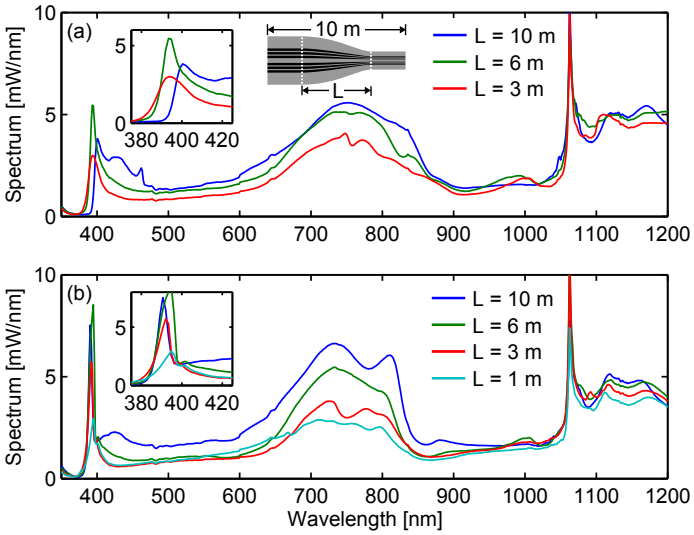


**Figure 3.5:** Experimental spectra of tapered fibres with a hole-to-pitch ratio of 0.7 and varying downtapering length. All fibres had a total length of approximately 10 m, and consisted of a ∼35 cm length of uniform fibre with a pitch of 4.0 $\mu$m, followed by a downtapering section of varying length $L$ (see legend) and a length of waist with a constant pitch of (a) 2.2 $\mu$m (the optimum pitch) or (b) 1.85 $\mu$m.

| Taper length [m] | 10 | 6 | 3 | 1 |
|---|---|---|---|---|
| Vis. power, 2.2 $\mu$m taper [W] | 1.68 | 1.40 | 1.11 | - |
| Vis. power, 1.85 $\mu$m taper [W] | 1.67 | 1.41 | 1.02 | 1.00 |

**Table 3.2:** Visible spectral power below 900 nm of the tapers shown in Fig. 3.5. All spectra had a total power of 5.8 W.

10 m taper in Fig. 3.5(a) suggests that the optimum pitch and hole-to-pitch ratio was not entirely reached in this fibre. More importantly, there is a clear dependence on the downtaper length of the light in the blue edge. In fact, we observe a clear increase of the spectral density in the entire visible part of the spectrum with the length of the downtaper for both values of the final taper pitch. This is detailed in Table 3.2, which gives a list of the visible power below 900 nm measured through two $E0_2$ mirrors. Interestingly, the total power was 5.8 W in all cases, but the visible power has a clear dependence on the downtaper length independently on the final pitch. To understand this difference, we show in Fig. 3.6 the attenuation

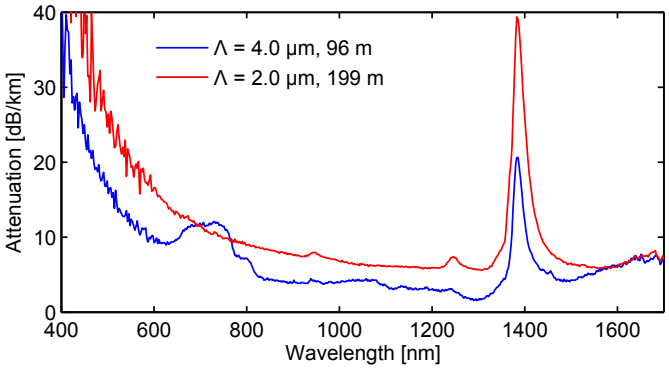


**Figure 3.6:** Attenuation for PCFs with hole-to-pitch ratio 0.7 and pitch 4.0 $\mu$m (blue) and 2.0 $\mu$m (red), respectively. Fibre lengths of 96 and 199 m were used to measure the loss. Courtesy of NKT Photonics A/S.

of two uniform fibres with hole-to-pitch ratio 0.7 and a pitch of 4.0 and 2.0 $\mu$m, respectively. The loss was measured with an incoherent broadband light source in a 96 and 199 m length of fibre, respectively. Because of the low loss and short fibre length the measurement of the 4.0 $\mu$m fibre must be considered relatively uncertain. Similarly, the uncertainty increases at low wavelengths due to a low spectral density of the used light source at these wavelengths. The trend is nonetheless clear: the attenuation increases at all wavelengths with decreasing fibre diameter, in line with [80, 82]. Even so, the loss is still very low at all wavelengths, which explains why we see a constant total power independent on the relative length of the downtaper and waist. The downtapering and waist hence redistribute the energy in the spectrum, but do not introduce any significant additional attenuation in this case. In [82] it was found that although the attenuation increases in small core PCFs, it is rather insignificant for core diameters above 2 $\mu$m, but rapidly increasing for smaller core diameters. The fibres considered here had core diameters in the taper waist of $\Lambda(2 - d/\Lambda) = 2.9$ $\mu$m and 2.4 $\mu$m, respectively, and are thus far from this high attenuation region.

These measurements suggest that a longer downtaper is beneficial in two ways: (1) it shifts more energy all the way to the blue edge due to a lower GAM, and (2) it allows an overall larger transfer of light into the visible. Finally, it is interesting to notice that tapering to 1.85 $\mu$m instead of 2.2 $\mu$m only has a minimal impact on the spectrum: the blue edge appears at the same wavelength, but is enhanced in the 1.85 $\mu$m taper. This could be because the final hole-to-pitch ratio is slightly higher than 0.7, in which

case the optimum pitch is somewhere between 1.85 and 2.2 $\mu$m.

## 3.3 Single-mode air-fill fraction increasing PCFs

While PCF tapers have proven their worth for blue-extended SC generation, accessing the deep-blue spectral region requires a high air-fill fraction. This brings about the drawback that high air-fill fraction PCFs are inevitably (highly) multi-mode at the pump, which greatly complicates coupling and interfacing. To overcome this issue, we fabricated a PCF with longitudinally increasing air-fill fraction *and* decreasing pitch directly at the draw-tower. This uniquely ensures single-mode behaviour at the input and GV matching into the deep-blue at the output, because of the longitudinally increasing air-fill fraction. This can be appreciated from Fig. 3.2: where the previously considered tapers had a constant hole-to-pitch ratio and decreasing pitch, corresponding to moving vertically downwards in the figure, an increasing air-fill fraction and decreasing pitch corresponds to moving diagonally downwards. Specifically, we chose the same input parameters as the tapers in Fig. 3.4 with a 0.52 hole-to-pitch ratio and 3.3 $\mu$m pitch, which makes the PCF single-mode at 1064 nm [191]. However, this time we simultaneously increased the hole-to-pitch ratio to 0.85 and decreased the pitch to 2.0 $\mu$m, which gives a theoretical GV match to 360 nm, according to Fig. 3.2. Importantly, we show in Paper IV that the changes in dispersion and GV in this case follow exactly the same trends as in Fig. 3.1 for a taper with constant hole-to-pitch ratio. The conclusions from tapered fibres with constant hole-to-pitch ratio can therefore be immediately extrapolated to air-fill fraction increasing tapers.

The tapers considered so-far were fabricated by controlling the draw speed during fabrication. However, increasing the air-fill fraction necessitates an additional control of the pressure on the air holes during the draw. Left isolated, we found that increasing the air hole pressure leads to an undesirable increase in the pitch. It was thus necessary to control simultaneously the pressure and draw speed to achieve the desired structure with increasing hole-to-pitch ratio and decreasing pitch. The fibre structure realised after a number of iterative draws is shown in Fig. 3.7: the hole-to-pitch ratio increases from 0.52 to 0.85 over 7 m, while the pitch decreases from 3.3 to 2.15 $\mu$m. The hexagonal structure is well preserved during the air hole-expansion without introducing any structural defects. Although the final pitch is slightly larger than the optimum pitch of 2.0 $\mu$m, this highlights the amazing design freedom in PCFs and clearly verifies the feasibility of fabricating PCFs with longitudinally increasing air-fill fractions. A similar

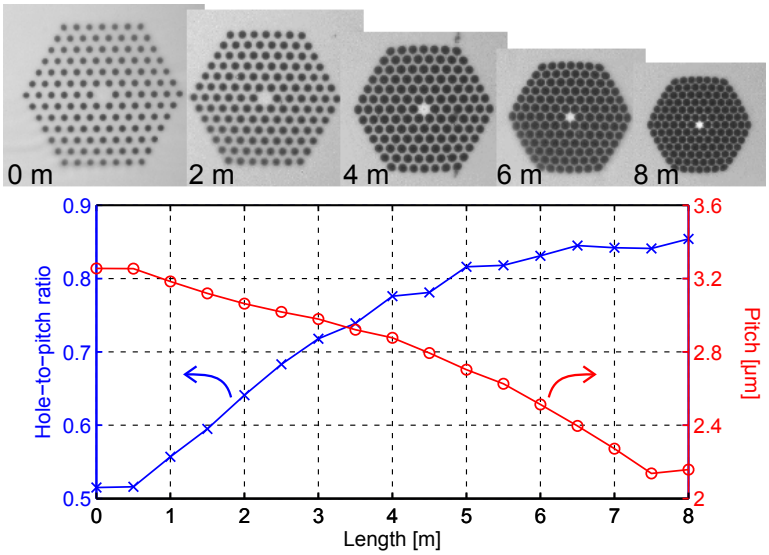


**Figure 3.7:** Characterisation of the fibre structure: the top row shows microscope images of the fibre end facet at selected distances from the input (on the same scale) and the plot shows the corresponding hole-to-pitch ratio and pitch calculated from 17 images equidistantly spaced along the 8 m fibre.

approach was pursued in [148, 193], where the air hole size was increased in a short section of an endlessly single-mode PCF using a post processing technique, but only to enhance the visible power.

Figure 3.8 shows the SC generated in the air-fill fraction increasing PCF, where an initial 40 cm length of uniform fibre was kept to initiate the spectral broadening. The spectrum generated in the fundamental mode had a total power of 5.8 W with 734 mW in the visible part of the spectrum, and extends down to 375 nm with a spectral density above 0.5 mW/nm in most of the visible bandwidth. The discrepancy between the measured spectral blue edge at 375 nm and the theoretical target at 360 nm is due to a perturbation of the innermost air holes, resulting in a reduction of the core size. This is detailed in Paper IV. Yet, these results clearly demonstrate the applicability of air-fill fraction increasing PCFs for single-mode pumped deep-blue SC generation.

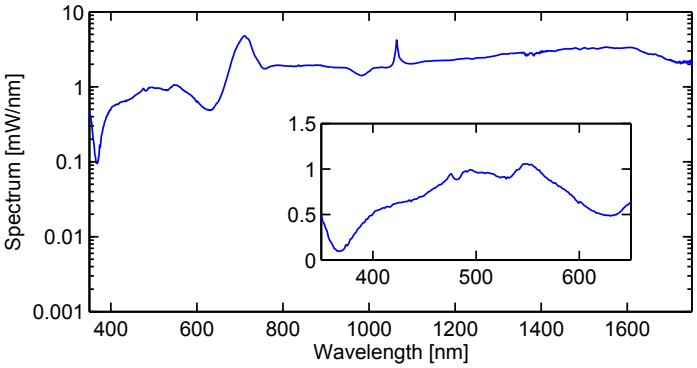


**Figure 3.8:** Measured SC spectrum. The inset shows a close up of the spectral blue edge on a linear scale. The total output power was 5.8 W with 734 mW in the visible part of the spectrum.

## 3.4 Conclusions, discussion and outlook

In this chapter we have investigated the applicability of PCF tapers for blue-extending SC generation into the commercially attractive deep-blue spectral region. Specifically, tapered fibres bring together two otherwise mutually exclusive features: an initial fibre section with a ZDW close to the pump and a subsequent fibre section with GV matching from the mid-infrared loss edge into the deep-blue. The former ensures an efficient break-up of the pump into solitons and DWs, while the latter allows the Raman solitons to trap and blueshift the DWs to short wavelengths.

By introducing the concept of a group acceleration mismatch, we explained that the amount of light transferred to the spectral blue edge is directly correlated with the gradient of the taper. This is because the taper-induced change in GV generally is much larger for the soliton than for its trapped DW package, which can cause light to escape from the soliton-induced trap. We verified this by pumping an asymmetric draw-tower taper from either end, where a longer downtaper significantly enhanced the blueshifted power. Subsequently, we fabricated a range of tapers with a 0.7 hole-to-pitch ratio and successfully demonstrated SC generation with spectral densities in excess of 1 mW/nm across the visible region down to 390 nm. We found that the spectral power in the entire visible region was enhanced by increasing the downtaper length, and that attenuation was not a limiting factor in these tapers. Finally, we fabricated the first single-mode high air-fill fraction PCF for deep-blue SC generation. For this, we

exploited the full degrees of freedom to draw a PCF with longitudinally increasing air-fill fraction and decreasing pitch, which makes it single-mode at the input and resulted in an SC spectrum extending down to 375 nm.

Future directions would include further development of the air-fill increasing PCF to accurately realise the specified target, but also to vary the device length and increase the final air-fill fraction to shift the spectrum below 350 nm. A more thorough investigation of the attenuation must also be conducted to investigate when the increasing material attenuation at short wavelengths becomes a limiting factor for the spectral broadening. It would also be highly interesting to examine the effects of scaling the average and peak power.

It is also yet to be investigated if photodarkening is a limiting factor for SC sources based on tapered fibres. Photodarkening in pure silica has been attributed to the generation of structural defects in the silica network, where partially bound oxygen atoms with one free electron leads to strong absorption [194, 195]. This may become an increasing problem in tapers because of the increased intensity. In terms of reaching ultrashort wavelengths other methods have been pursued, including gas-filled hollow-core fibres [196–198], which resolves any degradation issues since the SC is generated in the injected gas rather than in silica. The combination of very short PCF tapers with sub-wavelength diameters and femtosecond pulses in [69, 150] yielded impressive results with a high energy transfer into the UV region. However, the merits of the method presented here lie in simple and robust all-fibre design that can be made completely compatible with existing technology, and the ability of these designs to work with simpler long-pulsed pump sources with high average powers.

Chapter 4

# Supercontinuum noise properties

The highly nonlinear nature that enables SC generation also makes the process very sensitive to noise; even small noise seeds and pump pulse variations can result in large amplitude variations in the resulting SC [199–203]. A considerable ongoing effort has been devoted to understand and control the SC noise properties, motivated both by application demands for low-noise broadband sources as well as in the fundamental context of clarifying links with instabilities in other systems. The primary sources of SC noise will be discussed in this chapter together with a review of the results of Papers V-VIII. Specifically, we introduce a higher-order moment description of the spectral noise and pursue two approaches to lower the noise: first numerically by actively seeding the pulse break-up with a minute seed and second experimentally by passively controlling the noise with tapered fibres.

## 4.1 Noise sources and rogue waves

There are two main sources of spectral SC noise [201]: the fundamental limit is set by quantum noise, i.e. input shot noise and spontaneous Raman scattering, leading to broadband SC noise. Additionally, the high sensitivity of SC generation to initial input pulse conditions makes the process sensitive to technical noise such as pump fluctuations. The relative importance of these sources depends on the dynamical regime. For most cases - and for long-pulsed SC generation in particular - input shot noise is the dominant noise seed, while Raman scattering plays a minor role [201]. Due to the high stability of modern pump lasers, it is well established that the main source

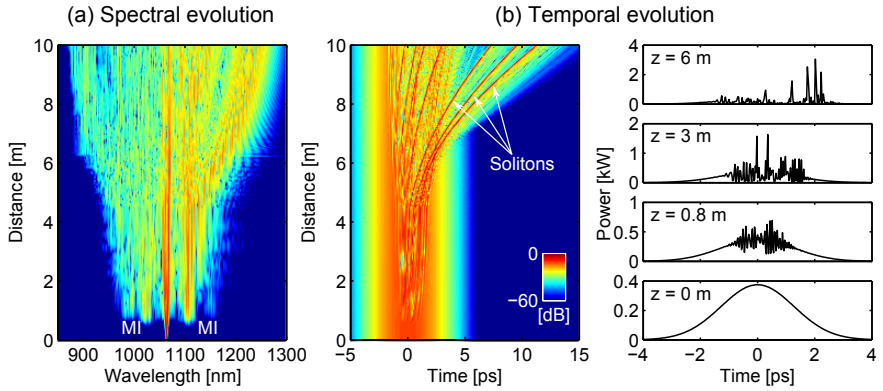


**Figure 4.1:** Spectral and temporal evolution of MI-driven SC generation, using a 3 ps (FWHM) Gaussian pump at 1064 nm with 262.5 W peak power (this odd peak power is chosen to match Fig. 4.3). The PCF has hole-to-pitch ratio 0.52 and pitch 3.6 $\mu$m and is used throughout the chapter.

of shot-to-shot noise in long-pulsed SC generation stems from the noise-driven MI process that breaks the pump into ultrashort pulses [55, 204]. This implies a shot-to-shot variation of the distributed soliton spectrum generated from the MI process, and consequently also of the subsequent soliton interaction and energy transfer. This adds to the noise, because soliton collisions depend strongly on the relative phase and amplitude [128, 130, 131, 205].

The noisy character of SC generation is illustrated in Fig. 4.1 by showing the spectral and temporal evolution of a typical (low-power) SC in the presence of noise. The hallmarks of the noise-initiated MI process are clearly seen in the form of spectral sidebands and a temporal modulation on the pulse envelope, which leads to a break up of the pulse into redshifting solitons. In what follows we shall quantify and discuss the spectral SC noise in more detail.

The long-wavelength edge of a high-power SC is thus constituted of a large number of solitons with a spread in shape and energy that varies from shot-to-shot. In typical experiments, where the SC is measured as an average over 1000s of individually generated spectra, this shot-to-shot information is completely washed-out. This also means that statistically rare rogue waves are not captured by averaged measurement techniques [128]. It was in fact exactly an investigation of spectrally filtered pulse trains of individually generated spectra that allowed Solli *et al.* [27] to observe optical rogue waves in the form of large amplitude solitons that experienced

an enhanced Raman redshift, and hence appeared isolated at the red SC edge. Rogue solitons can either be generated directly as high-peak power solitons in the MI pulse break-up for certain initial noise conditions [27, 206] or through collisional events, where the convective nature of solitons generally transfers energy from the smaller to the larger soliton [29, 205, 207–209]. In that regard, it should be noted that collisional energy transfer between solitons is a necessity for rogue soliton formation in high-power SC generation; the individual MI-generated solitons do not have sufficient energy redshift to the spectral edge.

The rogue wave term is not clearly defined in optics. Following the hydrodynamic definition, rogue waves can be associated with solitons whose height (peak power) is more than twice the significant wave height, i.e. the mean peak power of the one-third largest amplitude solitons [210]. However, the term is commonly used to describe a single high-energy soliton that has experienced an enhanced redshift (relative to the statistical norm), and spectral regions with L-shaped wave energy (histogram) distributions are considered synonymous with rogue waves. In [210] it was further demonstrated that collisional events lead to higher peak powers than any single rogue soliton, suggesting that on-going collisions could in fact also be perceived as rogue events. It should further be noted that rogue waves - like all other waves - are quenched when they reach the loss edge. This has been demonstrated to transform the characteristic L-shaped statistics associated with rogue events into skewed Gaussian statistics [211].

Finally it should be stressed that although long-pulsed SC generation is not suitable for applications that require a high degree of spectral coherence, low pulse-to-pulse energy fluctuations are nonetheless of vital importance (also for incoherent sources) for several applications, such as fluorescence microscopy. In fact, relatively large shot-to-shot variation is not necessarily a disadvantage, since large variations lead to very smooth average spectra [200], which can be utilised for applications where the pulsed SC is treated as quasi-continuous. As an interesting example, the randomness of MI-driven SC generation was utilised to generate random numbers in [212].

## 4.2 Quantifying supercontinuum noise

SC noise is often quantified by the spectral coherence function calculated as an ensemble average over independently generated SC spectra $\tilde{A}_i(\omega)$

[204, 213, 214],

$$\left|g_{12}^{(1)}(\omega)\right| = \left| \frac{\left\langle \tilde{A}_i^*(\omega)\tilde{A}_j(\omega)\right\rangle_{i\neq j}}{\sqrt{\left\langle \left|\tilde{A}_i(\omega)\right|\right\rangle^2 \left\langle \left|\tilde{A}_j(\omega)\right|\right\rangle^2}} \right|, \tag{4.1}$$

where angle brackets denote an ensemble average and the asterisk denotes complex conjugation. The spectral coherence function provides an inside into the stability of an SC and is primarily a measure of the shot-to-shot phase fluctuations, with $|g_{12}^{(1)}| = 1$ signifying perfect coherence. Experimentally, the spectral coherence is related to the fringe visibility of the spectral interference pattern generated by independently generated SC spectra. In contrast, intensity fluctuations are typically quantified in bandwidths of e.g. 10 nm across the SC spectrum, either from histograms of pulse heights (peak powers) [27,207,215] or the *relative intensity noise* (RIN) of the radio-frequency spectrum [201–203, 215]. Specifically, the latter is calculated as $\mathrm{RIN}(\omega) = \Delta\mathrm{P}(\omega)^2/\mathrm{P}_{\mathrm{avg}}(\omega)^2$, where $\Delta P$ and $P_{avg}$ are the mean square intensity fluctuations and average optical power, respectively.

To demonstrate the limitations of the existing noise measures based on histograms, RIN and the spectral coherence, we use numerical simulations in the presence of noise to generate an ensemble of SC spectra under conditions where there are significant fluctuations between different realisations of the ensemble. Throughout this chapter and Papers V-VII, we shall consider a PCF typical for SC generation pumped at 1064 nm. The particular fibre has a pitch of 3.6 $\mu$m and a relative hole-size of 0.52, resulting in a ZDW of 1054 nm (for further details see Paper V or VI). These exact parameters are not special, but chosen because they are realistic and typical of many experiments.

The simulation results for a 3 ps Gaussian pulse with 250 W peak power are shown in Fig. 4.2: the spectral plot in Fig. 4.2(b) superposes results of the 500 individual simulations (grey) together with the calculated mean (solid line), with the top subplots showing the calculated degree of spectral coherence and RIN calculated in 10 nm bandwidths across the spectrum. Figure 4.2(c) shows histograms of the pulse energy fluctuations extracted over the 10 nm bandwidths marked in the spectral plot in Fig. 4.2(b) (Fig. 4.2(a) shows a re-analysis of the results described in the following section). The close-up of the long wavelength edge clearly shows the presence of a few rogue wave-like solitons that have redshifted significantly further than the statistical mean. This is also reflected in the histograms that show a transition from Gaussian near the pump to long-tailed (L-shaped) near

the long wavelength edge. The spectral coherence and histograms clearly provide only limited and qualitative information. For example, whilst it is easy to calculate and display the coherence at all wavelengths across the spectrum, the fact we see that it is zero over most of the SC bandwidth indicates only the presence of severe noise over a wide wavelength range, without indicating anything specific about its nature. On the other hand, displaying histograms at specific wavelengths across the SC is useful to show how statistics can vary from Gaussian near the pump to long-tailed near the long wavelength edge, but the selection of which particular wavelengths to filter and analyse in this way is not a priori evident. The RIN gives a measure of the noise across the full SC bandwidth, and although it captures the increase in noise with detuning from the pump, it does not provide any information on the nature of the shot-to-shot fluctuations.

### 4.2.1 Higher-order moment description of spectral noise

To resolve the limitations of the noise measures discussed above, we introduced *higher-order moments* as SC noise and rogue wave descriptors in Paper V. The HOMs characterise the shape of a particular distribution and not only its location and spread. For a real-valued random variable $X$, the $n$th-order central moment around the mean is given by

$$\mu_n = \langle (X - \langle X \rangle)^n \rangle. \tag{4.2}$$

The zeroth and first central moments are $\mu_0 = 1$ and $\mu_1 = 0$, respectively. The second order central moment $\mu_2$ is the well-known variance $\sigma^2$, which measures the distribution spread. Instead of $\sigma^2$ we shall be using the so-called *coefficient of variation*: $C_v = \sigma/\langle X \rangle$, which has the straightforward interpretation as being inversely proportional to the *signal-to-noise ratio* (SNR) that we shall also consider later. Of particular interest for analysing the asymmetric long-tailed distributions associated with SC generation are the third and fourth central moments, commonly expressed in normalised form relative to the variance. The third order central moment is referred to as the *skewness* $\gamma = \mu_3/\sigma^3$, which measures the asymmetry of the distribution, with $\gamma < 0$ for a left-skewed distribution, $\gamma > 0$ for a right-skewed distribution and $\gamma = 0$ for a symmetric distribution. The fourth-order central moment is referred to as *kurtosis* $\kappa = \mu_4/\sigma^4 - 3$, and measures whether the distribution is peaked or flat relative to a normal distribution of the same variance. A normal (Gaussian) distribution has $\kappa = 0$, and a high kurtosis arises from rare extreme deviations from the mean. The HOMs all relate to the pulse intensity, and should hence be considered complementary to the phase-sensitive spectral coherence, Eq. (4.1).

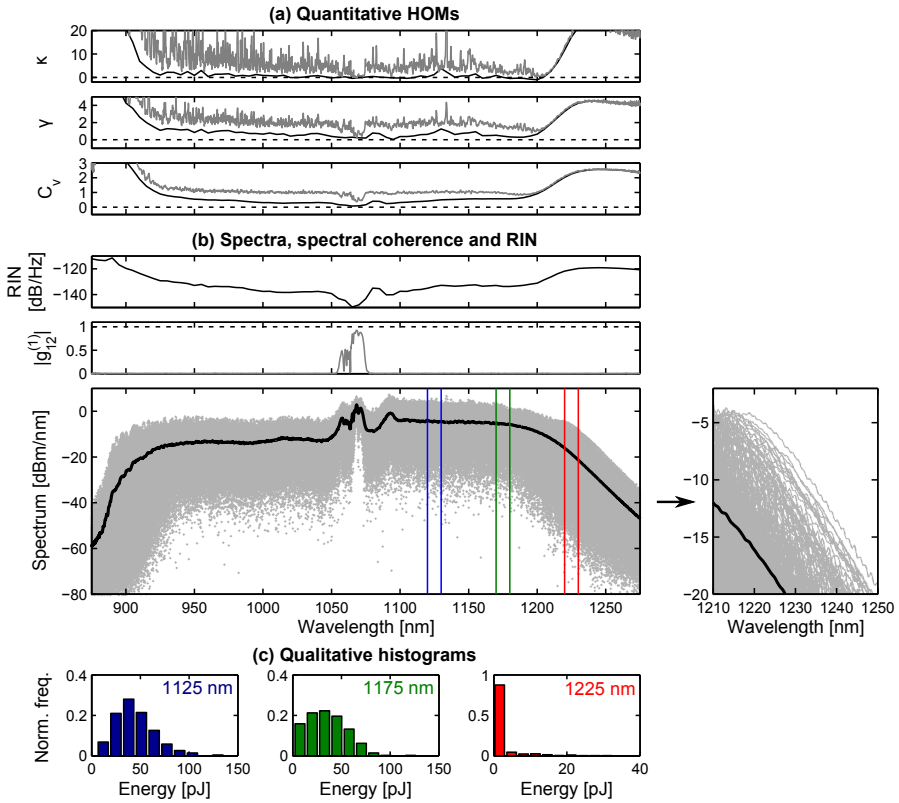


**Figure 4.2:** Numerical simulations in the presence of noise. (b) Spectra, calculated degree of spectral coherence ($|g_{12}^{(1)}|$) and RIN for a 3 ps Gaussian pulse with 250 W peak power after 10 m propagation. A close-up of the long wavelength edge is shown on the right. (a) Corresponding HOMs calculated both in 10 nm bandwidths (black lines) and using the numerical resolution (grey lines). The HOMs are kurtosis ($\kappa$), skewness ($\gamma$) and coefficient of variation ($C_v$), respectively. (c) Histograms calculated in the 10 nm spectral windows marked in spectrum in (b).

We re-analyse the simulation results presented above using HOMs in Fig. 4.2(a). The HOMs are calculated across the SC spectrum both in 10 nm bandwidths and using the numerical resolution (0.07 nm at 1064 nm). The moments clearly reflect the transition from low-noise near-Gaussian statistics to noisy highly skewed and peaked statistics when the window is moved into the spectral wing. A larger spectral window introduces a higher degree of averaging and hence results in lower values of the HOMs, but the particular choice of spectral windows does not affect the overall conclusions. The HOMs thus provide direct insight into the degree and nature of the noise across the SC bandwidth, and allows a direct quantitative comparison between modelling and experiment. In other words, the HOMs capture both the magnitude and character of the noise, which previously had only been analysed with a combination of qualitative histograms and a quantitative measure such as RIN.

In Paper V we detail how the HOMs can be used to gain insight into the nature of the intensity fluctuations in a few select cases. We further suggest, as a useful guideline, that rogue wave behaviour can be associated with the product of skew and kurtosis exceeding ten, $\gamma \cdot \kappa > 10$. This, however, should be taken as a rule of thumb and not a strict criteria. As a further example of the utility of the HOMs, Wetzel *et al.* [216] used a frequency-to-time mapping technique to measure single-shot SC spectra. The analysis of the noise properties based on HOMs showed an excellent agreement with simulation results across the full SC bandwidth.

## 4.3 Seeded supercontinnum generation

In the long-pulse MI-driven regime, it has been demonstrated that modifying the input conditions can stabilise the otherwise highly turbulent and noisy SC generation. Indeed, by inducing the MI with an externally applied modulation, a train of short soliton-like pulses can be generated with a desired repetition rate [17, 18]. It was thus suggested by Islam *et al.* [128] that the distributed spectrum of solitons generated from the MI of a picosecond pulse could be generated deterministically with small shot-to-shot fluctuations by seeding at the MI frequency. Extensive investigations have used modulational control of the input pulse both to clarify the fundamental physics underlying instabilities and links to rogue wave phenomena [206, 217–219], as well as in the application motivated context of lowering the SC noise [220–225].

To illustrate the basic principle of modulational control of the pump in SC generation, we revisit the results of Fig. 4.1 in Fig. 4.3, where the

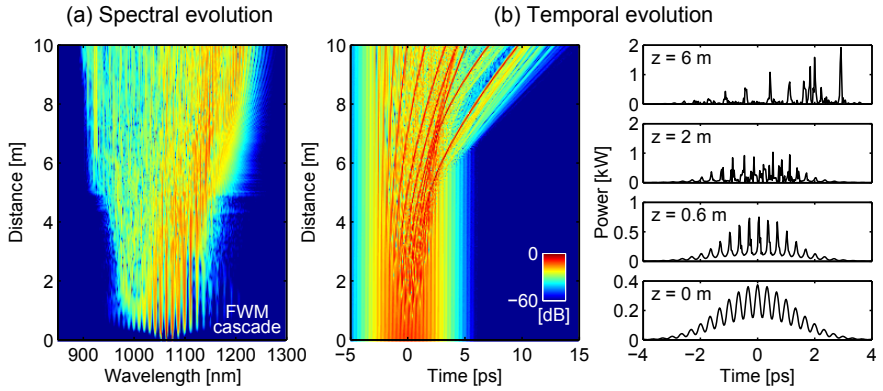


**Figure 4.3:** Spectral and temporal evolution of seeded SC generation, similar to Fig. 4.1, but with the pump power split between a 250 W pump and an identical seed with 5 % of the power and a 3 THz frequency offset relative to the pump.

pump is modulated with a weak seed pulse. This altogether changes the character of the pulse break up: whereas unseeded MI builds from noise that differs from shot to shot, the seed ensures the same beating of the temporal pulse envelope in every shot, and therefore leads to a *deterministic* rather than noise-driven pulse break-up. In the frequency domain the seed leads to the amplification of a FWM cascade rather than an amplification of MI sidebands from noise. The resulting noise reduction is quantified and discussed in the following.

Seeded SC generation was numerically investigated in [221, 222, 225]: Genty *et al.* [221] found that, for a pump with a low peak power of 75 W, an optimum SC broadening and stability was achieved for a seed pulse with a 5 THz offset relative to the pump. Similarly, [225] investigated the influence of a weak CW seed on low power SC generation in a dispersion-shifted fiber, and described how seeding leads to a pulse breakup caused by FWM. A high peak power of 10 kW was used in [222] to generate a coherent comb-like SC in a short PCF by introducing a seed. An optimal fibre length on the order of 5-10 cm was determined, for which the comb remains coherent, yet relatively narrow and highly structured. Experimentally, SC generation was induced by triggering a sub-threshold pump with a seed pulse or CW in [217,223,224]. This further led to improved spectral stability and coherence. This, however, is fundamentally different from the results of [221, 222, 225], where the pulse break-up is caused by the amplification of a FWM cascade. Rather than modulating the pump with a seed pulse, it has been attempted to feed back a fraction of generated SC from one pulse

as a seed for the following pulse [220, 226–233]. Although very interesting, we shall not pursue this approach here.

While it has thus been shown that seeding can reduce the noise of an SC, this has been either at low pump power, often close to the MI threshold, or for very short fibres. The previous investigations are thus far from commercial SC sources with peak powers and fibre lengths on the order of 10 kW and 10 m, respectively. To this end, in Paper VI we investigated seeding under a variety of conditions, and explain what happens as we approach the parameters of a commercial SC source. In particular, we investigate the influence of the seed wavelength and MI gain spectrum on seeding at various power levels above the SC threshold, from which we highlight a number of distinct dynamical regimes. In Paper VII we further demonstrated that seeded SC generation is extremely sensitive to the degree of phase noise of the seed. The main results of Papers VI-VII are reviewed in the following.

### 4.3.1 Influence of seed wavelength and MI gain spectrum

As a starting point, we consider a 3 ps Gaussian pump with 250 W peak power and a seed with the same temporal width but 5% of the peak power, similar to Fig. 4.3. We use the same PCF as in Figs. 4.1–4.3 with a ZDW at 1054.2 nm. The results for pumping close to the ZDW at 1055 nm with varying seed frequency offset are shown in Fig. 4.4; pumping close to the ZDW shifts the MI gain peak far away from the pump and above the Raman gain peak, which yields the richest dynamics and is useful for highlighting the general dynamics. The MI and Raman gain spectra are shown in Fig. 4.4(f). For each set of parameters we carried out 200 simulations to quantify the noise properties with the spectral coherence and SNR.

Figure 4.4(a) shows the evolution of unseeded SC generation (overlapping pump and seed). Unseeded MI amplifies a single set of side-bands that evolves into solitons and DWs, as demonstrated in Fig. 4.1. This results in an incoherent spectrum with near-unity SNR over most of the bandwidth. The white lines mark the width of the MI gain spectrum, defined by where the gain is 5% of the maximum gain. By introducing a seed with a small 3 THz offset relative to the pump, the pulse breakup is initiated by a cascaded FWM process that causes a coherent broadening of the pump, as seen in Fig. 4.4(b) (and Fig. 4.3). The width of the frequency comb is limited by the width of the MI gain spectrum. With further propagation a soliton is generated from the FWM process with enough power to redshift outside the MI gain band. The output spectrum is coherent over most of the bandwidth, but the soliton at the long wavelength edge of the spectrum has a varying phase from shot to shot, which degrades the coherence at the spec-

tral edges, but leads to a high intensity stability. When the seed is shifted further away to the peak of the Raman gain at 13 THz in Fig. 4.4(c), the spectral evolution is dominated by the amplification of a single set of coherent side-bands amplified through degenerate FWM. At ∼5 m a massive soliton is ejected from the long wavelength side-band, which is exactly what was referred to as 'harnessing and control of optical rogue waves' in [206], where the pump pulse was modulated with a well-defined frequency to eject a large amplitude soliton. The soliton is again not phase-stable from shot to shot, but it is highly intensity-stable. This is opposite to what was reported in [225], where the rogue soliton was coherently generated from a FWM side-band. By shifting the seed to the peak of the MI gain at 20 THz in Fig. 4.4(d), a single set of well-separated side-bands is amplified. The pump and side-bands broaden independently of each other, mainly by SPM. This leads to a spectrum with three clearly distinct bands of high coherence and SNR. Finally, in Fig. 4.4(e) the seed is shifted to the tail of the MI gain spectrum, and a single set of side-bands is slowly amplified. The pump is only slightly depleted and experiences noise-seeded MI unaffected by the seed at 1180 nm.

These general trends were confirmed over a larger parameter space in Paper VI. In particular, the best noise improvements were found for $0 < \nu_{\mathrm{mod}} \lesssim \frac{1}{4}\nu_{\mathrm{MI}}$, where $\nu_{\mathrm{mod}}$ and $\nu_{\mathrm{MI}}$ are the pump-seed frequency offset and MI gain bandwidth, respectively. In this regime, the amplification of a broad FWM cascade with many bands across the MI gain bandwidth leads to a spectrum with high coherence and SNR over most of the bandwidth, as in Fig. 4.4(b).

One of the main conclusions of Paper VI is that although it is possible to divide the results into regimes of high and low coherence and intensity stability, depending on the wavelength and power of the pump and seed, the seeding process is highly sensitive to the exact input parameters. Generally, we find that the shot-to-shot stability can be increased by pumping further away from the ZDW. This results in an increase of the MI gain at small frequency offsets, which gives a faster amplification of the FWM cascade that diminishes the influence of noise. This is illustrated in Fig. 4.5, where we show the temporal dynamics for pump wavelengths of 1055 and 1075 nm, respectively. The strong dependence of the MI gain spectrum on pump wavelength is clearly seen in the subfigures on the right. The seed causes a beating of the temporal profile, which, if chosen correctly, leads to a deterministic pulse break-up. When the pump is close to the ZDW as in Fig 4.5(a), the MI gain is relatively small at the seed wavelength (1070.1 nm) and slowly increasing with wavelength. The temporal profile is therefore only slowly broken up into solitons. The solitons are therefore

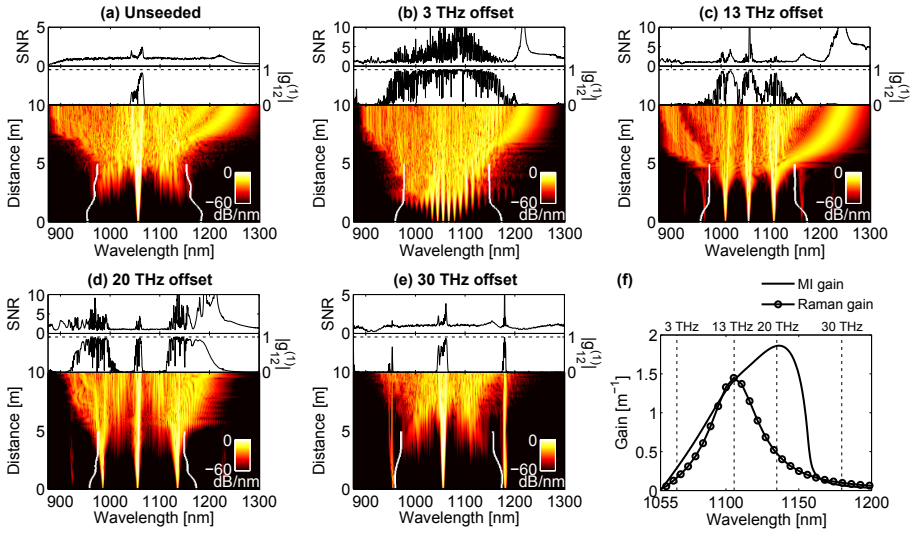


**Figure 4.4:** Single-shot simulations of pumping at 1055 nm with a 250 W pump and a 5% seed at frequency offsets of (a)-(e) 0, 3, 13, 20, and 30 THz, respectively. The white lines indicate the MI gain bandwidth. The top rows in (a)-(e) show the ensemble calculated signal-to-noise ratio (SNR) and spectral coherence ($|g_{12}^{(1)}|$). (f) MI and Raman gain curves, the vertical lines correspond to the frequency offsets used in (a)-(e). The frequency offset of 13 THz (c) is the Raman gain peak and 20 THz (d) is the MI gain peak.

mainly generated from the pulse centre where the peak power is highest. This gives the solitons time to redshift before the cascade is amplified and the dynamics is relatively turbulent. In contrast to this, pumping further from the ZDW gives a much larger gain at the seed wavelength (1090.6 nm) that increases more rapidly with wavelength. This causes a fast breakup of the temporal pulse, where the individual temporal fringes generate fundamental solitons in a controlled fashion that almost resembles soliton fission, as seen in Fig 4.5(b). The most powerful solitons are still generated near the centre of the pulse where the power is highest. The most powerful rogue-like soliton only collides with the smaller solitons generated from the trailing edge of the pulse. Interestingly, a closer inspection reveals that this rogue-like soliton is generated *incoherently* when pumping close to the ZDW, but *coherently* when the pump is shifted away from the ZDW.

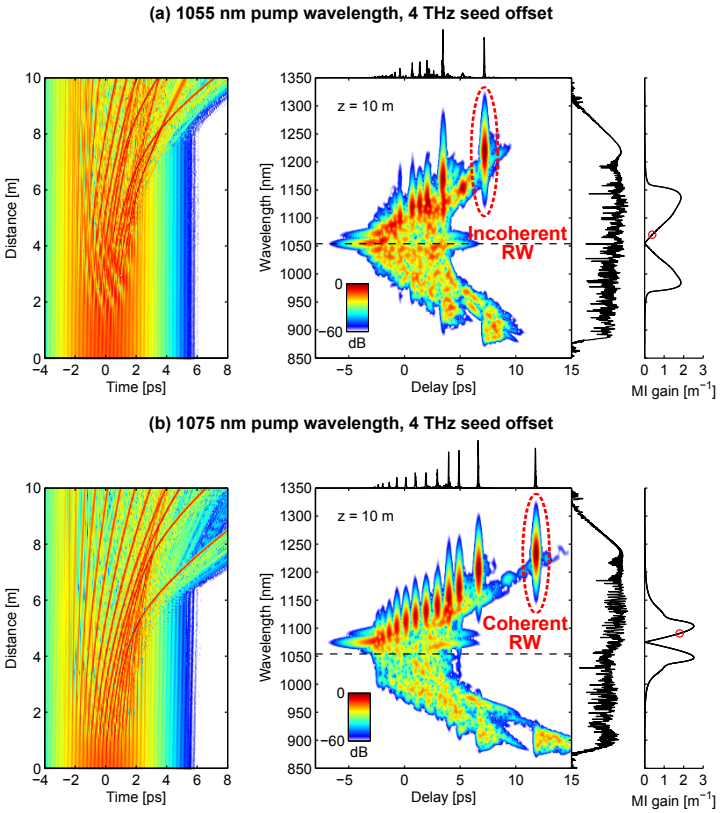


**Figure 4.5:** Temporal evolution, spectrogram at the fiber end (10 m) and MI gain spectrum for a 5% seed with a 4 THz offset for pump wavelengths of (a) 1055 nm and (b) 1075 nm. The black dashed lines in the spectrograms mark the ZDW at 1054 nm and the seed wavelength is marked with red circles in the MI gain spectra.

### 4.3.2 Seeding at high peak power

It thus seems safe to conclude that a suitably chosen seed can be used to effectively manipulate the pulse breakup and improve the noise characteristics. However, the situation changes drastically when we approach the power levels and fibre lengths of typical SC sources. To this end, we show in Fig. 4.6 the spectral evolution and noise statistics (calculated from an ensemble of 100 simulations) for a 1064 nm pump with peak powers of 500, 750, and 1500 W, respectively, and a seed at 3 THz offset. When the peak power of the pump is increased, the SC bandwidth increases and multiple distinct solitons and GV matched DWs become visible. However,

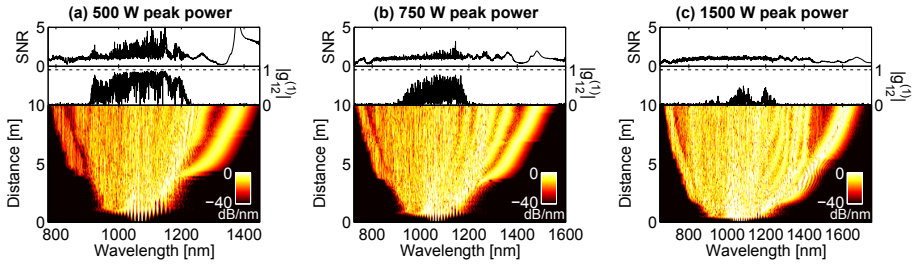


**Figure 4.6:** Single-shot simulations of pumping at 1064 nm with a 5% seed at a frequency offset of 3 THz for pump peak powers of (a)–(c) 500, 750, and 1500 W, respectively. The top rows show the signal-to-noise ratio (SNR) and spectral coherence ($|g_{12}^{(1)}|$).

the increasing pump power also severely degrades the noise properties and only the central part of the spectrum remains (partially) coherent. At the highest peak power of 1500 kW in Fig. 4.6(c), the initial FWM cascade is quickly washed out by the onset of phase-dependent soliton interactions and DW generation, and the output spectrum is incoherent over most of the bandwidth.

Although the pulse breakup can be completely deterministic also at high pump powers, the subsequent turbulent solitonic dynamics makes the resulting spectrum incoherent. In [220] it was experimentally demonstrated that the spectral noise increases with the pump power, although this was for a very different set-up where a fiber with two closely spaced ZDWs was back-seeded. It is interesting to notice that the typical broad and flat SC spectra reported in most high-power experiments come at a price of low coherence; the flatness is exactly a consequence of the averaging over solitons with large shot-to-shot variations in shape and energy. Similarly, the high power seeded SC generation in [222] resulted in highly structured spectra, but only with a sub-octave bandwidth due to the short fibre length.

### 4.3.3 Influence of phase coherence

The SC noise improvements afforded by seeding have all been obtained using a phase coherent seed. In particular, the numerical investigations in [206, 221, 222, 225] and Paper VI all used a perfectly coherent seed to modulate the pump. Experimentally, the seed was generated by filtering a fraction of the pump in [217] and in [223] the signal and idler from an optical parametric amplifier were used as pump and seed, respectively. A

separate CW source was used as the seed in [224]. It thus seems fair to assume that in all these cases the seed was at least partially coherent with the pump. In Paper VII we therefore addressed the influence of the phase coherence of the seed with numerical simulations, to see which conditions this enforces on the mechanisms that can be used to generate the seed.

Figure 4.7 recaps the results of Paper VII of seeding with a partially (in)coherent seed. In addition to the broadband noise of the one-photon per-mode model, phase noise was added to the seed based on a physically justified phase-diffusion model. The model assumes fluctuations of the temporal phase with zero ensemble mean, resulting in a Lorentzian noise spectrum whose width is quantified by the linewidth $\Delta\nu_{\mathrm{FWHM}}$ (see Paper VII and Appendix A for details). The results in Figs. 4.7(a)–(c) show the spectral evolution and ensemble calculated statistics (from 500 simulations) for a 250 W pump at 1064 nm and a seed with 3 THz offset from the pump and varying phase noise linewidth. The phase coherent seed in Fig. 4.7(a) results in a highly coherent spectrum as described in the previous sections. When the linewidth of the seed is increased in Figs. 4.7(b)–(c), the broadening is still initiated by cascaded FWM, but the contrast of the FWM comb decreases, resulting in a significant degradation of the SNR and coherence. This is further detailed in Figs. 4.7(d)–(f) by the ensemble calculated spectra at a propagation distance 1 m for the same linewidths as Figs. 4.7(a)–(c). Although the comb structure is clearly seen in all cases, the fringe contrast is significantly decreased when the noise linewidth is increased, which results in a similar decrease in the spectral coherence and SNR. In Paper VII we confirm these results over a much larger parameter space. In particular, our results clearly show that the maximum tolerable phase noise of the seed is in fact quite small and that the specific phase-noise tolerance decreases with increasing pump power. This directly restricts the mechanisms that can be used to generate the seed.

Finally, it should be emphasized that quantitative validity of these results is limited by the numerical resolution: a numerical resolution of 19.1 GHz was used for Fig. 4.7. This is discussed in Paper VII, where we confirm that although we generally can not *quantitatively* determine the exact allowable phase noise linewidth, our results are *qualitatively* valid: The results clearly show that the SC becomes increasingly noisy when the seed noise linewidth is increased, and that the seed must be at least partially coherent with the pump to achieve a coherent SC.

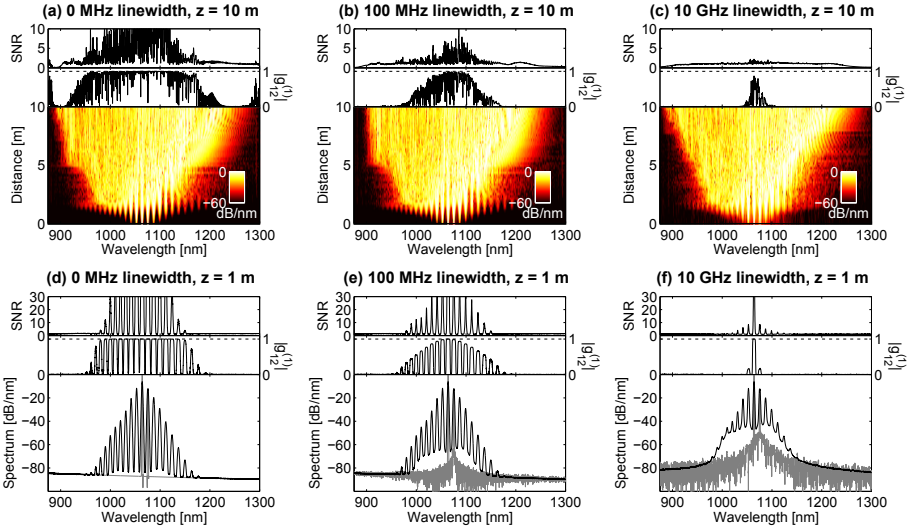


**Figure 4.7:** Single shot simulations of seeded SC generation with varying seed linewidth, $\Delta\nu_{\mathrm{FWHM}}$. (a)–(c) Spectral evolution and ensemble calculated spectral coherence ($|g_{12}^{(1)}|$) and signal-to-noise ratio (SNR) at the fiber output (10 m). (d)–(f) Ensemble calculated spectra and noise properties at a propagation distance of 1 m for the same linewidths as (a)–(c). The grey spectra show single shot input.

## 4.4 Noise properties of blue-extended supercontinuum

So far we considered active noise reduction by seeding the initial stages of the SC formation. In Paper VIII we experimentally investigated passive noise reduction by controlling the subsequent soliton-driven dynamics with tapered fibres. A discussion of this is also included in Paper III. This was first investigated by Moselund [136], who found a clear difference in the noise properties of the SC generated in a uniform and short ∼2 cm tapered PCF. However, the dynamics in such short tapers are very different from longer tapers, in that the taper length is very short compared to the soliton period and the conversion into the visible poor. The noise reduction in [136] can therefore not immediately be extrapolated to longer tapers. Longer tapers were investigated by Kudlinski *et al.* [137], who speculated that the taper increases the power density beyond 1750 nm (because of the increased nonlinearity and decreased dispersion), which translates into an increased number of solitons at these long wavelengths and hence a noise reduction. This, in turn, decreases the noise at the blue edge because of

the GV matched link between the spectral edges. The shot-to-shot noise was quantified in filtered spectral regions across the SC as the variation of the smallest to the largest amplitudes in each recorded pulse train. The SC noise from a uniform and 7 m long tapered PCF were compared using this noise measure, and the tapered fibre was found to reduce the noise across the full SC bandwidth upto 1750 nm.

In Paper VIII we measured the RIN across the full SC bandwidth as a function of power in a uniform and tapered PCF. The RIN measured in filtered wavelength regions by an electric spectrum analyser are shown in Fig. 4.8(a) and the corresponding spectra in 4.8(b) (see Paper VIII for further details). The PCFs had a hole-to-pitch ratio of 0.52 and are thus similar to those in Fig. 3.4, but with a longer 4 m tapered section. The noise properties of the uniform and tapered fibres appear very similar; the RIN increases with the detuning from the pump and exceeds -75 dB/Hz on the blue side of the spectral edge for both the uniform and tapered fibre. The figure does, however, suggest that the noise around 600 nm is slightly lower in the SC generated in the tapered fibre. To investigate the noise on the edge further, Figs. 4.8(c)–(d) show measurements of the red and blue edges, respectively, where the pump power was adjusted to shift the spectral edge (at the -10 dBm/nm level) to a certain wavelength. The figure shows that the RIN follows the edge and is at the same level in both the uniform and tapered fibre. This result opposes the conclusions drawn in [137], although the interpretation is ambiguous: in as much as the noise follows the spectral SC edge, tapering can indeed lower the noise near the blue edge compared to an SC generated in the corresponding untapered fibre, simply because the blue edge is shifted to a shorter wavelength. The noise level near the edge will, however, remain the same according to our results based on RIN. One could therefore claim that tapering does indeed lower the noise in the visible part of the spectrum by moving the spectral blue edge. Notwithstanding, we do not observe a noise reduction across the full SC bandwidth as reported in [137]. These results are described in greater detail in Paper VII, where the RIN is mapped out as a function of peak power and wavelength. The results are complimented with numerical simulations in Paper III.

## 4.5 Conclusions, discussion and outlook

We investigated the noise properties of long-pulsed SC generation. This regime is characterised by large shot-to-shot fluctuations originating from the noise-driven MI process that breaks the pump into solitons and DWs.

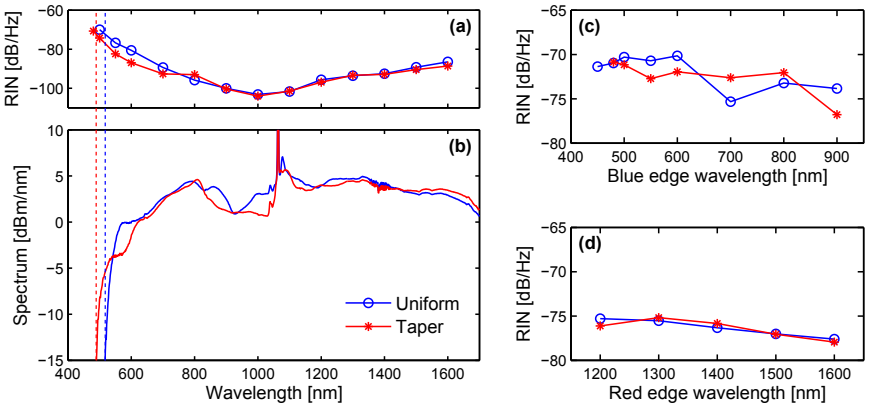


**Figure 4.8:** (a)–(b) Measured spectra and RIN for a uniform fibre (blue) and a taper (red) pumped with a peak power of 5 kW. The PCFs are similar to those of Fig. 3.4, but with a 4 m tapered section. (c)–(d) Noise at the spectral red and blue edge as a function of wavelength. The spectral edges were controlled by adjusting the pump power.

The subsequent turbulent solitonic dynamics adds to the noise and leads to the formation of statistically rare optical rogue waves. Previously, SC noise has been quantified by the phase-sensitive spectral coherence function and histograms of spectrally filtered pulse energies, which only gives limited and qualitative information about the noise without revealing anything about its nature. Here we introduced statistical higher-order moments that collectively give an accurate quantitative measure of the spectral noise across the full SC bandwidth, and provide a clear identification of regions of rogue wave behaviour.

Moreover, we attempted two approaches to lower the large spectral noise. First we numerically investigated noise reduction by seeding the pulse break-up, where a suitably chosen seed can deterministically break up the pump by the amplification of a FWM cascade rather than by noise-seeded MI. Although this method appears very promising at first glance, our results showed a high sensitivity to the exact parameters of the pump and seed. In particular, we found that turbulent soliton dynamics overpowers the deterministic pulse break-up for commercially relevant kW pump powers, thereby completely washing out the noise improvement of the seeded pulse break-up. Similarly, we found the process to be extremely sensitive to phase-noise on the seed, which limits the mechanisms that can be used to generate the seed. Rather than actively controlling the pulse break-up, we attempted

to passively tame the subsequent soliton-driven spectral dynamics with tapered fibres. This had previously been demonstrated to reduce the spectral noise across the full SC bandwidth, but we observed no such clear noise reduction. On the contrary, we found that the spectral noise follows the spectral edge irrespectively of the fibre geometry.

These results thus clearly show that seeding has little or no impact on the noise properties of commercially relevant long-pulsed high-power SC sources. Future directions would include a thorough comparison of the noise properties of SC generation in various uniform and tapered fibres. In particular, the noise measure introduced in [137] must be compared to RIN and HOMs to shed some light on whether tapers can indeed reduce the noise.

The frequency-to-time mapping technique that was first used to reveal the existence of optical rogue waves in [27], was recently used to gain insight into the stochastic nature of MI [234–236] and correlations in the full SC spectrum [216]. It seems very likely that this approach will further aid the fundamental understanding of SC noise properties, and may prove especially useful in comparing experimental results with numerical simulations.

There has currently been renewed interested in generating fully coherent SC spectra in all-normal PCFs through SPM broadening [55–61]. This further means that the SC can be temporally compressed, but it comes at the price of a limited bandwidth and requires shorter pulses. This is in many ways a return to the roots of SC generation, where a single coherent broadening mechanism is used rather than a plethora of interconnected processes. Although such sources may find applications due to their noise properties, they can not compete with the available long-pulsed sources in terms of bandwidth and average power, and it is therefore still worthwhile to investigate noise-reduction of incoherent long-pulsed SC generation.

Chapter 5

# Summary

In this thesis we have investigated various fundamental and application oriented aspects of SC generation in customised PCFs. We have focused on the commercially relevant long-pulsed high-power regime, where the spectral broadening is initiated by noise-seeded MI that breaks the pump into a distributed spectrum of redshifting solitons and DWs. Broadly speaking, we have manipulated both the initial pulse break-up by modulating the pump pulse and the subsequently soliton-driven dynamics with longitudinally invariant fibres, which permits a control of the spectral noise properties and bandwidth, respectively. This has been motivated by a large commercial potential in low-noise and spectrally blue-extended SC sources for e.g. biological applications.

The spectral bandwidth can be extended into the deep-blue region below 400 nm by shaping the dispersion and GV landscape. Specifically, PCFs with longitudinally varying dispersion and GV accommodate the ideal combination of an efficient pulse break-up near the ZDW and a subsequent spectral extension into the deep-blue by clever engineering of the GV profile. In Chapter 3 we utilised such tapered PCFs fabricated directly on the draw-tower to demonstrate SC generation with a spectral density in excess of 1 mW/nm across the entire visible region down to 390 nm. Importantly, we revisited the fundamental effect of soliton trapping in tapered fibres to introduce and verify the novel concept of a group acceleration mismatch. This allowed us to enhance the power in the spectral blue edge by optimising the taper shape. Finally, we pushed the PCF design freedom to the limit and fabricated the first PCF taper with longitudinally increasing air-fill fraction. This uniquely permits single-mode pumped SC generation down to 375 nm in one monolithic fibre device. Although more impressive results have been reported in the literature, our results provide a

highly important step towards realising a commercial deep-blue SC source. In particular, our investigations of the importance of the taper shape and the concept of group acceleration matching collectively form an important milestone, which we expect to influence the further development. We similarly consider our single-mode high air-fill fraction PCF a very promising candidate for next generation SC sources with high spectral density below 400 nm. Importantly, we expect that the conclusions drawn here can be extrapolated to generate SC spectral extending below 350 nm, which would be the obvious next step.

The initial stages of long-pulsed SC generation are dominated by noise-initiated MI that tears the pump into a train of soliton-like pulses. Because the process is driven by noise, it is responsible for large shot-to-shot variations of the resulting SC and the generation of statistically rare optical rogue waves with abnormal peak powers. In Chapter 4 we quantified these spectral variations with statistical higher-order moments. Specifically, we demonstrated the utility of the moments of coefficient of variation, skew and kurtosis, which collectively provide improved quantitative and qualitative insight into the nature of the spectral fluctuations across the spectrum, and allows easy identification of regimes of rogue wave-like statistics. The large spectral shot-to-shot fluctuations pose a limiting factor for several applications. In Chapter 4 we investigated two approaches to bring down the spectral variations in commercial SC sources. Instead of allowing noise-driven MI to break the pump into a train of soliton-like pulses, the pump can be modulated with a weak seed pulse to achieve a coherent pulse break-up. While seeding works beautifully under a large variety of initial conditions for a low pump power, the situation changes drastically when we approach the parameters of a commercial system, where the subsequent chaotic solitonic dynamics completely overpowers the coherent pulse break-up. Similarly, we numerically demonstrated that the process is highly sensitive to phase-noise on the seed pulse, which restrains the mechanisms that can be used to generate the seed. Although these results are fundamentally highly interesting in the context of e.g. rogue phenomena, our results seem to unambiguously suggest that seeding is without effect for commercial high-power systems.

Whilst controlling the pulse break-up in a high-power SC source thus seems redundant for the noise properties of the resulting SC, we instead tried to control the subsequent soliton dominated dynamics. Specifically, it has been suggested that tapered fibres could be used to lower the spectral noise by taming the soliton propagation. However, we found no immediate noise reduction in tapered PCFs. Rather, we found that the spectral noise increases with the detuning from the pump, and is at a constant noise level at the spectral edge.

In summary, in this thesis we have investigated blue-extension and enhancement of SC generation into the deep-blue in axially non-uniform PCFs and various aspects of the spectral SC noise. The results presented in this work provide new insight into the broadening mechanisms and are expected to have a direct impact on the development of the next generation of high-power SC sources with deep-blue spectra. The results are further of a fundamental importance in the context of understanding the origin of the spectral SC noise and its links with other systems.

Appendix A

# Implementing and solving the GNLSE

This appendix contains a collection of useful information on how to implement and solve the GNLSE with all the bells and whistles, such as fibre losses, noise sources, and frequency dependence of all fibre parameters. It is meant as a compilation of various bits and pieces of information that is not readily found elsewhere, and should be used to compliment the material in e.g. [1,71]. Specifically, the particular implementation of the GNLSE used in this work is introduced, where the frequency dependence of the fibre parameters is included according to [85] and the GNLSE solved in the interaction picture. It is further discussed how to include noise and attenuation in the model.

## A.1 Frequency dependence of material parameters

In the case of strong wavelength dependence of the effective area and refractive index, it has been argued by Lægsgaard [85] that the GNLSE in Eq. (2.9) does not accurately account for modal dispersion. This can be correctly included by introducing a new nonlinear coefficient

$$\gamma(\omega) = \frac{n_2 n_0 \omega_0}{c n_{\text{eff}}(\omega)\sqrt{A_{\text{eff}}(\omega)A_{\text{eff}}(\omega_0)}}, \tag{A.1}$$

where $n_0 = n_{\text{eff}}(\omega_0)$ is the effective refractive index at $\omega_0$. The resulting modified GNLSE is then

$$\frac{\partial \tilde{C}}{\partial z} = i\left[\beta(\omega) - \beta(\omega_0) - \beta_1(\omega_0)(\omega - \omega_0)\right]\tilde{C}(z,\omega) - \frac{\alpha(\omega)}{2}\tilde{C}(z,\omega) \qquad \text{(A.2)}$$
$$+ i\gamma(\omega)\left(1 + \frac{\omega - \omega_0}{\omega_0}\right)\mathcal{F}\left\{C(z,\tau)\int_{-\infty}^{+\infty} R(\tau')|C(z,\tau-\tau')|^2 d\tau'\right\},$$

where $\mathcal{F}$ is the Fourier transform and frequency domain variables are denoted with a tilde. The modified envelope $\tilde{C}$ is related to the physical envelope $\tilde{A}$ by

$$\tilde{C}(z,\omega) = \left(\frac{A_{\text{eff}}(\omega)}{A_{\text{eff}}(\omega_0)}\right)^{-1/4}\tilde{A}(z,\omega). \qquad \text{(A.3)}$$

The above equations form the basis for all the numerical simulations in this work. It should be noted that working in the frequency domain is numerically faster than working in the time domain [237], and further allows the sum over dispersion terms ($\beta_m$ coefficients) in Eq. (2.9) to be replaced with the approximation-free expression $\beta(\omega) - \beta(\omega_0) - \beta_1(\omega_0)(\omega - \omega_0)$ [71].

The modified GNLSE conserves a quantity proportional to the photon number,

$$\frac{\partial}{\partial z}\int n_{\text{eff}}(\omega)\sqrt{A_{\text{eff}}(\omega)}\frac{|\tilde{C}(z,\omega)|^2}{\omega}d\omega = 0, \qquad \text{(A.4)}$$

which can be used to check the numerical accuracy of the simulations.

For the sake of simplicity, we shall use the normal envelope $A$ in what follows. It is, however, straightforward to substitute $A$ with the modified envelope $C$.

### A.1.1 Modelling tapered fibres

Modelling pulse propagation in tapered fibres corresponds to introducing a $z$ dependence on all fibre parameters in the GNLSE. However, the interaction picture implementation discussed in the next section assumes that the fibre is invariant in each calculation step, and the taper is hence numerically modelled by updating the fibre parameters between the calculation steps. In practice, the modal properties ($\beta$, $\gamma$ and $A_{\text{eff}}$) are calculated in COMSOL as a function of wavelength for a limited number of fixed fibre parameters (hole-to-pitch ratio $d/\Lambda$ and pitch $\Lambda$), and these values are then interpolated and updated a sufficient number of times with propagation.

Vanvincq *et al.* [238] recently made a detailed derivation of a scalar propagation model and showed that an additional term is needed in Eq. (A.4)

to conserve the photon number in tapered fibres. This, however, was resolved by Lægsgaard [239] by adopting a different normalisation. In [239] it was further demonstrated that care must be taken when interpolating fibre parameters in a tapered fibre, but the exact interpolation scheme becomes less important for longer tapers like those investigated in this work. The difference in the results obtained with the normal GNLSE model and the corrected models are modest for long tapers, and all results presented here are based on the non-corrected model. It was, however, checked that the interpolation of fiber parameters was sufficiently fine.

## A.2 The interaction picture implementation

The GNLSE has traditionally been solved using the so-called *split-step Fourier method*, where the pulse envelope $A(z,t)$ is propagated over a small distance $h$ by alternately applying the dispersive and nonlinear effects, which yields $A(z+h,t)$. The nonlinear step is typically integrated with a second or fourth order Runge-Kutta solver. The local error of this scheme has a leading term that is third order in the step-size, $O(h^3)$ [71,86,237,240]. The work in this thesis is based on the closely related *four-order Runge-Kutta interaction picture* (RK4IP) method that is faster and firth-order locally accurate [86]. The RK4IP method works be expressing the GNLSE as

$$\frac{\partial A(z,\tau)}{\partial z} = \left(\hat{D} + \hat{N}\right) A(z,\tau), \tag{A.5}$$

where $\hat{D}$ and $\hat{N}$ are the dispersive and nonlinear operators, respectively,

$$\hat{D} = i \sum_{m \geq 2} \frac{i^m \beta_m}{m!} \frac{\partial^m}{\partial \tau^m}; \tag{A.6}$$

$$\hat{N}A(z,\tau) = i\gamma \left(1 + \frac{i}{\omega_0}\frac{\partial}{\partial \tau}\right) A(z,\tau) \int R(\tau')|A(z,\tau-\tau')|^2 d\tau'. \tag{A.7}$$

In the frequency-domain the operators read

$$\hat{D} = i\left(\beta(\omega) - \beta(\omega_0) - \beta_1(\omega_0)(\omega-\omega_0)\right); \tag{A.8}$$

$$\hat{N}A(z,\tau) = i\gamma \left(1 + \frac{\omega-\omega_0}{\omega_0}\right) \mathcal{F}\left\{A(z,\tau)\mathcal{F}^{-1}\left\{\tilde{R}(\omega-\omega_0)\mathcal{F}\left\{|A(z,\tau)|^2\right\}\right\}\right\}, \tag{A.9}$$

where $\mathcal{F}$ and $\mathcal{F}^{-1}$ are the Fourier and inverse Fourier transforms, respectively. The nonlinear operator is seen to involve several Fourier transforms. The RK4IP method explicitly gives the pulse envelope at $A(z+h,t)$ from

$A(z,t)$ calculated with a fourth-order Runge-Kutta solver. In the frequency domain the RK4IP scheme can be stated as follows [237]

$$\tilde{A}_I = \exp\left(\frac{h}{2}\tilde{D}\right)\tilde{A}(z,\omega) \tag{A.10}$$

$$k_1 = \exp\left(\frac{h}{2}\tilde{D}\right)\left[h\tilde{N}\left(\tilde{A}(z,\omega)\right)\right] \tag{A.11}$$

$$k_2 = h\tilde{N}\left(\tilde{A}(z,\omega) + k_1/2\right) \tag{A.12}$$

$$k_3 = h\tilde{N}\left(\tilde{A}(z,\omega) + k_2/2\right) \tag{A.13}$$

$$k_4 = h\tilde{N}\left(\exp\left(\frac{h}{2}\tilde{D}\right)\left(\tilde{A}(z,\omega) + k_3\right)\right) \tag{A.14}$$

$$\tilde{A}(z+h,\omega) = \exp\left(\frac{h}{2}\tilde{D}\right)\left[\tilde{A}_I + k_1/6 + k_2/3 + k_3/3\right] + k_4/6, \tag{A.15}$$

where $\hat{N}(\tilde{A})$ is the non-linear operator applied to $\tilde{A}$ and the $k_i$ terms are slope increments.

## A.3 Longitudinal step-size

The RK4IP can be straightforwardly implemented to calculate the evolution of the pulse envelope with propagation distance. However, treating the dispersive and nonlinear processes individually gives rise to a local error, which can be minimised with accurate numerical integration and intelligent control of longitudinal step-size.

The longitudinal step-size $h$ is thus very important for the accuracy of a given simulation, and allowing it to adapt throughout a simulation can increase the accuracy while decreasing the computational effort. In general, when the nonlinearities are low $h$ can be increased, as the error in splitting the dispersive and nonlinear processes is small. And visa-versa. An adaptive step-size can further mitigate issues with spurious FWM [86,241]. The most commonly applied method is the *local-error method* [242] that uses the step-doubling technique and local extrapolation. Each step is taken twice: once as a full step and once as two half steps, giving a coarse $u_c$ and fine $u_f$ solution. The difference between the two gives an estimate of the local error, $\delta = \|u_f - u_c\|/\|u_f\|$, and the step-size is adjusted by comparing with a predefined goal error $\delta_g$, as described in [242]. The method further gives a higher accuracy, when a linear combination of the coarse and fine solution is used as input for the following step. It does however require 50% more

Fourier transforms than the constant step-size algorithm, and is therefore not necessarily more efficient that the constant step-size algorithm.

The extra calculations needed to find both the fine and coarse solution could be speeded up by using a Runge-Kutta-Fehlberg method, where the fine solution is found by including a fifth slope increment $k_5$ to the Runge-Kutta solver, which then can be compared to the solution found using the first four slope increments. This methods was however not tested here (if it ain't broke, don't fix it).

## A.4 Numerical resolution

It is crucial to chose an appropriate numerical grid size and spacing to ensure that the involved dynamics can be correctly resolved. Thus, the width of the temporal grid should be sufficiently large to contain the pulse shape after propagating through the fibre, without any temporal wrapping arising from the large GV differences relative to the pump. The temporal grid resolution should be sufficiently fine to resolve all generated frequencies. According to the sampling theorem, the grid resolution should be at least twice the highest frequency [243].

### A.4.1 Domain size

The frequency and time domains used in the simulations are dependent on the centre wavelength $\lambda_0$ and the spacing of points in the time domain $\Delta t$. Specifically, the maximum $\lambda_{\max}$ and minimum $\lambda_{\max}$ wavelengths are [244]

$$\lambda_{\min/\max} = \left( \frac{1}{2c\Delta t} \pm \frac{1}{\lambda_0} \right)^{-1}, \tag{A.16}$$

where $\lambda_0$ often is taken as the pulse centre frequency, which may limit $\lambda_{\min}$ at a too high value. This can be improved by choosing a centre frequency of the pulse $\omega_0$ that is different from the centre frequency of the domain $\omega_{\exp}$, and in turn give the pulse an initial chirp, so that

$$A(z=0,\tau) = \sqrt{P_0}\mathrm{sech}\left(\frac{\tau}{\tau_0}\right)\exp\left(i\omega_{\exp}\tau\right), \tag{A.17}$$

which gives

$$\tilde{A}(z=0,\omega) = \sqrt{P_0}\pi\tau_0\mathrm{sech}\left(\frac{\pi}{2}\tau_0\left(\omega_{\exp}+\omega\right)\right). \tag{A.18}$$

That is, the chirp shifts the centre frequency by $\omega_{\text{exp}}$, but does otherwise not change the pulse. The situation is similar for a Gaussian pulse

$$A(z=0,\tau) = \sqrt{P_0}\exp\left(\frac{-\tau^2}{2\tau_0^2}\right)\exp\left(i\omega_{\text{exp}}\tau\right); \tag{A.19}$$

$$\tilde{A}(z=0,\omega) = \sqrt{P_0}\sqrt{2\pi}\tau_0\exp\left(-\frac{1}{2}\tau_0^2(\omega+\omega_{\text{exp}})^2\right). \tag{A.20}$$

The GNLSE is derived in the retarded frame of reference moving with the GV of the carrier frequency of the pulse ($\omega_{\text{exp}}$), and the dispersion operator must be changed to

$$\hat{D}(\omega) = \beta(\omega) - \beta_0(\omega_{\text{exp}}) - \beta_1(\omega_0)(\omega-\omega_{\text{exp}}) \tag{A.21}$$

in order to compensate for this. Here $\beta_0(\omega_{\text{exp}})$ is the zeroth $\beta$-coefficient expanded at $\omega_{\text{exp}}$, and $\beta_1(\omega_0)$ the first $\beta$-coefficient expanded at $\omega_0$. It should also be noticed that Eq. (A.16) dictates $\Delta t > \lambda_0/(2c)$ in order to avoid negative frequency components.

**Fibre parameters**

When using $\omega_{\text{exp}} \neq \omega_0$ one must take care in the definitions of the fibre parameters. That is, the nonlinear coefficient is given by (using the standard definition)

$$\gamma(\omega) = \frac{n_2\omega_{\text{exp}}}{cA_{\text{eff}}(\omega)}, \tag{A.22}$$

but when calculating e.g. the peak power of a soliton $P_0 = |\beta_2|/(\tau_0^2\gamma)$ the correct expression reads

$$\gamma(\omega) = \frac{n_2\omega_0}{cA_{\text{eff}}(\omega)}. \tag{A.23}$$

The first definition is used when defining the vector used in the simulation, as this must be the same independently on the input pulse. That latter definition, on the other hand, is directly related to the pulse, and must be independent on the chosen expansion frequency.

## A.5 Noise sources

Nonlinear pulse propagation in optical fibres is highly influenced by noise, and noise sources must be included in simulations to obtain meaningful results. This section describes two such numerical noise sources: the *one photon per mode* background noise model and the *phase-diffusion* laser linewidth model.

### A.5.1 One photon per mode model

Noise on the input field is commonly included as a fictitious field consisting of one photon with a random phase in each spectral discretisational bin. Smith [245] showed that the Raman amplification of spontaneous emission in a fibre is equivalent to injecting this one photon per mode field. Inclusion of background noise is highly important for MI-initiated SC generation.

It is straightforward to include this model: the envelope at frequency bin $\nu_n$ of a field consisting of one photon per mode with random phase is

$$\tilde{A}(\nu_n) = (T_{\max} h\nu)^{1/2} \exp\left\{i\phi(\nu_n)\right\}, \tag{A.24}$$

where $\phi(\nu_n)$ is a random spectral phase in the interval $[0; 2\pi]$ and $T_{\max}$ the width of the temporal window. The Fourier transform of $\tilde{A}(\nu_n)$ can then be added to the input field.

### A.5.2 Phase-diffusion model

In addition to the background noise from the one photon per mode model, it is often necessary to include the spectral noise linewidth of the laser. The phase-diffusion model naturally includes a spectral linewidth and leads to a Lorentzian spectrum of the laser. The Lorentzian spectrum can, however, be reshaped into a Gaussian spectrum [246]. The underlying physics is well-founded [247, 248].

The starting point is the input envelope of the quasi-CW field with power $P(\tau)$

$$A(0,\tau) = \sqrt{P(\tau)} \exp\left(i\delta\phi(\tau)\right), \tag{A.25}$$

where $\delta\phi(\tau)$ is a small fluctuation with $\langle\delta\phi(\tau)\rangle = 0$. The fluctuations correspond to random phase fluctuations $\nu_R$ of the (CW) frequency $\nu_0$, resulting in an instantaneous frequency

$$\nu_i = \nu_0 + \frac{1}{2\pi}\frac{d\delta\phi}{d\tau} = \nu_0 + \nu_R(\tau). \tag{A.26}$$

The phase fluctuation is hence

$$\delta\phi(\tau) = 2\pi \int_{-\infty}^{\tau} \nu_R(\eta) d\eta, \tag{A.27}$$

where $\nu_R(\tau)$ is modelled as white noise with zero mean and variance, $\sigma^2_{\nu_R}$. The variance is related to the FWHM spectral linewidth of the spectrum $\Delta\nu_{\mathrm{FWHM}}$

$$\sigma^2_{\nu_R} = \frac{\Delta\nu_{\mathrm{FWHM}} B}{2\pi}, \tag{A.28}$$

where $B = 1/\Delta t$ is the bandwidth of the spectral window. These equations form the basis for the phase-diffusion model, and provide an input field envelope $A(0, \tau)$ with the Lorentzian power spectrum

$$|\tilde{A}_L(\omega)|^2 = P_{avg} \frac{\Delta\nu_{\mathrm{FWHM}}}{2\pi} \frac{1}{(\nu - \nu_0)^2 + (\Delta\nu_{\mathrm{FWHM}}/2)^2}. \tag{A.29}$$

Note that $\int_0^\infty |\tilde{A}_L(\omega)|^2 d\omega = P_{avg}$. This can be reshaped into Gaussian spectrum with same average power [246].

## A.6 Attenuation in optical fibres

The attenuation, or power loss, of an optical signal with propagation distance is an important parameter in optical fibres. Generally, if a signal with power $P_0$ propagates though a fiber, the transmitted power $P_T$ can be described as

$$P_T = P_0 \exp(-\alpha L), \tag{A.30}$$

where the constant $\alpha$ contains all attenuations sources and $L$ is the progation distance. The attenuation is often expressed in units of dB/km [71]

$$\alpha_{\mathrm{dB}} = -\frac{1}{L} 10 \log_{10} \left( \frac{P_T}{P_0} \right) = -\frac{1}{L} 10 \log_{10}(\exp(-\alpha L)) \approx 4.343\alpha. \tag{A.31}$$

The attenuation originates from several physical processes. Pure silica glass has a very low loss over the full range 500-2000 nm, but shows increasing absorption above and below this region due to electronic resonances in the ultraviolet and vibrational resonances in the mid/far-infrared, respectively. These losses are intrinsic material properties of silica, and are known to depend exponentially on the photon energy [78, 136]

$$\alpha_{\mathrm{UV}} = a_{\mathrm{UV}} \exp\left(\lambda_{\mathrm{UV}}/\lambda\right) \tag{A.32}$$

$$\alpha_{\mathrm{IR}} = a_{\mathrm{IR}} \exp\left(-\lambda_{\mathrm{IR}}/\lambda\right), \tag{A.33}$$

where $a_{\mathrm{UV}} = 0.001$ dB/km, $\lambda_{\mathrm{UV}} = 4.67$ $\mu$m, and $a_{\mathrm{IR}} = 6 \cdot 10^{11}$ dB/km, $\lambda_{\mathrm{UV}} = 47.8$ $\mu$m. The values for the UV loss are from [249] and the IR from [136, 184]. According to these values, the loss at 350 nm is 1.6 dB/m.

Local fluctuations in the refractive index due to density fluctuations in silica from the fabrication causes scattering in all direction, also known as *Raleigh scattering*. This scattering depends strongly on the wavelength. Raleigh scattering is accompanied by wavelength independent imperfection scattering due to inhomogeneities of the fiber [136]

$$\alpha_{\mathrm{sc}} = a_{\mathrm{Ray}}/\lambda^4 + c_{\mathrm{sc}}, \tag{A.34}$$

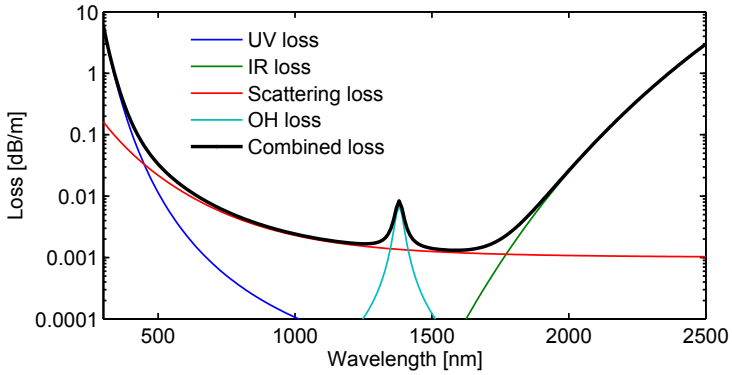


**Figure A.1:** Plot of the individual and combined losses mentioned in this section.

where $a_{\mathrm{Ray}} = 1.3$ dB/(km $\mu$m$^4$), $c_{\mathrm{sc}} = 1.0$ dB/km was measured for a commercial PCF in [136].

Impurities will add to the attenuation, and most important is the characteristic absorption peak near 1.4 $\mu$m, which stems from the presence of water. The OH ion has a fundamental vibrational resonance at 2.73 $\mu$m, and the overtones of this resonance causes the strong absorption peak in the near infrared. In [136] the OH absorption was found to be well described by a Lorentzian profile

$$\alpha_{\mathrm{OH}} = a_{\mathrm{OH}}/(1 + ((\lambda - \lambda_{\mathrm{OH}})/c_{\mathrm{OH}})^2) \tag{A.35}$$

with parameters $a_{\mathrm{OH}} = 7$ dB/km, $c_{\mathrm{OH}} = 16$ nm, $\lambda_{\mathrm{OH}} = 1,380$ nm found for a typical commercial PCF. The parameter $a_{\mathrm{OH}}$ reflects the OH content.

The individual and combined losses are shown in Fig. A.1. In simulations with long pulses and fibre lengths below 10 m, only the UV and IR losses are high enough to have any significant effects on the SC generation. However, many PCFs have significantly higher OH losses, which can be detrimental for SC generation. Additionally, PCFs have confinement losses due to light leakage from the core to the microstructured cladding. These losses are thus strongly dependent on the fibre structure and can generally be limited by increasing the number of air-hole rings. The confinement losses can be calculated from the imaginary part of the refractive index, although the values obtained from finite element solvers like COMSOL tend to be rather unreliable.

## A.7 Pulse parameters

**Gaussian pulse**

| | |
|---|---|
| Envelope (time domain): | $A(\tau) = \sqrt{P_0}\exp\left(-\tau^2/(2\tau_0^2)\right)$ |
| Envelope (freq. domain): | $\tilde{A}(\omega) = \sqrt{2\pi}\sqrt{P_0}\tau_0\exp\left(-\frac{1}{2}\tau_0^2\omega^2\right)$ |
| Intensity FWHM: | $\tau_{\mathrm{FWHM}} = 2\sqrt{\ln(2)}\tau_0 \approx 1.6651\tau_0$ |
| | $\omega_{\mathrm{FWHM}} = 4\ln(2)/\tau_{\mathrm{FWHM}}$ |
| | $\approx 2.77/\tau_{\mathrm{FWHM}}$ |
| | $\lambda_{\mathrm{FWHM}} \approx \lambda_0^2/(2\pi c)\omega_{\mathrm{FWHM}}$ |
| | $\approx 0.441\lambda_0^2/(c\tau_{\mathrm{FWHM}})$ |
| Energy: | $E = \int_{-\infty}^{\infty}\lvert A(t)\rvert^2 dt = \sqrt{\pi}P_0\tau_0$ |
| Avg. power: | $P_{avg} = Ef_{rep} = \sqrt{\pi}P_0\tau_0 f_{rep}$ |

**Sech pulse**

| | |
|---|---|
| Envelope (time domain): | $A(\tau) = \sqrt{P_0}\mathrm{sech}\left(\tau/\tau_0\right)$ |
| Envelope (freq. domain): | $\tilde{A}(\omega) = \pi\sqrt{P_0}\tau_0\mathrm{sech}\left(\frac{\pi}{2}\tau_0\omega\right)$ |
| Intensity FWHM: | $\tau_{\mathrm{FWHM}} = 2\ln(1+\sqrt{2})\tau_0 \approx 1.7627\tau_0$ |
| | $\omega_{\mathrm{FWHM}} = (2\sqrt{\ln(2)}\ln(1+\sqrt{2}))/(\pi\tau_{\mathrm{FWHM}})$ |
| | $\approx 0.4671/\tau_{\mathrm{FWHM}}$ |
| | $\lambda_{\mathrm{FWHM}} \approx \lambda_0^2/(2\pi c)\omega_{\mathrm{FWHM}}$ |
| | $\approx 0.07435\lambda_0^2/(c\tau_{\mathrm{FWHM}})$ |
| Energy: | $E = \int_{-\infty}^{\infty}\lvert A(t)\rvert^2 dt = 2P_0\tau_0$ |
| Avg. power: | $P_{avg} = Ef_{rep} = 2P_0\tau_0 f_{rep}$ |

# Paper I

## Optimum fiber tapers for increasing the power in the blue edge of a supercontinuum — group-acceleration matching

S. T. Sørensen, A. Judge, C. L. Thomsen, and O. Bang
Opt. Lett. **36**, 816–818 (2011).

**Abstract:** We demonstrate how the gradient of the tapering in a tapered fiber can significantly affect the trapping and blueshift of dispersive waves (DWs) by a soliton. By modeling the propagation of a fundamental 10 fs soliton through tapered fibers with varying gradients, it is shown that the soliton traps and blueshifts an increased fraction of the energy in its DW when the gradient is decreased. This is quantified by the group-acceleration mismatch between the soliton and DW at the entrance of the taper. These findings have direct implications for the achievable power in the blue edge of a supercontinuum generated in a tapered fiber and explain observations of a lack of power in the blue edge.

http://dx.doi.org/10.1364/OL.36.000816

# Paper II

## Deep-blue supercontinnum sources with optimum taper profiles – verification of GAM

S. T. Sørensen, U. Møller, C. Larsen, P. M. Moselund, C. Jakobsen, J. Johansen, T. V. Andersen, C. L. Thomsen, and O. Bang
Opt. Express **20**, 10635-10645 (2012).

**Abstract:** We use an asymmetric 2 m draw-tower photonic crystal fiber taper to demonstrate that the taper profile needs careful optimisation if you want to develop a supercontinuum light source with as much power as possible in the blue edge of the spectrum. In particular we show, that for a given taper length, the downtapering should be as long as possible. We argue how this may be explained by the concept of group-acceleration mismatch (GAM) and we confirm the results using conventional symmetrical short tapers made on a taper station, which have varying downtapering lengths.

http://dx.doi.org/10.1364/OE.20.01063

# Paper III

## Optimum PCF tapers for blue-enhanced supercontinuum sources [Invited]

U. Møller, S. T. Sørensen, C. Larsen, P. M. Moselund, C. Jakobsen, J. Johansen, C. L. Thomsen, O. Bang
Opt. Fiber Technol. **18**, 304-314 (2012).

**Abstract:** Tapering of photonic crystal fibers has proven to be an effective way of blueshifting the dispersive wavelength edge of a supercontinuum spectrum down in the deep-blue. In this article we will review the state-of-the-art in fiber tapers, and discuss the underlying mechanisms of supercontinuum generation in tapers. We show, by introducing the concept of a group-acceleration mismatch, that for a given taper length, the downtapering section should be as long as possible to enhance the amount of blueshifted light. We also discuss the noise properties of supercontinuum generation in uniform and tapered fibers, and we demonstrate that the intensity noise at the spectral edges of the generated supercontinuum is at a constant level independent on the pump power in both tapered and uniform fibers.

http://dx.doi.org/10.1016/j.yofte.2012.07.010

# Paper IV

## Single-mode high air-fill fraction photonic crystal fiber for high-power deep-blue supercontinuum sources

S. T. Sørensen, C. Larsen, C. Jakobsen, C. L. Thomsen, and O. Bang
Submitted to Opt. Lett. 29 April 2013

**Abstract:** Dispersion control with axially nonuniform photonic crystal fibers (PCFs) permits supercontinuum (SC) generation into the deep-blue from an ytterbium pump laser. In this letter, we exploit the full degrees of freedom afforded by PCFs to fabricate a fiber with longitudinally increasing air-fill fraction and decreasing diameter directly at the draw-tower. We demonstrate SC generation extending down to 375 nm in one such monolithic fiber device that is single-mode at 1064 nm at the input end.

# Paper V

## Describing supercontinuum noise and rogue wave statistics using higher-order moments

S. T. Sørensen, O. Bang, B. Wetzel, J. M. Dudley
Opt. Comm. **285**, 2451-2455 (2012).

**Abstract:** We show that the noise properties of fiber supercontinuum generation and the appearance of long-tailed rogue wave statistics can be accurately quantified using statistical higher-order central moments. Statistical measures of skew and kurtosis, as well as the coefficient of variation provide improved insight into the nature of spectral fluctuations across the supercontinuum and allow regions of long-tailed statistics to be clearly identified. These moments that depend only on analyzing intensity fluctuations provide a complementary tool to phase-dependent coherence measures to interpret supercontinuum noise.

http://dx.doi.org/10.1016/j.optcom.2012.01.030

# Paper VI

## Influence of pump power and modulation instability gain spectrum on seeded supercontinuum and rogue wave generation

S. T. Sørensen, C. Larsen, U. Møller, P. M. Moselund, C. L. Thomsen, and O. Bang
J. Opt. Soc. Am. B **29**, 2875-2885 (2012).

**Abstract:** The noise properties of a supercontiuum can be significantly improved both in terms of coherence and intensity stability by modulating the input pulse with a seed. In this paper, we numerically investigate the influence of the seed wavelength, the pump power, and the modulation instability gain spectrum on the seeding process. The results can be clearly divided into a number of distinct dynamical regimes depending on the initial four-wave mixing process. We further demonstrate that seeding can be used to generate coherent and incoherent rogue waves, depending on the modulation instability gain spectrum. Finally, we show that the coherent pulse breakup afforded by seeding is washed out by turbulent solitonic dynamics when the pump power is increased to the kilowatt level. Thus our results show that seeding cannot improve the noise performance of a high power supercontinuum source.

http://dx.doi.org/10.1364/JOSAB.29.002875

# Paper VII

## The role of phase coherence in seeded supercontinuum generation

S. T. Sørensen, C. Larsen, U. Møller, P. M. Moselund, C. L. Thomsen, and O. Bang
Opt. Express **20**, 22886-22894 (2012).

**Abstract:** The noise properties of a supercontinuum can be controlled by modulating the pump with a seed pulse. In this paper, we numerically investigate the influence of seeding with a partially phase coherent weak pulse or continuous wave. We demonstrate that the noise properties of the generated supercontinuum are highly sensitive to the degree of phase noise of the seed and that a nearly coherent seed pulse is needed to achieve a coherent pulse break-up and low noise supercontinuum. The specific maximum allowable linewidth of the seed laser is found to decrease with increasing pump power.

http://dx.doi.org/10.1364/OE.20.022886

# Paper VIII

## Power dependence of supercontinuum noise in uniform and tapered PCFs

U. Møller, S. T. Sørensen, C. Jakobsen, J. Johansen, P. M. Moselund, C. L. Thomsen, and O. Bang
Opt. Express **20**, 2851-2857 (2012)

**Abstract:** We experimentally investigate the noise properties of picosecond supercontinuum spectra generated at different power levels in uniform and tapered photonic crystal fibers. We show that the noise at the spectral edges of the generated supercontinuum is at a constant level independent on the pump power in both tapered and uniform fibers. At high input power the spectral bandwidth is limited by the infrared loss edge, this however has no effect on the noise properties.

http://dx.doi.org/10.1364/OE.20.002851

## Erratum

Opt. Express **20**, 23318-23319 (2012).

**Abstract:** An error was made in the calculation of the relative intensity noise (RIN) because of an incorrectly specified value of the photodetector DC transimpedance gain.

http://dx.doi.org/10.1364/OE.20.023318

# Bibliography


[1] J. M. Dudley, G. Genty, and S. Coen, "Supercontinuum generation in photonic crystal fiber," Rev. Mod. Phys. **78**, 1135–1184 (2006).

[2] J. M. Dudley and J. R. Taylor, "Ten years of nonlinear optics in photonic crystal fibre," Nat. Photon. **3**, 85–90 (2009).

[3] R. Alfano and S. Shapiro, "Observation of self-phase modulation and small-scale filaments in crystals and glasses," Phys. Rev. Lett. **24**, 592–594 (1970).

[4] R. Alfano and S. Shapiro, "Emission in the region 4000 to 7000 Åvia four-photon coupling in glass," Phys. Rev. Lett. **24**, 584–588 (1970).

[5] C. Lin and R. H. Stolen, "New nanosecond continuum for excited-state spectroscopy," Appl. Phys. Lett. **28**, 216 (1976).

[6] C. Lin, V. T. Nguyen, and W. G. French, "Wideband near-I.R. continuum (0.7-2.1 um) generated in low-loss optical fibres," Electron. Lett. **14**, 822–823 (1978).

[7] J. Knight, T. Birks, P. Russell, and D. Atkin, "All-silica single-mode optical fiber with photonic crystal cladding," Opt. Lett. **21**, 1547–1549 (1996).

[8] J. Knight, T. Birks, P. Russell, and D. Atkin, "All-silica single-mode optical fiber with photonic crystal cladding: errata," Opt. Lett. **22**, 484–485 (1997).

[9] J. Broeng, D. Mogilevstev, S. E. Barkou, and A. Bjarklev, "Photonic Crystal Fibers: A New Class of Optical Waveguides," Opt. Fiber Technol. **5**, 305–330 (1999).

[10] P. Russell, "Photonic crystal fibers," Science **299**, 358–62 (2003).

[11] P. S. J. Russell, "Photonic crystal fibers," J. Lightwave Technol. **24**, 4729–4749 (2006).

[12] J. Ranka, R. Windeler, and A. Stentz, "Visible continuum generation in air-silica microstructure optical fibers with anomalous dispersion at 800 nm," Opt. Lett. **25**, 25–27 (2000).

[13] J. M. Dudley, G. Genty, F. Dias, B. Kibler, and N. Akhmediev, "Modulation instability, Akhmediev Breathers and continuous wave supercontinuum generation," Opt. Express **17**, 21497–508 (2009).

[14] J. Herrmann, U. Griebner, N. Zhavoronkov, A. Husakou, D. Nickel, J. C. Knight, W. J. Wadsworth, P. S. J. Russell, and G. Korn, "Experimental Evidence for Supercontinuum Generation by Fission of Higher-Order Solitons in Photonic Fibers," Phys. Rev. Lett. **88**, 1–4 (2002).

[15] T. A. Birks, J. C. Knight, and P. S. Russell, "Endlessly single-mode photonic crystal fiber," Opt. Lett. **22**, 961–3 (1997).

[16] J. C. Knight, "Photonic crystal fibres," Nature **424**, 847–51 (2003).

[17] A. Hasegawa, "Generation of a train of soliton pulses by induced modulational instability in optical fibers," Opt. Lett. **9**, 288–90 (1984).

[18] K. Tai, A. Tomita, J. L. Jewell, and A. Hasegawa, "Generation of subpicosecond solitonlike optical pulses at 0.3 THz repetition rate by induced modulational instability," Appl. Phys. Lett. **49**, 236 (1986).

[19] M. Islam, G. Sucha, and I. Bar-Joseph, "Broad bandwidths from frequency-shifting solitons in fibers," Opt. Lett. **14**, 370–372 (1989).

[20] C. Y. Wang, P. L. Baldeck, Y. Budansky, and R. R. Alfano, "15-THz pulse generation arising from modulation instability oscillation in a colliding-pulse mode-locking dye laser." Opt. Lett. **14**, 497–9 (1989).

[21] E. J. Greer, D. M. Patrick, P. G. J. Wigley, and J. R. Taylor, "Generation of 2 THz repetition rare pulse trains through induced modulation instability," Electron. Lett. **25**, 1246–1248 (1989).

[22] E. M. Dianov, P. V. Mamyshev, A. M. Prokhorov, and S. V. Chernikov, "Generation of a train of fundamental solitons at a high repetition rate in optical fibers," Opt. Lett. **14**, 1008–10 (1989).

[23] P. Mamyshev and S. Chernikov, "Generation of a high-repetition-rate train of practically noninteracting solitons by using the induced modulational instability and Raman self-scattering effects," Opt. Lett. **15**, 1365–1367 (1990).

[24] V. Karpman and E. Krushkal, "Modulated waves in nonlinear dispersive media," Sov. Phys. JETP **28** (1969).

[25] N. Akhmediev and V. Korneev, "Modulation instability and periodic solutions of the nonlinear Schrödinger equation," Theor. Mat. Phys. **69** (1986).

[26] K. Tai, A. Hasegawa, and A. Tomita, "Observation of modulational instability in optical fibers," Phys. Rev. Lett. **56**, 0–4 (1986).

[27] D. R. Solli, C. Ropers, P. Koonath, and B. Jalali, "Optical rogue waves," Nature Lett. **450**, 1054–7 (2007).

[28] P. Müller, C. Garrett, and A. Osborne, "Rogue Waves - The fourteenth 'Aha Huliko'a Hawaiian Winter Workshop," Oceanography **18**, 66–75 (2005).

[29] N. Akhmediev, J. Soto-Crespo, and A. Ankiewicz, "Extreme waves that appear from nowhere: On the nature of rogue waves," Phys. Lett. A **373**, 2137–2145 (2009).

[30] N. Akhmediev, J. Soto-Crespo, and A. Ankiewicz, "Could rogue waves be used as efficient weapons against enemy ships?" Eur. Phys. J. **185**, 259–266 (2010).

[31] Y. Zhen-Ya, "Financial rogue waves," Commun. Theor. Phys. **54**, 947–949 (2010).

[32] O. Bang and M. Peyrard, "Generation of high-energy localized vibrational modes in nonlinear Klein-Gordon lattices," Phys. Rev. E **53** (1996).

[33] A. Husakou and J. Herrmann, "Supercontinuum generation of higher-order solitons by fission in photonic crystal fibers," Phys. Rev. Lett. **1**, 85–88 (2001).

[34] D. V. Skryabin, F. Luan, J. C. Knight, and P. S. J. Russell, "Soliton self-frequency shift cancellation in photonic crystal fibers," Science **301**, 1705–8 (2003).

[35] P. Beaud, W. Hodel, B. Zysset, and H. P. Weber, "Ultrashort pulse propagation, pulse breakup, and fundamental soliton formation in a single-mode optical fiber," IEEE J. Quantum Electron. **QE-23**, 1938–1946 (1987).

[36] A. V. Gorbach and D. V. Skryabin, "Theory of radiation trapping by the accelerating solitons in optical fibers," Phys. Rev. A **76**, 1–10 (2007).

[37] A. V. Gorbach and D. V. Skryabin, "Light trapping in gravity-like potentials and expansion of supercontinuum spectra in photonic-crystal fibres," Nat. Photon. **1**, 653–657 (2007).

[38] J. M. Stone and J. C. Knight, "Visibly "white" light generation in uniform photonic crystal fiber using a microchip laser," Opt. Express **16**, 2670–5 (2008).

[39] A. Kudlinski and G. Bouwmans, "Dispersion-engineered photonic crystal fibers for CW-pumped supercontinuum sources," J. Lightwave Technol. **27**, 1556–1564 (2009).

[40] J. C. Travers, "Blue extension of optical fibre supercontinuum generation," J. Opt. **12**, 113001 (2010).

[41] I. Hartl, X. D. Li, C. Chudoba, R. K. Ghanta, T. H. Ko, J. G. Fujimoto, J. K. Ranka, and R. S. Windeler, "Ultrahigh-resolution optical coherence tomography using continuum generation in an air-silica microstructure optical fiber." Opt. Lett. **26**, 608–10 (2001).

[42] B. Povazay, K. Bizheva, A. Unterhuber, B. Hermann, H. Sattmann, A. F. Fercher, W. Drexler, A. Apolonski, W. J. Wadsworth, J. C. Knight, P. S. J. Russell, M. Vetterlein, and E. Scherzer, "Submicrometer axial resolution optical coherence tomography." Opt. Lett. **27**, 1800–2 (2002).

[43] G. Humbert, W. Wadsworth, S. Leon-Saval, J. Knight, T. Birks, P. St J Russell, M. Lederer, D. Kopf, K. Wiesauer, E. Breuer, and D. Stifter, "Supercontinuum generation system for optical coherence tomography based on tapered photonic crystal fibre." Opt. Express **14**, 1596–603 (2006).

[44] G. McConnell, "Confocal laser scanning fluorescence microscopy with a visible continuum source," Opt. Express **12**, 2844–2850 (2004).

[45] J. Frank, A. Elder, J. Swartling, A. Venkitaraman, A. Jeyasekharan, and C. Kaminski, "A white light confocal microscope for spectrally resolved multidimensional imaging," J. Microscopy **227**, 203–215 (2007).

[46] D. Jones, D. J. Jones, S. A. Diddams, J. K. Ranka, A. Stentz, R. S. Windeler, J. L. Hall, and S. T. Cundiff, "Carrier-envelope phase control of femtosecond mode-locked lasers and direct optical frequency synthesis," Science **288**, 635–40 (2000).

[47] R. Holzwarth, T. Udem, T. Hansch, J. Knight, W. Wadsworth, and P. Russell, "Optical frequency synthesizer for precision spectroscopy," Phys. Rev. Lett. **85**, 2264–7 (2000).

[48] S. A. Diddams, T. Udem, J. C. Bergquist, E. A. Curtis, R. E. Drullinger, L. Hollberg, W. M. Itano, W. D. Lee, C. W. Oates, K. R. Vogel, and D. J. Wineland, "An optical clock based on a single trapped 199Hg+ ion," Science **293**, 825–8 (2001).

[49] T. Udem, R. Holzwarth, and T. W. Hänsch, "Optical frequency metrology." Nature **416**, 233–7 (2002).

[50] A. Ruehl, "Advances in Yb: Fiber Frequency Comb Technology," Opt. Photonics News pp. 30–35 (2012).

[51] M. Peach and M. Hatcher, "Supercontinuum sources make their presence felt," http://optics.org/news/4/2/7 (12 Feb. 2013) .

[52] A. Kudlinski, G. Bouwmans, O. Vanvincq, Y. Quiquempois, A. Le Rouge, L. Bigot, G. Mélin, and A. Mussot, "White-light cw-pumped supercontinuum generation in highly GeO(2)-doped-core photonic crystal fibers," Opt. Lett. **34**, 3631–3 (2009).

[53] C. Larsen, D. Noordegraaf, P. M. W. Skovgaard, K. P. Hansen, K. E. Mattsson, and O. Bang, "Gain-switched CW fiber laser for improved supercontinuum generation in a PCF," Opt. Express **19**, 3631–3633 (2011).

[54] A. Kudlinski and A. Mussot, "Optimization of continuous-wave supercontinuum generation," Opt. Fiber Technol. **18**, 322–326 (2012).

[55] M. Nakazawa, H. Kubota, and K. Tamura, "Random evolution and coherence degradation of a high-order optical soliton train in the presence of noise," Opt. Lett. **24**, 318–320 (1999).

[56] A. Heidt, "Pulse preserving flat-top supercontinuum generation in all-normal dispersion photonic crystal fibers," J. Opt. Soc. Am. B **27**, 550–559 (2010).

[57] A. M. Heidt, A. Hartung, G. W. Bosman, P. Krok, E. G. Rohwer, H. Schwoerer, and H. Bartelt, "Coherent octave spanning near-infrared and visible supercontinuum generation in all-normal dispersion photonic crystal fibers," Optics express **19**, 3775–87 (2011).

[58] A. M. Heidt, J. Rothhardt, A. Hartung, H. Bartelt, E. G. Rohwer, J. Limpert, and A. Tünnermann, "High quality sub-two cycle pulses from compression of supercontinuum generated in all-normal dispersion photonic crystal fiber," Optics Express **19**, 13873 (2011).

[59] A. Hartung, A. M. Heidt, and H. Bartelt, "Pulse-preserving broadband visible supercontinuum generation in all-normal dispersion tapered suspended-core optical fibers," Opt. Express **19**, 12275–12283 (2011).

[60] L. Hooper, P. Mosley, and A. Muir, "Coherent supercontinuum generation in photonic crystal fiber with all-normal group velocity dispersion," Opt. Express **19**, 4902–4907 (2011).

[61] A. Heidt, F. Poletti, J. Price, and D. J. Richardson, "Mid-IR coherent supercontinuum generation in all-solid step-index soft glass fibers," Specialty Optical Fibers, OSA **559**, paper STu3F.6 (2012).

[62] C. Xia, M. Kumar, O. P. Kulkarni, M. N. Islam, F. L. Terry, M. J. Freeman, M. Poulain, and G. Mazé, "Mid-infrared supercontinuum generation to 4.5 um in ZBLAN fluoride fibers by nanosecond diode pumping," Opt. Lett. **31**, 2553–2555 (2006).

[63] P. Domachuk, N. A. Wolchover, M. Cronin-Golomb, A. Wang, A. K. George, C. M. B. Cordeiro, J. C. Knight, and F. G. Omenetto, "Over 4000 nm bandwidth of mid-IR supercontinuum generation in sub-centimeter segments of highly nonlinear tellurite PCFs," Opt. Express **16**, 7161–8 (2008).

[64] G. Qin, X. Yan, C. Kito, M. Liao, C. Chaudhari, T. Suzuki, and Y. Ohishi, "Supercontinuum generation spanning over three octaves from UV to 3.85 microm in a fluoride fiber," Opt. Lett. **34**, 2015–7 (2009).

[65] C. Agger, C. Petersen, S. Dupont, H. Steffensen, J. K. Lyngsø, C. L. Thomsen, J. Thøgersen, S. R. Keiding, and O. Bang, "Supercontinuum generation in ZBLAN fibersdetailed comparison between measurement and simulation," J. Opt. Soc. Am. B **29** (2012).

[66] A. Kudlinski, A. K. George, J. C. Knight, J. C. Travers, A. B. Rulkov, S. V. Popov, and J. R. Taylor, "Zero-dispersion wavelength decreasing photonic crystal fibers for ultraviolet-extended supercontinuum generation," Opt. Express **14**, 5715 (2006).

[67] J. C. Travers, A. B. Rulkov, S. V. Popov, J. R. Taylor, A. Kudlinski, a. K. George, and J. C. Knight, "Multi-Watt Supercontinuum Generation from 0.3 to 2.4 um in PCF Tapers," in "Conference on Lasers and Electro-Optics," (IEEE, 2007), p. paper JTuB2.

[68] J. Stone and J. Knight, "From zero dispersion to group index matching: How tapering fibers offers the best of both worlds for visible supercontinuum generation," Opt. Fiber Technol. **18**, 315–321 (2012).

[69] S. P. Stark, J. C. Travers, and P. S. J. Russell, "Extreme supercontinuum generation to the deep UV," Opt. Lett. **37**, 770–772 (2012).

[70] A. Kudlinski, M. Lelek, B. Barviau, L. Audry, and A. Mussot, "Efficient blue conversion from a 1064 nm microchip laser in long photonic crystal fiber tapers for fluorescence microscopy," Opt. Express **18**, 16640–5 (2010).

[71] G. P. Agrawal, *Nonlinear Fiber Optics* (Academic Press, 2006), 4th ed.

[72] P. Kaiser and H. Astle, "Low-loss single-material fibers made from pure fused silica," Bell Syst. Tech. J. **53**, 1021–1039 (1974).

[73] T. Birks, P. Roberts, P. Russell, M. Atkin, and T. Shepherd, "Full 2-D photonic bandgaps in silica/air structures," IEEE Electron. Lett. **31**, 1941–1943 (1995).

[74] J. C. Knight, "Photonic Band Gap Guidance in Optical Fibers," Science **282**, 1476–1478 (1998).

[75] R. F. Cregan, B. J. Mangan, J. C. Knight, T. A. Birks, P. S. J. Russell, P. J. Roberts, and D. C. Allan, "Single-Mode Photonic Band Gap Guidance of Light in Air," Science **285**, 1537–1539 (1999).

[76] D. Mogilevtsev, T. Birks, and P. Russell, "Group-velocity dispersion in photonic crystal fibers," Opt. Lett. **23**, 1662–1664 (1998).

[77] O. Humbach, H. Fabian, and U. Grzesik, "Analysis of OH absorption bands in synthetic silica," J. Non-Cryst. Sol. **203**, 19–26 (1996).

[78] S. Walker, "Rapid modeling and estimation of total spectral loss in optical fibers," J. Lightwave Technol. **LT-4**, 1125–1131 (1986).

[79] P. Roberts, F. Couny, H. Sabert, B. Mangan, T. Birks, J. Knight, and P. Russell, "Loss in solid-core photonic crystal fibers due to interface roughness scattering," Opt. Express **13**, 7779–93 (2005).

[80] M. Phan-Huy, J. Moison, J. A. Levenson, S. Richard, G. Mélin, M. Douay, and Y. Quiquempois, "Surface roughness and light scattering in a small effective area microstructured fiber," J. Lightwave Technol. **27**, 1597–1604 (2009).

[81] W. Wadsworth, J. Knight, and T. Birks, "State-of-the-Art Photonic Crystal Fiber," Opt. Photonics News pp. 24–31 (2012).

[82] I. Gris-Sánchez, B. Mangan, and J. Knight, "Reducing spectral attenuation in small-core photonic crystal fibers," Opt. Mater. Express **1**, 179 (2011).

[83] K. J. Blow and D. Wood, "Theoretical Description of Transient Stimulated Raman Scattering in Optical Fibers," IEEE J. Quantum Electron. **25**, 2665–2673 (1989).

[84] J. Lægsgaard, N. A. Mortensen, and A. Bjarklev, "Mode areas and field-energy distribution in honeycomb photonic bandgap fibers," J. Opt. Soc. Am. B **20**, 2037 (2003).

[85] J. Lægsgaard, "Mode profile dispersion in the generalised nonlinear Schrödinger equation," Opt. Express **15**, 337–342 (2007).

[86] J. Hult, "A Fourth-Order RungeKutta in the Interaction Picture Method for Simulating Supercontinuum Generation in Optical Fibers," J. Lightwave Technol. **25**, 3770–3775 (2007).

[87] E. Treacy, "Measurement and interpretation of dynamic spectrograms of picosecond light pulses," J. Appl. Phys. **42** (1971).

[88] R. Trebino, *Frequency-resolved optical gating: the measurement of ultrashort laser pulses* (Springer, 2000).

[89] E. P. Ippen, "Self-phase modulation of picosecond pulses in optical fibers," Appl. Phys. Lett. **24**, 190 (1974).

[90] R. Stolen and C. Lin, "Self-phase-modulation in silica optical fibers," Phys. Rev. A **17**, 1448–1453 (1978).

[91] A. Chraplyvy and J. Stone, "Measurement of crossphase modulation in coherent wavelength-division multiplexing using injection lasers," Electron. Lett. **20**, 996–997 (1984).

[92] R. R. Alfano, Q. X. Li, T. Jimbo, J. T. Manassah, and P. P. Ho, "Induced spectral broadening of a weak picosecond pulse in glass produced by an intense picosecond pulse," Opt. Lett. **11**, 626–8 (1986).

[93] M. Islam, L. Mollenauer, and R. Stolen, "Cross-phase modulation in optical fibers," Opt. Lett. **12**, 625–627 (1987).

[94] R. Carman, R. Chiao, and P. Kelley, "Observation of degenerate stimulated four-photon interaction and four-wave parametric amplification," Phys. Rev. Lett. **17**, 1281–1284 (1966).

[95] R. H. Stolen, "Phase-matched three-wave mixing in silica fiber optical waveguides," Appl. Phys. Lett. **24**, 308 (1974).

[96] R. Stolen, "Phase-matched-stimulated four-photon mixing in silica-fiber waveguides," IEEE J. Quantum Electron. **QE-11**, 100–103 (1975).

[97] T. Benjamin and J. Feir, "The disintegration of wave trains on deep water," J. Fluid Mech **27** (1967).

[98] K. Hammani, C. Finot, B. Kibler, and G. Millot, "Soliton Generation and Rogue-Wave-Like Behavior Through Fourth-Order Scalar Modulation Instability," IEEE Photon. J. **1**, 205–212 (2009).

[99] A. Hasegawa and W. Brinkman, "Tunable coherent IR and FIR sources utilizing modulational instability," IEEE J. Quantum Electron. **QE-16**, 694–697 (1980).

[100] C. Raman, "A new radiation," Indian J. Phys. **2**, 387–398 (1928).

[101] D. Hollenbeck and C. D. Cantrell, "Multiple-vibrational-mode model for fiber-optic Raman gain spectrum and response function," J. Opt. Soc. Am. B **19**, 2886 (2002).

[102] J. S. Russell, "Report on waves," in "14th meeting of the British Association for the Advancement of Science," (1844), pp. 311–390.

[103] A. Hasegawa, "Transmission of stationary nonlinear optical pulses in dispersive dielectric fibers. II. Normal dispersion," Appl. Phys. Lett. **23**, 171 (1973).

[104] L. Mollenauer, R. Stolen, and J. Gordon, "Experimental observation of picosecond pulse narrowing and solitons in optical fibers," Phys. Rev. Lett. **45** (1980).

[105] A. Hasegawa and Y. Kodama, "Amplification and reshaping of optical solitons in a glass fiber-I," Opt. Lett. **7**, 285–7 (1982).

[106] A. Hasegawa, "Amplification and reshaping of optical solitons in a glass fiber-IV: Use of the stimulated Raman process," Opt. Lett. **8**, 650–652 (1983).

[107] K. Blow, N. Doran, and D. Wood, "Generation and stabilization of short soliton pulses in the amplified nonlinear Schrödinger equation," J. Opt. Soc. Am. B **5**, 381–391 (1988).

[108] H. H. Kuehl and L. Angeles, "Solitons on an axially nonuniform optical fiber," J. Opt. Soc. Am. B **5**, 709–713 (1988).

[109] Y. Kodama and A. Hasegawa, "Amplification and reshaping of optical solitons in glass fiber-II," Opt. Lett. **7**, 339–341 (1982).

[110] Y. Kodama and A. Hasegawa, "Amplification and reshaping of optical solitons in glass fiber-III. Amplifiers with random gain," Optics Letters **8**, 342–344 (1983).

[111] E. Golovchenko and E. Dianov, "Decay of optical solitons," JETP Lett **42**, 74–77 (1985).

[112] E. M. Dianov, A. Y. Karasik, P. V. Mamyshev, A. M. Prokhorov, V. N. Serkin, M. F. Stel'makh, and A. A. Fomichev, "Stimulated-Raman conversion of multisoliton pulses in quartz optical fibers," JETP Lett **41**, 242–244 (1985).

[113] F. Mitschke and L. Mollenauer, "Discovery of the soliton self-frequency shift," Opt. Lett. **11**, 659–661 (1986).

[114] J. P. Gordon, "Theory of the soliton self-frequency shift," Opt. Lett. **11**, 662–4 (1986).

[115] P. K. Wai, C. R. Menyuk, Y. C. Lee, and H. H. Chen, "Nonlinear pulse propagation in the neighborhood of the zero-dispersion wavelength of monomode optical fibers," Opt. Lett. **11**, 464–6 (1986).

[116] N. Akhmediev and M. Karlsson, "Cherenkov radiation emitted by solitons in optical fibers," Phys. Rev. A **51** (1995).

[117] I. Cristiani, R. Tediosi, L. Tartara, and V. Degiorgio, "Dispersive wave generation by solitons in microstructured optical fibers," Opt. Express **12**, 124–35 (2004).

[118] M. Erkintalo, Y. Q. Xu, S. G. Murdoch, J. M. Dudley, and G. Genty, "Cascaded Phase Matching and Nonlinear Symmetry Breaking in Fiber Frequency Combs," Phys. Rev. Lett. **109**, 223904 (2012).

[119] K. E. Webb, Y. Q. Xu, M. Erkintalo, and S. G. Murdoch, "Generalized dispersive wave emission in nonlinear fiber optics," Opt. Lett. **38**, 151 (2013).

[120] D. Faccio, E. Rubino, S. C. Kehr, F. Belgiorno, D. Townsend, S. Rohr, C. E. Kuklewicz, U. Leonhardt, and F. König, "Negative frequency resonant radiation," Phys. Rev. Lett. **108**, 253901 (2012).

[121] F. Biancalana, "Negative Frequencies Get Real," Physics Online Journal **5** (2012).

[122] N. Nishizawa and T. Goto, "Pulse trapping by ultrashort soliton pulses in optical fibers across zero-dispersion wavelength," Opt. Lett. **27**, 152–4 (2002).

[123] N. Nishizawa and T. Goto, "Characteristics of pulse trapping by use of ultrashort soliton pulses in optical fibers across the zero-dispersion wavelength," Opt. Express **10**, 1151–1159 (2002).

[124] G. Genty, M. Lehtonen, and H. Ludvigsen, "Effect of cross-phase modulation on supercontinuum generated in microstructured fibers with sub-30 fs pulses," Opt. Express **12**, 4614–24 (2004).

[125] A. V. Gorbach, D. V. Skryabin, J. M. Stone, and J. C. Knight, "Four-wave mixing of solitons with radiation and quasi-nondispersive wave packets at the short-wavelength edge of a supercontinuum," Opt. Express **14**, 9854–63 (2006).

[126] S. Hill, C. E. Kuklewicz, U. Leonhardt, and F. König, "Evolution of light trapped by a soliton in a microstructured fiber," Opt. Express **17**, 13588–600 (2009).

[127] J. C. Travers and J. R. Taylor, "Soliton trapping of dispersive waves in tapered optical fibers," Opt. Lett. **34**, 115–7 (2009).

[128] M. Islam, G. Sucha, and I. Bar-Joseph, "Femtosecond distributed soliton spectrum in fibers," J. Opt. Soc. Am. B **6** (1989).

[129] N. Savage, "Supercontinuum sources," Nat. Photon. **3**, 114–115 (2009).

[130] M. H. Frosz, O. Bang, and A. Bjarklev, "Soliton collision and Raman gain regimes in continuous-wave pumped supercontinuum generation," Opt. Express **14**, 9391–407 (2006).

[131] F. Luan, D. V. Skryabin, A. V. Yulin, and J. C. Knight, "Energy exchange between colliding solitons in photonic crystal fibers," Opt. Express **14**, 1479–1481 (2006).

[132] P. Falk, M. Frosz, O. Bang, and L. Thrane, "Broadband light generation at ˜1300 nm through spectrally recoiled solitons and dispersive waves," Opt. Lett. **33**, 621–623 (2008).

[133] A. Kudlinski and A. Mussot, "Visible cw-pumped supercontinuum," Opt. Lett. **33**, 2407–9 (2008).

[134] J. C. Travers, S. V. Popov, and J. R. Taylor, "Trapping of dispersive waves by solitons in long lengths of tapered PCF," in "Conference on Lasers and Electro-Optics," (Ieee, 2008), p. paper CThGG2.

[135] A. Mussot and A. Kudlinski, "19.5W CW-pumped supercontinuum source from 0.65 to 1.38 um," Electron. Lett. **45**, 1–2 (2009).

[136] P. Moselund, "Long-pulse supercontinuum light sources," Phd thesis, Technical University of Denmark (2009).

[137] A. Kudlinski, B. Barviau, A. Leray, and C. Spriet, "Control of pulse-to-pulse fluctuations in visible supercontinuum," Opt. Express **18**, 2670–2675 (2010).

[138] T. A. Birks, W. J. Wadsworth, and P. S. Russell, "Supercontinuum generation in tapered fibers," Opt. Lett. **25**, 1415–7 (2000).

[139] S. Leon-Saval, T. Birks, W. Wadsworth, P. St J Russell, and M. Mason, "Supercontinuum generation in submicron fibre waveguides," Opt. Express **12**, 2864–9 (2004).

[140] F. Lu, Y. Deng, and W. H. Knox, "Generation of broadband femtosecond visible pulses in dispersion-micromanaged holey fibers," Opt. Lett. **30**, 1566–8 (2005).

[141] P. Falk, M. Frosz, and O. Bang, "Supercontinuum generation in a photonic crystal fiber with two zero-dispersion wavelengths tapered to normal dispersion at all wavelengths," Opt. Express **13**, 7535–40 (2005).

[142] S. Pricking and H. Giessen, "Tailoring the soliton and supercontinuum dynamics by engineering the profile of tapered fibers," Opt. Express **18**, 5382–5387 (2010).

[143] J. Cascante-Vindas, A. Díez, J. Cruz, and M. Andrés, "White light supercontinuum generation in a Y-shaped microstructured tapered fiber pumped at 1064 nm," Opt. Express **18**, 14535–14540 (2010).

[144] W. J. Wadsworth, A. Ortigosa-Blanch, J. C. Knight, T. a. Birks, T.-P. M. Man, and P. S. J. Russell, "Supercontinuum generation in photonic crystal fibers and optical fiber tapers: a novel light source," J. Opt. Soc. Am. B **19**, 2148 (2002).

[145] M. Foster and A. Gaeta, "Ultra-low threshold supercontinuum generation in sub-wavelength waveguides," Opt. Express **12**, 3137–43 (2004).

[146] J. Teipel, D. Türke, H. Giessen, A. Zintl, and B. Braun, "Compact multi-Watt picosecond coherent white light sources using multiple-taper fibers," Opt. Express **13**, 1734–42 (2005).

[147] J. C. Travers, S. V. Popov, and J. R. Taylor, "Extended blue supercontinuum generation in cascaded holey fibers," Opt. Lett. **30**, 3132–4 (2005).

[148] C. Xiong, A. Witkowska, S. G. Leon-Saval, T. A. Birks, and W. J. Wadsworth, "Enhanced visible continuum generation from a microchip 1064nm laser," Opt. Express **14**, 6188–93 (2006).

[149] J. Cascante-Vindas, A. Diez, J. Cruz, M. Andrés, E. Silvestre, J. Miret, and A. Ortigosa-Blanch, "Tapering photonic crystal fibres for supercontinuum generation with nanosecond pulses at 532nm," Opt. Commun. **281**, 433–438 (2008).

[150] S. P. Stark, A. Podlipensky, N. Y. Joly, and P. S. J. Russell, "Ultraviolet-enhanced supercontinuum generation in tapered photonic crystal fiber," J. Opt. Soc. Am. B **27**, 592 (2010).

[151] Y. Peiguang, W. Huifeng, R. Shuangchen, Z. Junqing, Z. Jian, S. Jie, and L. Jie, "Fabrication of a 145-m long microstructured optical fiber taper and its supercontinuum generation," Opt. Engineering **50**, 105003 (2011).

[152] H. Chen, Z. Chen, X. Zhou, and J. Hou, "Cascaded PCF tapers for flat broadband supercontinuum generation," Chin. Opt. Lett. **10**, 10–12 (2012).

[153] K. Tajima, "Compensation of soliton broadening in nonlinear optical fibers with loss," Opt. Lett. **12**, 54–56 (1987).

[154] E. Bordon and W. Anderson, "Dispersion-adapted monomode fiber for propagation of nonlinear pulses," J. Lightwave Technol. **7**, 353–357 (1989).

[155] S. V. Chernikov and P. V. Mamyshev, "Femtosecond soliton propagation in fibers with slowly decreasing dispersion," J. Opt. Soc. Am. B **8**, 1633 (1991).

[156] V. Bogatyrev and M. Bubnov, "A single-mode fiber with chromatic dispersion varying along the length," J. Lightwave Technol. **9**, 561–566 (1991).

[157] S. V. Chernikov, E. M. Dianov, D. J. Richardson, and D. N. Payne, "Soliton pulse compression in dispersion-decreasing fiber," Opt. Lett. **18**, 476–8 (1993).

[158] M. Nakazawa, K. Tamura, H. Kubota, and E. Yoshida, "Coherence degradation in the process of supercontinuum generation in an optical fiber," Opt. Fiber Technol. pp. 215–223 (1998).

[159] M. Tse and P. Horak, "Designing tapered holey fibers for soliton compression," IEEE J. Quantum Electron. **44**, 192–198 (2008).

[160] J. C. Travers, J. M. Stone, A. B. Rulkov, B. A. Cumberland, A. K. George, S. V. Popov, J. C. Knight, and J. R. Taylor, "Optical pulse compression in dispersion decreasing photonic crystal fiber," Opt. Express **15**, 13203–11 (2007).

[161] F. Gérôme, K. Cook, a. K. George, W. J. Wadsworth, and J. C. Knight, "Delivery of sub-100fs pulses through 8m of hollow-core fiber using soliton compression," Opt. Express **15**, 7126–31 (2007).

[162] A. Peacock, "Mid-IR soliton compression in silicon optical fibers and fiber tapers," Opt. Lett. **37**, 818–820 (2012).

[163] A. C. Judge, O. Bang, B. J. Eggleton, B. T. Kuhlmey, E. C. Mägi, R. Pant, and C. M. de Sterke, "Optimization of the soliton self-frequency shift in a tapered photonic crystal fiber," J. Opt. Soc. Am. B **26**, 2064 (2009).

[164] C. Milián, A. Ferrando, and D. Skryabin, "Polychromatic Cherenkov radiation and supercontinuum in tapered optical fibers," J. Opt. Soc. Am. B **29**, 589–593 (2012).

[165] A. Al-kadry and M. Rochette, "Mid-infrared sources based on the soliton self-frequency shift," J. Opt. Soc. Am. B **29**, 1347–1355 (2012).

[166] A. Al-kadry and M. Rochette, "Maximized Soliton Self-frequency Shift in Non-uniform Microwires by the Control of Third-order Dispersion Perturbation," J. Lightwave Technol. **31**, 1462–1467 (2013).

[167] S. P. Stark, A. Podlipensky, and P. S. J. Russell, "Soliton Blueshift in Tapered Photonic Crystal Fibers," Phys. Rev. Lett. **083903**, 1–4 (2011).

[168] P. Dumais, F. Gonthier, S. Lacroix, J. Bures, A. Villeneuve, P. G. J. Wigley, and G. I. Stegeman, "Enhanced self-phase modulation in tapered fibers," Opt. Lett. **18**, 1996–1998 (1993).

[169] X. Liu, C. Xu, W. H. Knox, J. K. Chandalia, B. J. Eggleton, S. G. Kosinski, and R. S. Windeler, "Soliton self-frequency shift in a short tapered air-silica microstructure fiber," Opt. Lett. **26**, 358–60 (2001).

[170] T. Man, T. Birks, W. Wadsworth, and P. S. J. Russell, "Fabrication of indefinitely long tapered fibres for supercontinuum generation," OSA Tech. Dig., Nonlinear Guided Waves and Their Applications pp. paper WB4–1 (2001).

[171] E. C. Mägi, L. B. Fu, H. C. Nguyen, M. R. Lamont, D. I. Yeom, and B. J. Eggleton, "Enhanced Kerr nonlinearity in sub-wavelength diameter As(2)Se(3) chalcogenide fiber tapers," Opt. Express **15**, 10324–9 (2007).

[172] D. Hudson, S. Dekker, and E. Mägi, "Octave spanning supercontinuum in an As2S3 taper using ultralow pump pulse energy," Opt. Lett. **36**, 1122–1124 (2011).

[173] M. Liao, X. Yan, W. Gao, Z. Duan, and G. Qin, "Five-order SRSs and supercontinuum generation from a tapered tellurite microstructured fiber with longitudinally varying dispersion," Opt. Express **19**, 15389–15396 (2011).

[174] A. Marandi, C. Rudy, N. C. Leindecker, V. G. Plotnichenko, E. M. Dianov, K. L. Vodopyanov, and R. L. Byer, "Mid-Infrared Supercontinuum Generation from 2.4 m to 4.6 m in Tapered Chalcogenide Fiber," in "Conference on Lasers and Electro-Optics," (2012), pp. 7–8.

[175] J. Chandalia, B. Eggleton, R. Windeler, S. Kosinski, X. Liu, and C. Xu, "Adiabatic coupling in tapered air-silica microstructured optical fiber," IEEE Photon. Technol. Lett. **13**, 52–54 (2001).

[176] R. Kenny, T. Birks, and K. Oakley, "Control of optical fibre taper shape," Electron. Lett. **27** (1991).

[177] T. A. Birks, G. Kakarantzasa, P. S. Russell, and D. F. Murphy, "Photonic crystal fibre devices," Proc. of SPIE **4943**, 142–151 (2003).

[178] H. C. Nguyen, B. T. Kuhlmey, E. C. Mägi, M. J. Steel, P. Domachuk, C. L. Smith, and B. J. Eggleton, "Tapered photonic crystal fibres: properties, characterisation and applications," Appl. Phys. B **81**, 377–387 (2005).

[179] N. Vukovic, N. G. R. Broderick, M. Petrovich, and G. Brambilla, "Novel Method for the Fabrication of Long Optical Fiber Tapers," IEEE Photon. Technol. Lett. **20**, 1264–1266 (2008).

[180] S. Pricking and H. Giessen, "Tapering fibers with complex shape," Opt. Express **18**, 3426–37 (2010).

[181] A. Felipe, G. Espíndola, H. J. Kalinowski, J. A. S. Lima, and A. S. Paterno, "Stepwise fabrication of arbitrary fiber optic tapers," Opt. Express **20**, 19893–904 (2012).

[182] M. Liao, W. Gao, Z. Duan, and X. Yan, "Directly draw highly nonlinear tellurite microstructured fiber with diameter varying sharply in a short fiber length," Opt. Express **20**, 1141–1150 (2012).

[183] C. Cordeiro and W. Wadsworth, "Engineering the dispersion of tapered fibers for supercontinuum generation with a 1064 nm pump laser," Opt. Lett. **30**, 1980–1982 (2005).

[184] M. H. Frosz, P. M. Moselund, P. D. Rasmussen, C. L. Thomsen, and O. Bang, "Increasing the blue-shift of a supercontinuum by modifying the fiber glass composition," Opt. Express **16**, 21076–86 (2008).

[185] B. Barviau, O. Vanvincq, and A. Mussot, "Enhanced soliton self-frequency shift and CW supercontinuum generation in GeO2-doped core photonic crystal fibers," J. Opt. Soc. Am. B **28**, 1152–1160 (2011).

[186] X. Zhang, X. Zhu, R. Xing, X. Yang, F. Jiang, H. Li, J. Peng, N. Dai, and J. Li, "Microstructure core photonic crystal fiber for blue extension of supercontinuum generation," Opt. Commun. **298-299**, 191–195 (2013).

[187] N. Vukovic and N. Broderick, "Method for improving the spectral flatness of the supercontinuum at 1.55 um in tapered microstructured optical fibers," Phys. Rev. A **82**, 043840 (2010).

[188] Z. Chen, A. J. Taylor, and A. Efimov, "Soliton dynamics in non-uniform fiber tapers: analytical description through an improved moment method," J. Opt. Soc. Am. B **27**, 1022 (2010).

[189] A. C. Judge, O. Bang, and C. Martijn de Sterke, "Theory of dispersive wave frequency shift via trapping by a soliton in an axially nonuniform optical fiber," J. Opt. Soc. Am. B **27**, 2195 (2010).

[190] T. Schreiber, T. Andersen, D. Schimpf, J. Limpert, and A. Tünnermann, "Supercontinuum generation by femtosecond single and dual wavelength pumping in photonic crystal fibers with two zero dispersion wavelengths," Opt. Express **13**, 9556–69 (2005).

[191] M. Koshiba and K. Saitoh, "Applicability of classical optical fiber theories to holey fibers," Opt. Lett. **29**, 1739–1741 (2004).

[192] NKT Photonics A/S, "Application Note: Spectral Density Measurements," www.nktphotonics.com (2011).

[193] W. Wadsworth, A. Witkowska, S. Leon-Saval, and T. Birks, "Hole inflation and tapering of stock photonic crystal fibres," Opt. Express **13**, 6541–9 (2005).

[194] L. Skuja, "Optically active oxygen-deficiency-related centers in amorphous silicon dioxide," J. Non-Cryst. Sol. **239**, 16–48 (1998).

[195] L. Skuja, K. Kajihara, M. Hirano, and H. Hosono, "Visible to vacuum-UV range optical absorption of oxygen dangling bonds in amorphous SiO_{2}," Phys. Rev. B **84**, 205206 (2011).

[196] J. C. Travers, W. Chang, J. Nold, N. Y. Joly, and P. St. J. Russell, "Ultrafast nonlinear optics in gas-filled hollow-core photonic crystal fibers [Invited]," J. Opt. Soc. Am. B **28**, A11 (2011).

[197] P. Hölzer, W. Chang, J. Travers, and A. Nazarkin, "Femtosecond nonlinear fiber optics in the ionization regime," Phys. Rev. Lett. **203901**, 1–5 (2011).
[198] Z. Sun and A. C. Ferrari, "Fibre sources in the deep ultraviolet," Nat. Photon. **5**, 446—-447 (2011).
[199] A. Gaeta, "Nonlinear propagation and continuum generation in microstructured optical fibers," Opt. Lett. **27**, 924–926 (2002).
[200] X. Gu, L. Xu, M. Kimmel, E. Zeek, P. O'Shea, A. P. Shreenath, R. Trebino, and R. S. Windeler, "Frequency-resolved optical gating and single-shot spectral measurements reveal fine structure in microstructure-fiber continuum," Opt. Lett. **27**, 1174–6 (2002).
[201] K. L. Corwin, N. R. Newbury, J. M. Dudley, S. Coen, S. a. Diddams, K. Weber, and R. S. Windeler, "Fundamental Noise Limitations to Supercontinuum Generation in Microstructure Fiber," Phys. Rev. Lett. **90**, 1–4 (2003).
[202] K. Corwin, N. Newbury, J. Dudley, S. Coen, S. Diddams, B. Washburn, K. Weber, and R. Windeler, "Fundamental amplitude noise limitations to supercontinuum spectra generated in a microstructured fiber," Appl. Phys. B **77**, 269–277 (2003).
[203] N. Newbury and B. Washburn, "Noise amplification during supercontinuum generation in microstructure fiber," Opt. Lett. **28**, 944–946 (2003).
[204] J. Dudley and S. Coen, "Numerical simulations and coherence properties of supercontinuum generation in photonic crystal and tapered optical fibers," IEEE J. Sel. Top. Quant. Electron. **8**, 651–659 (2002).
[205] G. Genty, C. M. D. Sterke, O. Bang, F. Dias, N. Akhmediev, and J. M. Dudley, "Collisions and turbulence in optical rogue wave formation," Phys. Lett. A **374**, 989–996 (2010).
[206] J. M. Dudley, G. Genty, and B. J. Eggleton, "Harnessing and control of optical rogue waves in supercontinuum generation," Opt. Express **16**, 3644–51 (2008).
[207] A. Mussot, A. Kudlinski, M. Kolobov, E. Louvergneaux, M. Douay, and M. Taki, "Observation of extreme temporal events in CW-pumped supercontinuum," Opt. Express **17**, 17010 (2009).
[208] N. Akhmediev, A. Ankiewicz, and M. Taki, "Waves that appear from nowhere and disappear without a trace," Phys. Lett. A **373**, 675–678 (2009).
[209] M. Erkintalo, G. Genty, and J. Dudley, "Giant dispersive wave generation through soliton collision," Opt. Lett. **35**, 658–660 (2010).
[210] M. Erkintalo, G. Genty, and J. Dudley, "On the statistical interpretation of optical rogue waves," Eur. Phys. J. **144**, 135–144 (2010).
[211] D. Buccoliero, H. Steffensen, H. Ebendorff-heidepriem, T. M. Monro, and O. Bang, "Midinfrared optical rogue waves in soft glass photonic crystal fiber," Opt. Express **19**, 17973–17978 (2011).
[212] B. Wetzel, K. J. Blow, S. K. Turitsyn, G. Millot, L. Larger, and J. M. Dudley, "Random walks and random numbers from supercontinuum generation," Opt. Express **20**, 11143–52 (2012).
[213] M. Bellini and T. Hänsch, "Phase-locked white-light continuum pulses: toward a universal optical frequency-comb synthesizer," Opt. Lett. **25**, 1049–1051 (2000).

[214] J. Dudley and S. Coen, "Coherence properties of supercontinuum spectra generated in photonic crystal and tapered optical fibers," Opt. Lett. **27**, 1180–1182 (2002).

[215] C. Lafargue, J. Bolger, G. Genty, F. Dias, J. M. Dudley, and B. J. Eggleton, "Direct detection of optical rogue wave energy statistics in supercontinuum generation," IEEE Electron. Lett. **45** (2009).

[216] B. Wetzel, A. Stefani, L. Larger, P. A. Lacourt, J. M. Merolla, T. Sylvestre, A. Kudlinski, A. Mussot, G. Genty, F. Dias, and J. M. Dudley, "Real-time full bandwidth measurement of spectral noise in supercontinuum generation," Sci. Rep. **2**, 882 (2012).

[217] D. Solli, C. Ropers, and B. Jalali, "Active control of rogue waves for stimulated supercontinuum generation," Phys. Rev. Lett. **233902**, 18–21 (2008).

[218] B. Kibler, J. Fatome, C. Finot, G. Millot, and F. Dias, "The Peregrine soliton in nonlinear fibre optics," Nature Phys. **6**, 790–795 (2010).

[219] M. Erkintalo, K. Hammani, B. Kibler, C. Finot, N. Akhmediev, J. M. Dudley, and G. Genty, "Higher-order modulation instability in nonlinear fiber optics," Phys. Rev. Lett. **253901**, 14–18 (2011).

[220] P. Moselund, M. Frosz, C. Thomsen, and O. Bang, "Back-seeding of higher order gain processes in picosecond supercontinuum generation," Opt. Express **16**, 1644–1646 (2008).

[221] G. Genty, J. M. Dudley, and B. J. Eggleton, "Modulation control and spectral shaping of optical fiber supercontinuum generation in the picosecond regime," Appl. Phys. B **94**, 187–194 (2009).

[222] G. Genty and J. Dudley, "Route to coherent supercontinuum generation in the long pulse regime," IEEE J. Quantum Electron. **45**, 1331–1335 (2009).

[223] D. Solli, B. Jalali, and C. Ropers, "Seeded supercontinuum generation with optical parametric down-conversion," Phys. Rev. Lett. **233902**, 1–4 (2010).

[224] K. Cheung, C. Zhang, and Y. Zhou, "Manipulating supercontinuum generation by minute continuous wave," Opt. Lett. **36**, 160–162 (2011).

[225] Q. Li, F. Li, K. Wong, and A. Lau, "Investigating the influence of a weak continuous-wave-trigger on picosecond supercontinuum generation," Opt. Express **19**, 377–381 (2011).

[226] M. Kues, N. Brauckmann, and T. Walbaum, "Nonlinear dynamics of femtosecond supercontinuum generation with feedback," Opt. Express **17**, 635–639 (2009).

[227] N. Brauckmann, M. Kues, T. Walbaum, and C. Fallnich, "Experimental investigations on nonlinear dynamics in supercontinuum generation with feedback," Opt. Express **18**, 233–237 (2010).

[228] N. Brauckmann, M. Kues, P. Groß, and C. Fallnich, "Adjustment of supercontinua via the optical feedback phasenumerical investigations," Opt. Express **18**, 20667–20672 (2010).

[229] N. Brauckmann, M. Kues, P. Groß, and C. Fallnich, "Adjustment of supercontinua via the optical feedback phaseexperimental verifications," Opt. Express **18**, 24611–24618 (2010).

[230] M. Kues, N. Brauckmann, P. Groß, and C. Fallnich, "Basic prerequisites for limit-cycle oscillations within a synchronously pumped passive optical nonlinear fiber-ring resonator," Phys. Rev. A **033833**, 1–10 (2011).

[231] N. Brauckmann, M. Kues, P. Groß, and C. Fallnich, "Noise reduction of supercontinua via optical feedback," Opt. Express **19**, 7914–7923 (2011).

[232] P. Groß, N. Haarlammert, M. Kues, T. Walbaum, and C. Fallnich, "Optical Fiber Technology Effects of optical feedback on femtosecond supercontinuum generation," Opt. Fiber Technol. **18**, 290–303 (2012).

[233] M. Schmidberger, W. Chang, P. S. J. Russell, and N. Y. Joly, "Influence of timing jitter on nonlinear dynamics of a photonic crystal fiber ring cavity," Opt. Lett. **37**, 3576–8 (2012).

[234] D. Solli, G. Herink, B. Jalali, and C. Ropers, "Fluctuations and correlations in modulation instability," Nat. Photon. **6**, 463–468 (2012).

[235] A. Mussot and A. Kudlinski, "Modulation instability: Loaded dice," Nat. Photon. **6** (2012).

[236] D. R. Solli, C. Ropers, and B. Jalali, "Measuring single-shot modulation instability and supercontinuum spectra at megahertz rates," Nonlinearity **26**, R85–R92 (2013).

[237] A. A. Rieznik, A. M. Heidt, G. König, V. A. Bettachini, and D. F. Grosz, "Optimum Integration Procedures for Supercontinuum Simulation," IEEE Photon. J. **4**, 552–560 (2012).

[238] O. Vanvincq, J. Travers, and A. Kudlinski, "Conservation of the photon number in the generalized nonlinear Schrödinger equation in axially varying optical fibers," Phys. Rev. A **84**, 1–7 (2011).

[239] J. Lægsgaard, "Modeling of nonlinear propagation in fiber tapers," J. Opt. Soc. Am. B **29**, 3183 (2012).

[240] A. Heidt, "Efficient adaptive step size method for the simulation of supercontinuum generation in optical fibers," J. Lightwave Technol. **27**, 3984–3991 (2009).

[241] G. Bosco, A. Carena, V. Curri, R. Gaudino, P. Poggiolini, and S. Benedetto, "Suppression of spurious tones induced by the split-step method in fiber systems simulation," IEEE Photon. Technol. Lett. **12**, 489–491 (2000).

[242] O. Sinkin, R. Holzlohner, J. Zweck, and C. Menyuk, "Optimization of the split-step fourier method in modeling optical-fiber communications systems," J. Lightwave Technol. **21**, 61–68 (2003).

[243] C. Shannon, "Communication in the presence of noise," Proc. of the IRE **37**, 10–21 (1949).

[244] M. H. Frosz, "Supercontinuum generation in photonic crystal fibres : Modelling and dispersion engineering for spectral shaping," Ph.D. thesis, Technical University of Denmark (2006).

[245] R. Smith, "Optical power handling capacity of low loss optical fibers as determined by stimulated Raman and Brillouin scattering," Appl. Opt. **11**, 2489–2494 (1972).

[246] M. H. Frosz, "Validation of input-noise model for simulations of supercontinuum generation and rogue waves," Opt. Express **18**, 14778–87 (2010).

[247] S. B. Cavalcanti and G. P. Agrawal, "Noise amplification in dispersive nonlinear media," Phys. Rev. A **51**, 4086 (1995).

[248] A. Mussot, E. Lantz, H. Maillotte, T. Sylvestre, C. Finot, and S. Pitois, "Spectral broadening of a partially coherent CW laser beam in single-mode optical fibers," Opt. Express **12**, 2838–43 (2004).

[249] J. Gowar, *Optical communication systems* (Prentice-Hall, Inc., 1993), 2nd ed.